

Copyright
by
Rosa Elia Cárdenas
2011

The Dissertation Committee for Rosa Elia Cárdenas
certifies that this is the approved version of the following dissertation:

**Analysis of Crystalline Ammonium
Hexafluorophosphate using Nuclear Magnetic
Resonance Force Microscopy (NMRFM) and Design
and Construction of a Dynamical Room-Temperature
NMRFM Microscope**

Committee:

John T. Markert, Supervisor

Alejandro de Lozanne

Allan MacDonald

Zhen Yao

David W. Hoffman

**Analysis of Crystalline Ammonium
Hexafluorophosphate using Nuclear Magnetic
Resonance Force Microscopy (NMRFM) and Design
and Construction of a Dynamical Room-Temperature
NMRFM Microscope**

by

Rosa Elia Cárdenas, B.S. Phy; M.A.

DISSERTATION

Presented to the Faculty of the Graduate School of
The University of Texas at Austin
in Partial Fulfillment
of the Requirements
for the Degree of

DOCTOR OF PHILOSOPHY

THE UNIVERSITY OF TEXAS AT AUSTIN

August 2011

To my mother.

Acknowledgments

I would like to thank everyone who helped and encouraged me throughout my time as a graduate student. I would particularly like to thank Dr. John T. Markert for being a great advisor. I would also like to thank all of the members of the Markert Lab. They were an invaluable source of knowledge and support. I would particularly like to thank Jay-Hyuk Choi, Utkur Mirsaidov, Yong Lee, Wei Lu, Isaac Manzanera, Keesong Park and Mark Monti.

I would also like to thank my family for being very supportive and understanding. My mother, for always encouraging me (*hechale ganas*), for being Mami when I need her to be, and for praying for me every time I ask her to. My father, who instilled a great work ethic in me. I would also like to express my deepest appreciation to my big sister, Maria del Pilar, for asserting her great courage as a young woman and setting a virtuous example for all of her younger siblings. Because of you, Pily, I am here today. Thank you. She was brave enough to leave home and go to college before anyone else had from our entire family. My sister Ruth, who showed me that there was an entire world away from Eagle Pass, TX that needed to be explored - “Isabella Rossellini, Lancome”. We have both done lots of exploring since then. My brother Beny, who introduced me to the wonderful world of university life while I was still in high school. That was definitely motivation for me to go

to college! While I visited him at The University of Wisconsin-Madison, I sat in on an introductory physics lecture and realized that I could hold my own in a physics class. And even before this, I thank him for letting me tag along with him and his friends, although it was reluctantly on his part. Through this experience, I learned how to interact with boys, which made the male-dominated world of physics less intimidating.

I would also like to thank the Bill and Melinda Gates Foundation for their financial support by the Gates Millennium Scholarship. I would also like to thank the University of Texas at Austin Department of Physics for their financial support. Finally, I would like to thank the University of Texas College of Natural Sciences Freshman Research Initiative (FRI) program for their financial support.

**Analysis of Crystalline Ammonium
Hexafluorophosphate using Nuclear Magnetic
Resonance Force Microscopy (NMRFM) and Design
and Construction of a Dynamical Room-Temperature
NMRFM Microscope**

Publication No. _____

Rosa Elia Cárdenas, Ph.D.
The University of Texas at Austin, 2011

Supervisor: John T. Markert

In this dissertation I explain the theoretical and experimental details of nuclear magnetic resonance force microscopy (NMRFM). I report the data that I have collected on ammonium hexafluorophosphate at room temperature using NMRFM. This experiment measured cantilever deflection as a function of applied magnetic field. I also report on the progress of a new dynamical room-temperature NMRFM microscope. I describe the new probe and its advantages over the previous generation probe and I show the current calibration measurements.

Table of Contents

Acknowledgments	v
Abstract	vii
List of Figures	xi
Chapter 1. Introduction	1
Chapter 2. Theory	4
2.1 Nuclear Magnetic Resonance (NMR)	4
2.1.1 Nuclear Magnetic Resonance Absorption	4
2.1.2 Curie's Law	6
2.2 Time Evolution of Magnetization	8
2.2.1 Magnetization Equation of Motion	8
2.2.2 The Bloch Equations	11
2.3 Relaxation Times	12
2.3.1 What are the relaxation times T_2 and T_2^* ?	12
2.3.2 What is the relaxation time T_1 ?	16
2.4 Nuclear Magnetic Resonance Experimental Set-Up	16
2.4.1 NMR Signal To Noise Ratio	17
2.5 Nuclear Magnetic Resonance Force Microscopy (NMRFM) . .	20
2.5.1 Modulation	21
2.5.2 Nuclear Magnetic Resonance Force Microscopy Basic Ex- perimental Set-Up	24
2.5.3 NMRFM Signal To Noise Ratio	25

Chapter 3. NMRFM Experimental Details	26
3.1 NMRFM Schematic Details	26
3.2 The NMRFM Pulse	26
3.2.1 The Pulse Box	26
3.2.2 RF Decay to Resonance and Modulation	27
3.2.3 Radio Frequency Signal Generator	31
3.2.4 The RF Gate	33
3.2.5 The Tank Circuit	35
3.3 Signal Detection	36
3.3.1 The Interferometer	36
3.3.2 Cleaving The Fiber	42
3.3.3 Alignment	45
3.3.4 Feedback by the Fringe-Lock Circuit	47
Chapter 4. NMRFM Experiment and Results	51
4.1 La Flaca	51
4.2 Ammonium Hexafluorophosphate, NH_4PF_6	52
4.3 NMRFM Experimental Set-Up for Ammonium Hexafluorophosphate	54
4.4 NMRFM Ammonium Hexafluorophosphate Scan Results	55
4.5 Probe Limitations	57
Chapter 5. New Room Temperature NMRFM Probe	68
5.1 La Flaca II	68
5.2 Tiny Slip-Stick Positioners	68
5.3 Positioner Electronics	70
Chapter 6. Micro Magnet Coated Cantilevers	82
6.1 Permalloy Deposition and Masking	82
6.2 Results	83

Chapter 7. Summary and Future Work	86
7.1 Summary	86
7.2 Future Work	87
7.2.1 Analysis of Micro Magnet Coated Cantilevers	87
7.2.2 NMRFM Liquid Sample	88
Appendices	90
Appendix A. NMR Periodic Table	91
Appendix B. RF Board Parts	94
Appendix C. Powering On The Big Red Electromagnet	99
C.1 Powering On Procedure	99
C.2 Powering Off Procedure	100
C.3 Post Power Surge Measures	100
Appendix D. Slip-Stick Stage Machine Drawings	101
Appendix E. Piezo Specifications	116
E.1 Plate Piezo Specifications	116
E.2 Stack Piezo Specifications	116
Appendix F. Epoxy Specifications	118
Bibliography	121
Vita	125

List of Figures

2.1	Zeeman Energy Splitting in Hydrogen	5
2.2	Zeeman Energy Splitting	6
2.3	Precessing Moment	9
2.4	Rotating Frame	10
2.5	Moment tilt angle	11
2.6	Free Induction Decay	13
2.7	T_2^* Calculation	14
2.8	T_2 Measurement: $\pi/2, \tau, \pi$	15
2.9	Magnetization during a Hahn spin echo	15
2.10	T_1 Measurement: $\pi, \tau, \pi/2$	17
2.11	NMR Experimental Set-Up	17
2.12	NMR $\pi/2$	18
2.13	NMR Schematic	19
2.14	B_{eff}	23
2.15	NMRFM magnet on cantilever experimental set-up	24
2.16	NMRFM sample on cantilever experimental set-up	25
3.1	NMRFM Schematic A	28
3.2	NMRFM Schematic B	29
3.4	Modulation Box Circuit Diagram	31
3.5	Pulse And Modulation Box Output	32
3.6	Pulse Programmer And Modulation Box	33
3.7	Agilent 4402B Spectrum Analyzer	34
3.8	HP8640B Output Through Spectrum Analyzer	35
3.11	Ceramic Variable Capacitor	35
3.9	Modulated RF Output Through Spectrum Analyzer	36
3.14	Coil	36
3.10	RF Board Circuit Diagram	37

3.12	HP 8753 Network Analyzer	38
3.13	Ceramic Variable Capacitors	39
3.15	Incident, Refracted and Reflected Rays	39
3.16	Stainless Steel Tubing	43
3.17	Mechanical $x - y - z$ Stage	48
3.18	Feedback Cartoon	49
4.1	Utkur's Probe	52
4.2	Mounted Variable Capacitors	58
4.3	Ammonium Hexafluorophosphate	59
4.4	Resonant Field	59
4.5	Field vs. Distance	60
4.6	NMRFM Mechanical Stage	61
4.7	Driven Scans	62
4.8	Driven Scans Again	62
4.9	Driven Scans In Components	63
4.10	Artifact	63
4.11	Artifacts	64
4.12	Igor Pro Procedure	64
4.13	Table of Minima and Maxima	65
4.14	Maxima Vs. Field	66
4.15	Normalized Data vs. Field	66
4.16	Igor Pro Normalization Procedure	67
5.1	Probe Schematic	73
5.2	Probe Pictures	74
5.3	DAQ Card Pinout	75
5.4	OPA 549 Specifications	76
5.5	OPA 549 Circuit Diagram	77
5.6	OPA 549 Photolithography Mask	78
5.7	Photoresist Coated Board and Mask	78
5.8	OPA 549 Final Circuit	79
5.9	Moving Fiber	80

5.10	Z - Direction Calibration	81
6.1	Cantilever Masking Schematic	82
6.2	Optical and SEM Coated Cantilever Images	83
6.3	SQUID Data	85
7.1	Magnet Capped Oscillator Resonant Frequency Shift	87
7.2	Silicon Nitride Window	88
7.3	Liquid NMRFM Experiment	89
A.1	NMR Periodic Table A	92
A.2	NMR Periodic Table B	93
B.1	3820 Data Sheet	94
B.2	3906 Data Sheet	95
B.3	LM117 Data Sheet	96
B.4	NTE957 Data Sheet	97
B.5	RF Gate Data Sheet	98

Chapter 1

Introduction

Nuclear Magnetic Resonance (NMR) is a technique used to manipulate the nuclear moments in a sample. By manipulating the nuclear moments in specific ways and monitoring their evolution, we can extract useful information from the system like the relaxation times, T_1 , T_2 , and T_2^* . In the familiar technique, Nuclear Magnetic Resonance Imaging (MRI), the result of measuring the evolution of the nuclear moments of the system is an image.

When considering a macroscopic object like a part of the human body, the resolution from an MRI image, which uses conventional NMR, can be considered “good”. Large sample, for example brain MRIs have resolution of only a little less than a millimeter. Currently, the highest resolution of an MRI image is approximately a few microns for a liquid at room temperature and $50 \mu\text{m}$ for a solid at room temperature [1]. The limiting factor in this resolution is the method for collecting data. Recall that an MRI image is created by measuring the evolution of the nuclear moments by conventional NMR. Data in conventional NMR is collected inductively by a coil.

In order to increase the resolution one must collect data by a method different from that of an inductive coil. The best alternative method for col-

lecting data has been found by using Magnetic Resonance Force Microscopy (MRFM).

Magnetic Resonance Force Microscopy (MRFM) was originally proposed in 1991 by Sidles [2] as a way to obtain high resolution three dimensional images of individual biological molecules. MRFM has since been modified and improved, but the principle remains the same. The way it works is that the force created by an oscillating magnetization can be detected by coupling it to a mechanical micro-oscillator through a field gradient. This has been demonstrated by the detection of a force as small as 10^{-21} N [3].

Nuclear magnetic resonance force microscopy (NMRFM) is the type of MRFM that uses nuclear signals to conduct three dimensional scanning. Imaging using this technique has resulted in the detection of a force of 10^{-17} N [4] with a spatial resolution of approximately 4 nm [4]. This spatial resolution is approximately 10^9 times better in volume than that currently obtained in MRI using conventional NMR inductive techniques.

Another coveted detection milestone is the direct detection of a single nuclear spin. Currently NMRFM is the only feasible technique that could accomplish this. But, in order to detect a single nuclear spin, it may be necessary to detect a force as small as 10^{-24} N [3], 1000 times smaller than the smallest force yet detected by an MRFM technique.

In this dissertation I will describe a room-temperature NMRFM experiment to analyze ammonium hexafluorophosphate and the development and

characterization of a new dynamical room-temperature NMRFM microscope.

In Chapter 2 I review the theory of NMR. In Chapter 3, I discuss NMRFM experimental details. Chapter 4 describes the experimental results of an NMRFM experiment. Chapter 5 explains the new room-temperature NMRFM probe that I have put together. Chapter 6 discusses a technique that we use to deposit magnetic material on cantilevers, and Chapter 7 summarizes the dissertation and explains work to be done in the future.

Chapter 2

Theory

2.1 Nuclear Magnetic Resonance (NMR)

2.1.1 Nuclear Magnetic Resonance Absorption

Consider a nucleus with a magnetic moment, $\vec{m} = \gamma\vec{L}$, where γ is the gyromagnetic ratio specific to the nuclear species. When this moment is placed in an external magnetic field, \vec{B} , it experiences a torque, $\vec{\tau} = d\vec{L}/dt$ [5].

$$\frac{d\vec{L}}{dt} = \vec{m} \times \vec{B} \quad (2.1)$$

The magnetic energy associated with a moment in an external magnetic field is given by [6] [7] [8]:

$$U = -\vec{m} \cdot \vec{B} = -\gamma\vec{L} \cdot \vec{B} \quad (2.2)$$

If $\vec{B} = B_0\hat{z}$, then

$$U = -m_z B_0 = -\gamma\hbar B_0 l_z, \quad (2.3)$$

Where the values of l_z are $m_l = -l, -l + 1, \dots, +l$, so $U = -\gamma\hbar B_0 m_l$. For example, if a nucleus has $l = \frac{1}{2}$, then $m_l = \pm\frac{1}{2}$, and there are two energy states,

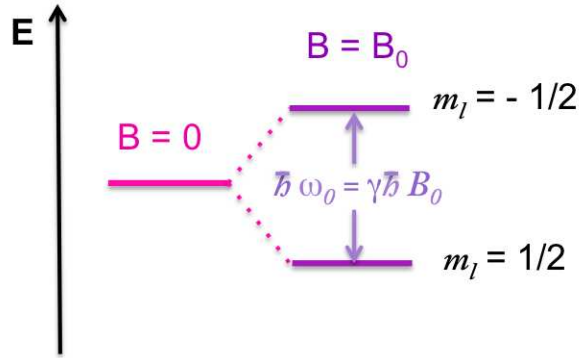


Figure 2.2: The energy when there is no external field and the splitting of the energy when an external field B_0 is applied.

given by:

$$\Delta E = \gamma B_0 \hbar \equiv \hbar \omega_0, \quad (2.5)$$

and so,

$$\omega_0 = \gamma B_0. \quad (2.6)$$

This is the condition for nuclear magnetic resonance absorption and the foundation for nuclear magnetic resonance. A periodic table that lists the gyro-magnetic ratio of each nuclear species is shown in Appendix A.

2.1.2 Curie's Law

The population of the energy levels of an ensemble of nuclei in thermal equilibrium is determined by the Boltzmann distribution,

$$f_j = \frac{N e^{-E_j/k_B T}}{\sum_j g_j e^{E_j/k_B T}} \quad (2.7)$$

where N is the number of particles, E_j is the energy of the j^{th} state, k_B is the Boltzmann constant, T is the absolute temperature and g_j is the degeneracy of the j^{th} state [9]. The population ratio between two states, i and j , is given by the Boltzmann ratio [10],

$$B_{ij} = e^{(E_i - E_j)/k_B T}. \quad (2.8)$$

When discussing nuclear magnetic resonance, one should keep in mind that the signal being detected is very small. This is because at room temperature, the population difference is quite tiny. For example, consider a proton rich sample immersed in a 10 T field at 293 K, $B_{ij} = e^{1.1 \times 10^{-5}} = 1$. So the population ratio is nearly unity; up and down states are nearly equally populated. Of course, a small number of spins implies a small signal to detect.

The signal that we measure when discussing NMR is the net magnetization of many atomic nuclei. The expression for the net magnetization of the sample can be calculated from Boltzmann statistics and the quantum theory of paramagnetism. In effect, the total magnetization is just the number of nuclei pointing along the externally applied field, B_{ij} , times the magnetization of each, $m_z = \gamma \hbar l_z$. However, one must recall that in a magnetic field a nucleus with angular momentum l has $2l + 1$ equally spaced energy levels which must be considered in the expression for the magnetization. By doing so, we now have a more general expression for the magnetization given by:

$$M = \frac{N \gamma^2 \hbar^2 l(l+1)}{3k_B T} B_0, \quad (2.9)$$

[11] [7] where

$$M \equiv \chi_0 B_0. \quad (2.10)$$

χ_0 is the magnetic susceptibility, and

$$\chi_0 = \frac{N\gamma^2\hbar^2 L(L+1)}{3k_B T} \equiv \frac{C}{T}, \quad (2.11)$$

where C is known as the Curie constant and Equation 2.11 is called Curie's Law. Curie's Law is valid in the high temperature limit when $T \gg \frac{\gamma\hbar B_0}{k_B}$.

2.2 Time Evolution of Magnetization

2.2.1 Magnetization Equation of Motion

Recall that when a moment is placed in an external magnetic field, \vec{B} , it experiences a torque, $\vec{\tau} = \frac{d\vec{L}}{dt} = \vec{m} \times \vec{B}$. To obtain the equation of motion of the magnetization, we can take the derivative of \vec{m} .

$$\frac{d\vec{m}}{dt} = \gamma \frac{d\vec{L}}{dt} = \gamma \vec{m} \times \vec{B} \quad (2.12)$$

This equation has the familiar form found in classical mechanics for a spinning top that precesses about its axis [6]. By analogy, we expect for our moment to precess about its axis.

In general one studies an ensemble of nuclei so we let \vec{M} be the vector sum of the individual spins, \vec{m} [12]. We can now get a relationship for the total magnetization:

$$\frac{d\vec{M}}{dt} = \gamma \vec{M} \times \vec{B} \quad (2.13)$$

If $\vec{B} = B_0\hat{z}$, then the precession will be about the \hat{z} axis. I will define the vector

$$\vec{B}_0 = B_0\hat{z}. \quad (2.14)$$

The precession frequency is given by Equation 2.6, where

$$\omega_{Larmor} \equiv \omega_0 = \gamma B_0. \quad (2.15)$$

To manipulate the magnetization, one can apply a sinusoidal magnetic field, \vec{B}_1 , in the plane perpendicular to \vec{B}_0 . \vec{B}_1 should oscillate at a radio frequency (rf) near the Larmor frequency and have the following form:

$$\vec{B}_1 = B_1[\cos(\omega_{rf}t)\hat{x} - \sin(\omega_{rf}t)\hat{y}]. \quad (2.16)$$

We can now include both \vec{B}_0 and \vec{B}_1 in the equation of motion. To simplify the expression, we change to a rotating coordinate system with new axes, x', y', z , that rotates at the same radio frequency as \vec{B}_1 [12].

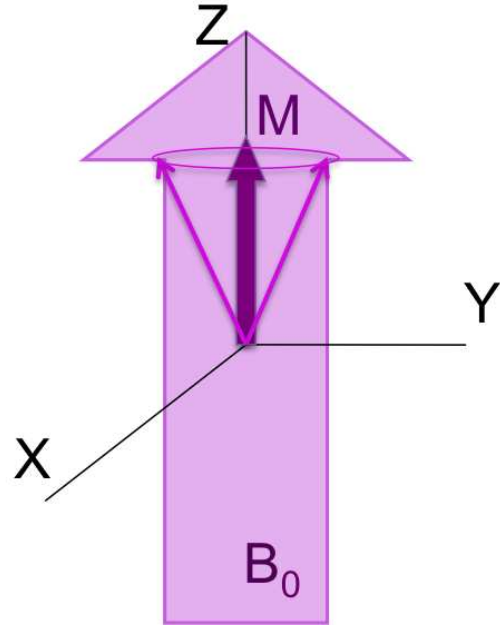


Figure 2.3: The net moment is the sum of all of the individual precessing moments points along z.

The new equation of motion

is:

$$\frac{d\vec{M}}{dt} = \gamma\vec{M} \times [\vec{B}_0 + \vec{B}_1] + \vec{\omega}_{rf} \times \vec{M}. \quad (2.17)$$

This can be rewritten such that:

$$\frac{d\vec{M}}{dt} = \gamma\vec{M} \times \underbrace{[(B_0 - \omega_{rf}/\gamma)\hat{z} + B_1\hat{x}']}_{\vec{B}_{eff}}. \quad (2.18)$$

By rearranging into this form and expressing the second half of the equation as an effective field, \vec{B}_{eff} , where

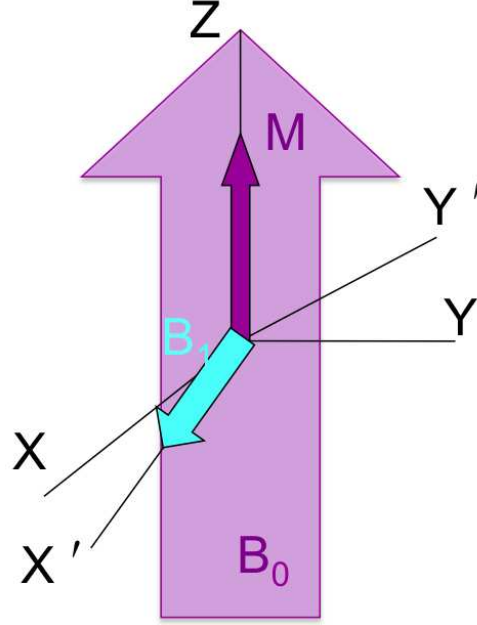
$$\vec{B}_{eff} = B_1\hat{x}' + (B_0 - \omega_{rf}/\gamma)\hat{z}, \quad \text{Figure 2.4: } B_1 \text{ points along } x'. \quad (2.19)$$

the equation of motion, Equation 2.18, becomes similar in form to the familiar Equation 2.13.

Now, if the resonant frequency is satisfied by setting $\omega_{rf} = \omega_0 = \gamma B_0$, then the effective field becomes $\vec{B}_{eff} = B_1\hat{x}'$. This makes our equation of motion take the form:

$$\frac{d\vec{M}}{dt} = \gamma\vec{M} \times B_1\hat{x}'. \quad (2.20)$$

This now implies that the magnetization precesses about the x' - axis, and that the magnetization direction changes with length and strength of the



radio frequency, $B_1\hat{x}'$, pulse. The angle, θ , that \vec{M} tilts from the \hat{z} direction can be found by integrating Equation 2.6 to get:

$$\theta = \gamma B_1 t_p. \quad (2.21)$$

Where t_p is the duration of the radio frequency pulse, $B_1\hat{x}'$, and B_1 is its magnitude.

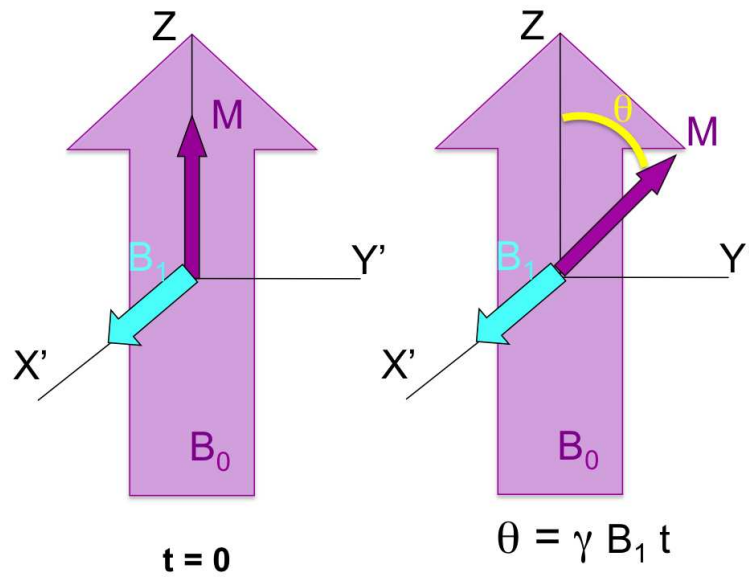


Figure 2.5: The angle by which the moment is tilted around x' depends on the length of time that B_1 is applied along the x' direction.

2.2.2 The Bloch Equations

Recall the equation of motion of the magnetization given by Equation 2.13. Where, in general,

$$\vec{B} = \vec{B}_0 + \vec{B}_1 = B_1[\cos(\omega_r t)\hat{x} - \sin(\omega_r t)\hat{y}] + B_0\hat{z}. \quad (2.22)$$

We can now break down the equation of motion into its components.

$$\vec{M} \times \vec{B} = \begin{vmatrix} \hat{i} & \hat{j} & \hat{k} \\ M_x & M_y & M_z \\ B_x & B_y & B_z \end{vmatrix} = (M_y B_z - M_z B_y) \hat{i} - (M_x B_z - M_z B_x) \hat{j} + (M_x B_y - M_y B_x) \hat{k} \quad (2.23)$$

To describe the evolution of the magnetization in the presence of interactions, Bloch assumed that the relaxation of the different components of the magnetization can be treated as 1st order processes with characteristic times T_1 and T_2 , respectively [12]. By making this assumption we can now write the components of the equation of motion as follows:

$$\frac{dM_x}{dt} = \gamma(M_y B_0 + M_z B_1 \sin(\omega_r f t)) - \frac{M_x}{T_2} \quad (2.24)$$

$$\frac{dM_y}{dt} = \gamma(M_z B_1 \cos(\omega_r f t) - M_x B_0) - \frac{M_y}{T_2} \quad (2.25)$$

$$\frac{dM_z}{dt} = -\gamma(M_x B_1 \sin(\omega_r f t) + M_y B_1 \cos(\omega_r f t)) - \frac{M_z - M_0}{T_1} \quad (2.26)$$

2.3 Relaxation Times

2.3.1 What are the relaxation times T_2 and T_2^* ?

T_2 and T_2^* are known as the spin-spin relaxation times. They describe the coherence time for the moments in the plane perpendicular to \vec{B}_0 . Over time the moments begin to de-phase and lose coherence.

One mechanism for this type of decoherence is the energy exchange between moments by conservative dipolar interactions, and is described by T_2 . This implies that $M_{y'}$ decays with a time constant, T_2 .

Another mechanism for the decoherence of the moments is that, in general, \vec{B}_0 is not perfectly homogeneous. This results in different nuclei precessing at different frequencies leading to the de-phasing of the moments. The decay of $M_{y'}$ due to the combined effects of the energy exchange between moments and the inhomogeneity of the external field is described by T_2^* .

Both mechanisms must be considered when describing the decoherence of the moments in the plane perpendicular to \vec{B}_0 , and so the two rates add as follows:

$$\frac{1}{T_2^*} = \frac{1}{T_2} + \frac{\gamma \Delta B_0}{2} \quad (2.27)$$

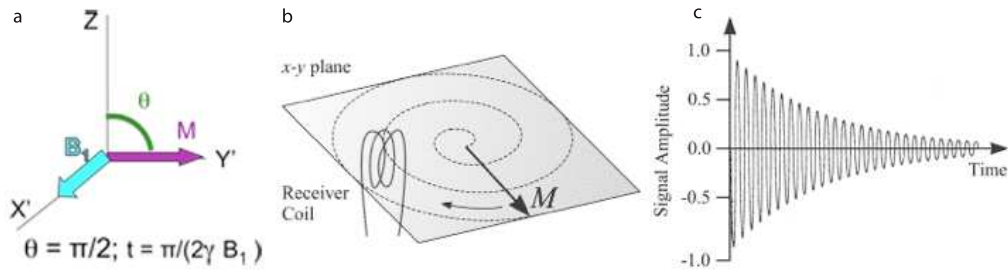


Figure 2.6: a. B_1 is applied along the x' direction for a time that corresponds to a tilt angle of $\pi/2$. b. Then the magnetization rotates around z in the $x' - y'$ plane until the magnetization in this plane is no longer coherent. Image from [13]. c. Amplitude vs. Time plot. Image is from [13].

T_2^* is found by measuring the free induction decay (FID) of the moments. The FID is measured by applying a $\theta = \pi/2$ pulse. This is done by setting $\theta = \pi/2$ in Equation 2.21 and determining the length of time that the radio frequency pulse, \vec{B}_1 , should be applied (see Figure 2.6 a).

The resulting FID is a decaying sinusoidal function. This is a direct measurement of M_y as it decays (see Figure 2.6 b).

The signal amplitude vs. time should be similar to that found in Figure 2.6 c. From the exponential decay, one can determine T_2^* as shown in Figure 2.7.

T_2 is found by using a Hahn spin echo pulse sequence: $\pi/2, \tau, \pi$ shown in Figure 2.9. By doing this, the FID is observed at 2τ as shown in Figure 2.8. This is repeated for different values of τ . To calculate T_2 , one fits to the exponentially decaying envelope created by the peaks of the free induction decay.

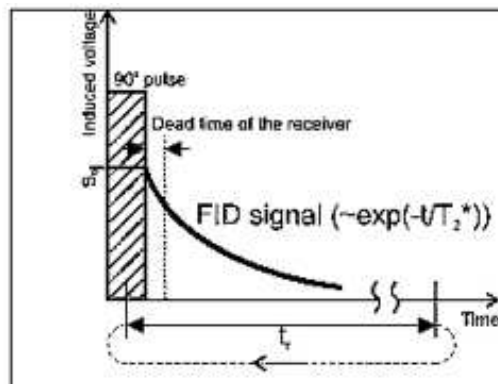


Figure 2.7: T_2^* is determined by the exponential decay of the signal.

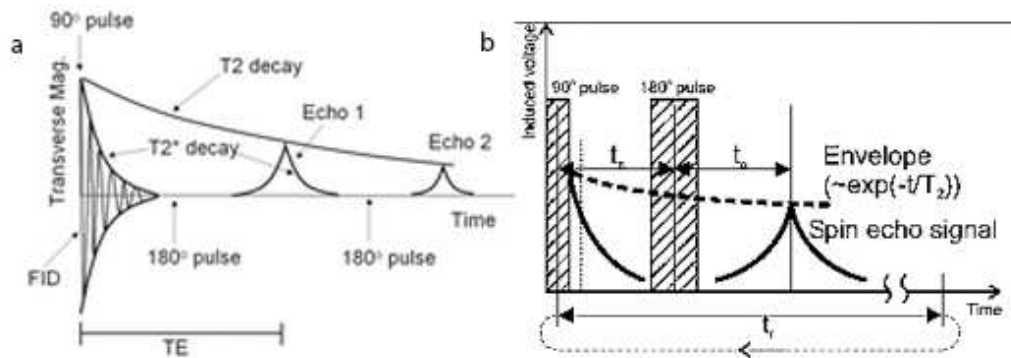


Figure 2.8: T_2 is determined by the exponential decay of the FID maxima versus τ . Image from [14].

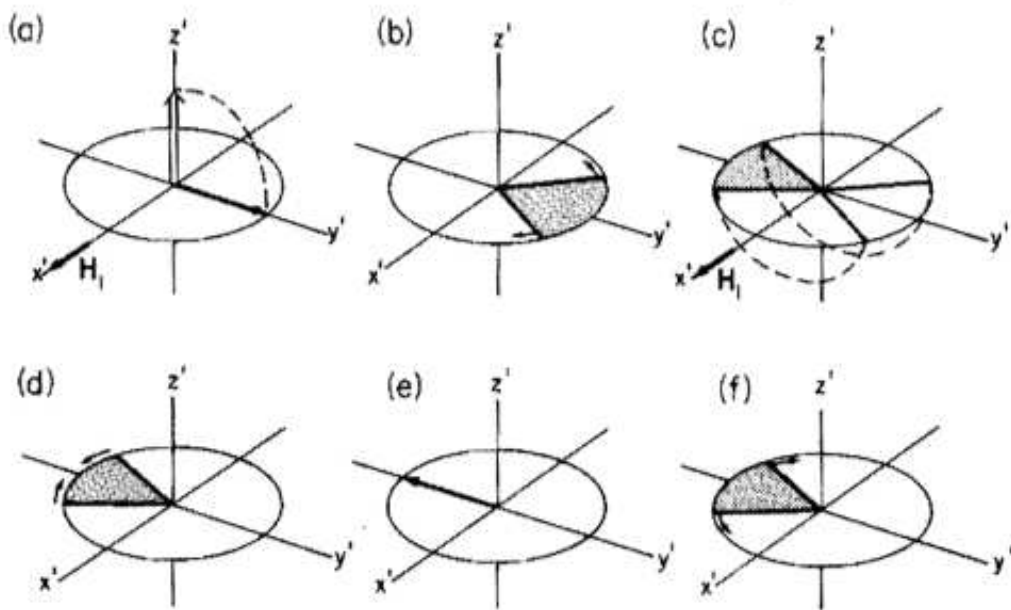


Figure 2.9: The Hahn spin echo experiment. (a) A $\pi/2$ pulse applied along x' at $t = 0$ causes \vec{M} to tip to the y' axis. (b) The individual moments, \vec{m}_i dephase due to the inhomogeneity of \vec{B}_0 . (c) A π pulse along x' at time τ causes all of the moments, \vec{m}_i , to rotate π about the x' axis. (d) The faster nuclei now go away from the observer, while the slower nuclei move toward the observer. (e) At time τ the \vec{m}_i rephase along the $-y'$ axis. (f) At $t > 2\tau$ the \vec{m}_i dephase again. From [12]

2.3.2 What is the relaxation time T_1 ?

T_1 is known as the spin-lattice relaxation time. This type of relaxation is due to moments exchanging energy with their surroundings. The result of this relaxation is that M_z relaxes back to the equilibrium value of M_0 with the time constant, T_1 . By measuring T_1 for nuclei, one can study the interactions resulting from electron paramagnetism. In metals, measuring T_1 describes the relaxation of nuclei by conduction electrons and by electron paramagnetic moments. T_1 can also be used to extract details of motion modulated dipole interactions.

T_1 is calculated by integrating the z -component of the equation of motion of the magnetization, Equation 2.26, to get:

$$M_z = M_0(1 - 2e^{-(t/T_1)}) \quad (2.28)$$

T_1 is measured by using the pulse sequence: $\pi, \tau, \pi/2$ shown in Figure 2.10 a.

This is done for various values of τ and the maximum of the free induction decay is plotted as a function of τ resulting in a plot similar to that in Figure 2.10 b. One can then fit the data to Equation 2.28 and extract the value of T_1 .

2.4 Nuclear Magnetic Resonance Experimental Set-Up

Nuclear Magnetic Resonance experiments are conducted by placing a sample inside of a radio-frequency-magnetic-field-producing coil (Figure 2.11). This sample and coil system is then placed inside of a large external magnetic

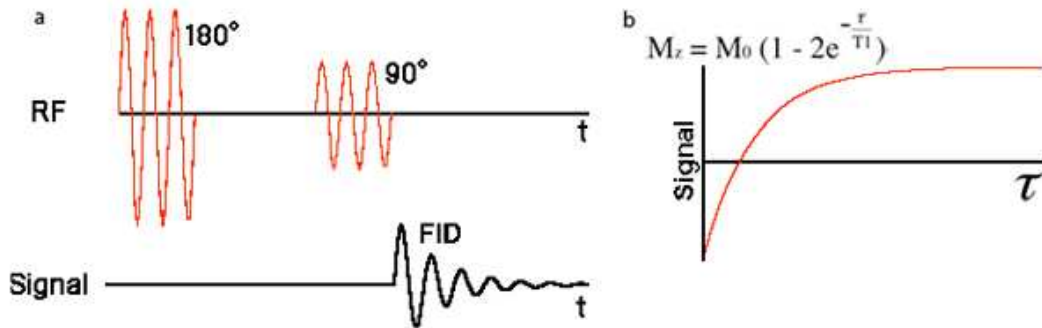


Figure 2.10: T_1 is determined by applying the pulse sequence shown in Figure 8 a. (π , τ , $\pi/2$) and then by plotting the FID maxima versus τ as shown in Figure 8b.

field, B_0 (Figure 2.12). It is placed inside of B_0 and oriented so that the field produced by B_1 is perpendicular to B_0 .

A more detailed schematic of a conventional NMR experiment is shown in Figure 2.13.

2.4.1 NMR Signal To Noise Ratio

One of the main motivators for NMR-FM comes from the limits encountered by conventional NMR when it comes to the signal to noise ratio. In both NMR and NMR-FM experiments one can use the general expression found by Rugar et al. for the signal to noise ratio (SNR) [15]:

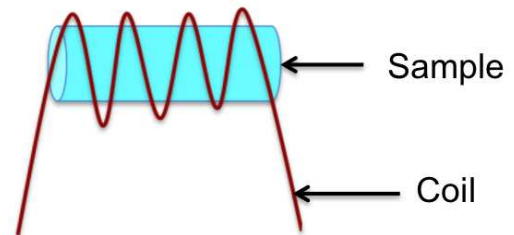


Figure 2.11: Sample is placed inside of the coil that produces the radio frequency magnetic field, B_1 .

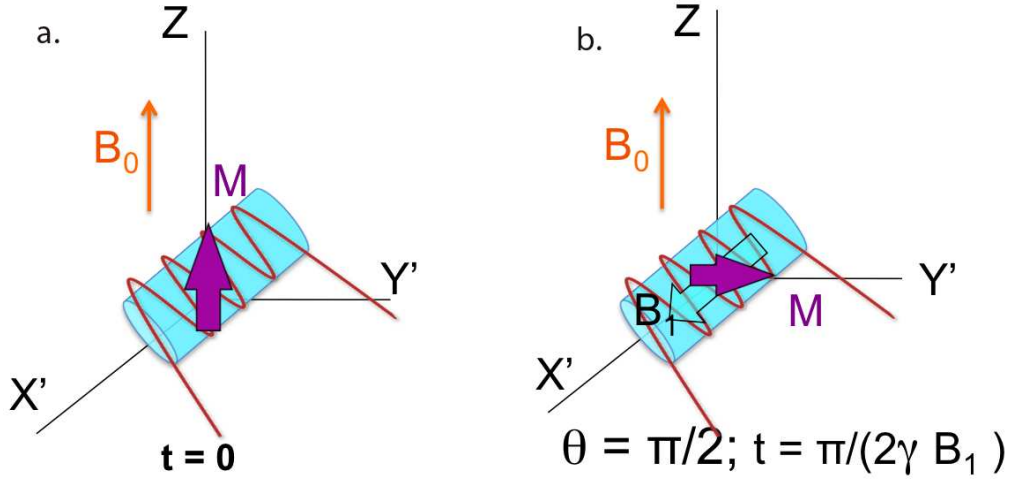


Figure 2.12: a. The magnetization of the sample along B_0 . b. The magnetization tilted by $\pi/2$ after B_1 has been applied for a time, $t = \pi/(2\gamma B_1)$.

$$SNR \propto \sqrt{\frac{\omega Q}{k_m}}. \quad (2.29)$$

In this expression, Q is the quality factor of the LC circuit,

$$Q = \frac{\omega_0 L}{R}, \quad (2.30)$$

and k_m is considered a generalized “magnetic” spring constant. In the case for NMR, one finds that:

$$k_m = \frac{L}{B_i^2}, \quad (2.31)$$

where L is the inductance of the coil and B_i is the field produced inside of the coil. The expression for the SNR in NMR can now be reduced to [16]:

$$SNR \propto \frac{\omega_0}{\sqrt{nd}}, \quad (2.32)$$

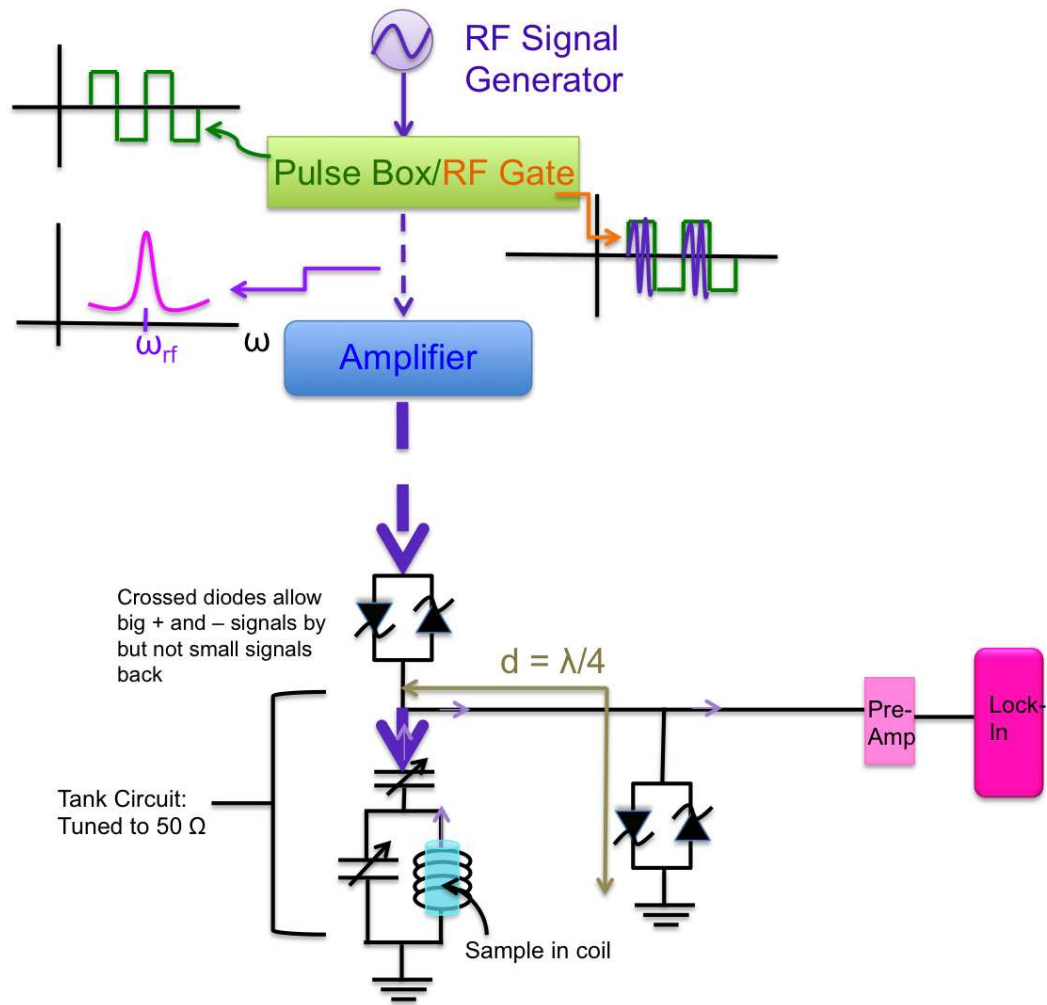


Figure 2.13: Schematic of NMR experiment.

where n is the number of turns of the coil and d is the diameter of the coil. This tells us that ultimately the SNR limit in conventional NMR is primarily due to the physical characteristics of the coil.

2.5 Nuclear Magnetic Resonance Force Microscopy (NMRFM)

NMRFM is a technique that couples the force created by an oscillating nuclear magnetization to a mechanical micro-oscillator through a field gradient. This is an NMR experiment that uses a mechanical micro-oscillator, similar to the cantilevers used in atomic force microscopy (AFM), as its detection mechanism rather than an inductive coil. This allows for the detection of a much smaller force since the sensitivity of a mechanical cantilever is much greater than that of a coil.

The idea is to consider the force on the moment:

$$\vec{F} = (\vec{M} \cdot \vec{\nabla})\vec{B}. \quad (2.33)$$

If $\vec{B} = B\hat{z}$, then

$$F_z = M_z \frac{\partial B}{\partial z}. \quad (2.34)$$

Now, we can tilt the spins onto the $x' - y'$ plane, and they will precess at a frequency ω_{rf} about the x' axis. If there is a magnetic field gradient present, the precessing magnetization will create an oscillating magnetic force at a frequency of ω_{rf} .

But how can we couple to this oscillating force using the mechanical cantilever when ω_{rf} is on the order of MHz, but mechanical cantilevers have resonant frequency typically in the kHz range? Note that a harmonic oscillator's amplitude is amplified when driven at its resonance frequency by a factor of Q ,

$$x = \frac{F_{min}}{k}Q. \quad (2.35)$$

The best way to couple the oscillating force is by making the time-dependence of the magnetization equal to that of the resonant frequency of the mechanical cantilever. In doing this, the force oscillates at the resonant frequency of mechanical cantilever as well, creating a driving force exactly at the cantilever's resonant frequency, and allowing the oscillator's amplitude to be amplified by the factor, Q , and allowing for a greater minimum force sensitivity, since:

$$F_{min} = \left(\frac{4kk_B T \Delta\nu}{Q\omega_{osc}}\right)^{1/2}, \quad (2.36)$$

where k is the cantilever's spring constant, k_B is the Boltzmann constant, T is the temperature in Kelvin, Q is the quality factor of the cantilever, and ω_{osc} is the resonant frequency of the cantilever.

2.5.1 Modulation

Selecting the correct frequency for the magnetization's time dependence is done by using Sidle's modulation technique [17]. This can be accomplished by modulating the rf field such that \vec{B}_{eff} has an oscillating z component. To do this we modulate the frequency of the rf field:

$$\omega_{rf}(t) = \omega_0 + \Delta\omega(t), \quad (2.37)$$

where $\Delta\omega(t)$ is the frequency modulation function. Now consider the resonant case when $\omega_0 = \gamma B_0 \Rightarrow \omega_{rf}(t) = \gamma B_0 + \Delta\omega(t)$. This results in an effective field described by:

$$\vec{B}_{eff} = B_1 \hat{x}' + [B_0 - \frac{\gamma B_0}{\gamma} - \frac{\Delta\omega(t)}{\gamma}] \hat{z} = -\frac{\Delta\omega(t)}{\gamma} \hat{z} + B_1 \hat{x}' \quad (2.38)$$

To determine $\Delta\omega(t)$ we use the a priori knowledge that we want M_z to oscillate in the $x' - z$ plane so that the force will do so as well. To accomplish this, we make the effective magnetic field, \vec{B}_{eff} , oscillate in the $x' - z$ plane, since the magnetization, \vec{M} , couples to \vec{B}_{eff} , if the direction of the magnetic field changes adiabatically. To do this, we set

$$\Delta\omega(t) = \Omega \cos(\omega_{osc}(t)), \quad (2.39)$$

where ω_{osc} is the resonant frequency of the mechanical cantilever. This results in \vec{B}_{eff} having a time-dependence similar to that shown in Figure 2.14.

Recall that the magnetization will only follow the effective field if \vec{B}_{eff} changes direction slowly compared to the Larmor frequency of the nucleus. This adiabatic condition is given by [17][10]:

$$B_1^2 \gg \frac{\Omega \omega_{osc}}{\gamma^2} \quad (2.40)$$

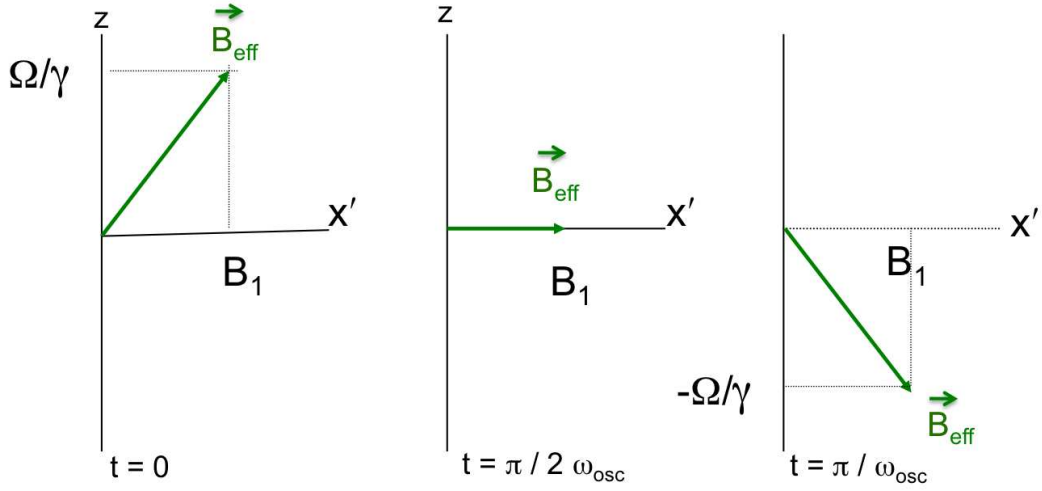


Figure 2.14: \vec{B}_{eff} at three different times.

If the adiabatic condition is met, the magnetization, \vec{M} , will couple to \vec{B}_{eff} , so \vec{M} will oscillate at ω_{osc} , and therefore, the force will also oscillate with ω_{osc} since,

$$F_z(t) = M_z(t) \frac{\partial B}{\partial z}. \quad (2.41)$$

By doing this, we are now driving the cantilever with a force at its resonant frequency and amplifying its motion by a factor of Q . This allows us to detect the force from the magnetization of the sample with the sensitivity of a mechanical oscillator.

When the adiabatic condition is met, the time-dependent expression for the magnetization can be found by replacing B_0 in Equation 2.9 by the magnitude of the z -component of \vec{B}_{eff} (Equation 2.38)[17]:

$$M_z(t) = -M_z(0) \frac{\Delta\omega(t)/\gamma}{[(\omega(t)/\gamma)^2 + B_1^2]^{1/2}}. \quad (2.42)$$

$M_z(0)$ is χ_0 by Curie's Law (Equation 2.11).

2.5.2 Nuclear Magnetic Resonance Force Microscopy Basic Experimental Set-Up

An NMRM experiment includes some of the same basic structure as a conventional NMR experimental set-up. For example, there is a large external magnetic field, \vec{B}_0 and a coil to produce a radio frequency field, \vec{B}_1 , perpendicular to the external magnetic field. However, it also includes some added parts. These are a gradient producing magnet, a mechanical cantilever, and an interferometer used to detect the deflection of the cantilever. There are two geometries possible in an NMRFM experiment. One is the magnet on oscillator configuration as shown

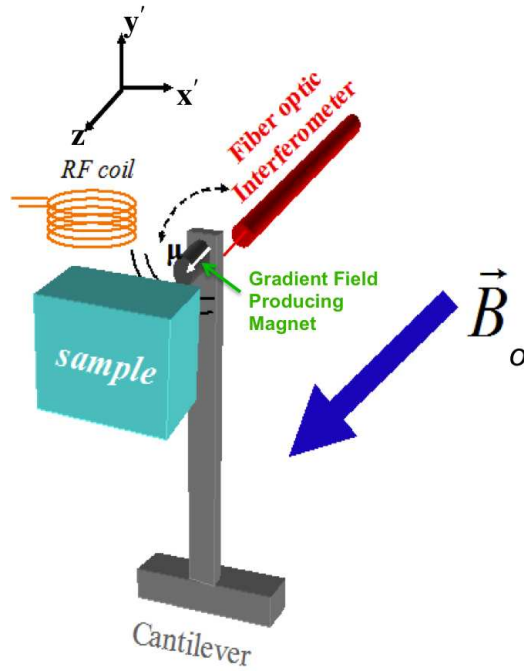


Figure 2.15: NMRFM magnet on cantilever experimental set-up.

if Figure 2.15. The other is the sample on oscillator configuration shown in Figure 2.16. These images only show the basic NMRFM experimental set-up. A detailed description of an NMRFM experiment will be presented in the next chapter.

2.5.3 NMRFM Signal To Noise Ratio

To find the signal-to-noise ratio (SNR) in the case of NMRFM we can go back to the general expression found by Rugar et al. (Equation 2.29). However, Q is now the quality factor of the mechanical cantilever and one must use a different expression for the generalized “magnetic” spring constant:

$$k_m = \frac{k_s}{G^2}, \quad (2.43)$$

where k_s is the mechanical spring constant of the cantilever and G is the magnetic field gradient,

$$G = \frac{\partial B_z}{\partial z}. \quad (2.44)$$

We are now left with an expression for the SNR in NMRFM given by:

$$\text{SNR} \propto G \sqrt{\frac{\omega_0 Q}{k_s}}. \quad (2.45)$$

This expression tells us that the limit in SNR, for the case of NMRFM, is dependent on the physical characteristics of the cantilever and on the field gradient.

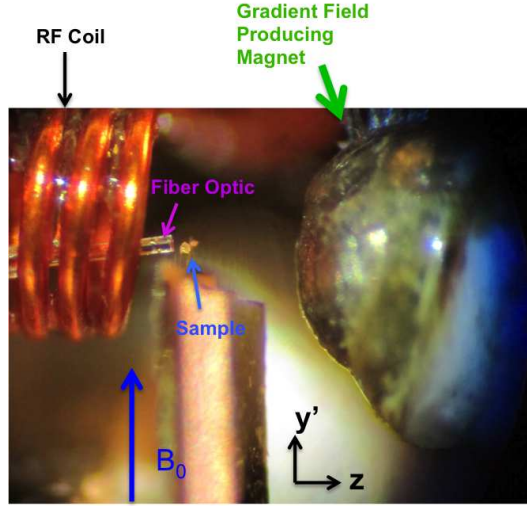


Figure 2.16: NMRFM sample on cantilever experimental set-up.

Chapter 3

NMRFM Experimental Details

3.1 NMRFM Schematic Details

Figures 3.1 and 3.2 show the schematic of an NMRFM experiment. One can see the similarities between this schematic and the one for conventional NMR shown in Figure 2.13. One can also see some major difference, the main ones being the frequency modulation in the NMRFM pulse side and most of the detection mechanism in the detection side shown in Figure 3.2. I will now explain each part of the experiment individually.

3.2 The NMRFM Pulse

3.2.1 The Pulse Box

Figure 3.1 shows how the pulses for an NMRFM experiment are generated. You start with a radio frequency signal and then that is gated into pulses of different lengths. The way this is done in this experiment is by first creating the pulses necessary for a specific experiment. For example, if we are interested in looking for T_2^* , then we would want a $\pi/2$ pulse.

For this experiment I have built a pulse programmer. The pulse programmer can generate up to three square pulses. There is an on/off switch for

each of the pulses. If the user is only interested in one pulse then they should turn off pulses two and three. It is up to the the user to check the pulses from the pulse box and make sure that they are the appropriate length. This can be done by connecting the output from the box into an oscilloscope or a Nicolet. The details of how pulses are generated by this pulse box are given in the circuit diagram shown in Figure 3.3.

3.2.2 RF Decay to Resonance and Modulation

In chapter 2 Section 5 Subsection 1, I discussed that the frequency modulation of the radio frequency signal needed to be done adiabatically. I did not, however, describe how this is done. To do this, I have a modulation box that is responsible for two things, creating a signal with a smooth exponential decay and a signal that oscillates at the resonant frequency of the cantilever. These are then added. This box creates an exponentially decaying signal with a time constant, $\tau = RC$ [18]. This signal allows for the smooth decay in frequency from far away to the Larmor frequency or radio frequency necessary to meet the adiabatic condition. When the sinusoidal signal will be allowed through depends on the settings chosen on the modulation box. The output from this box will then be put into the dc coupled radio frequency modulation connection of the HP8640B radio frequency signal generator. This allows for the modulation of the radio frequency signal at the resonant frequency of the cantilever, provided that the user sets the input frequency correctly. The modulation box details are shown in Figure 3.4. An example of the output of

NMRFM Pulse Side

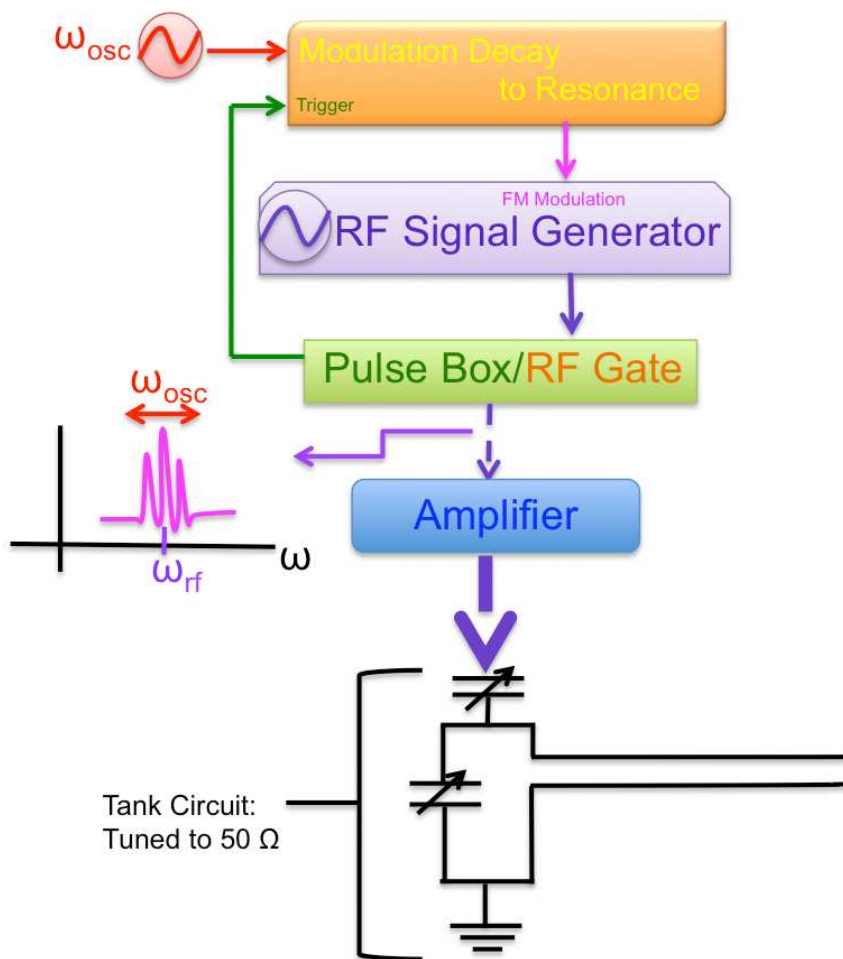


Figure 3.1: Schematic of NMRFM Experiment

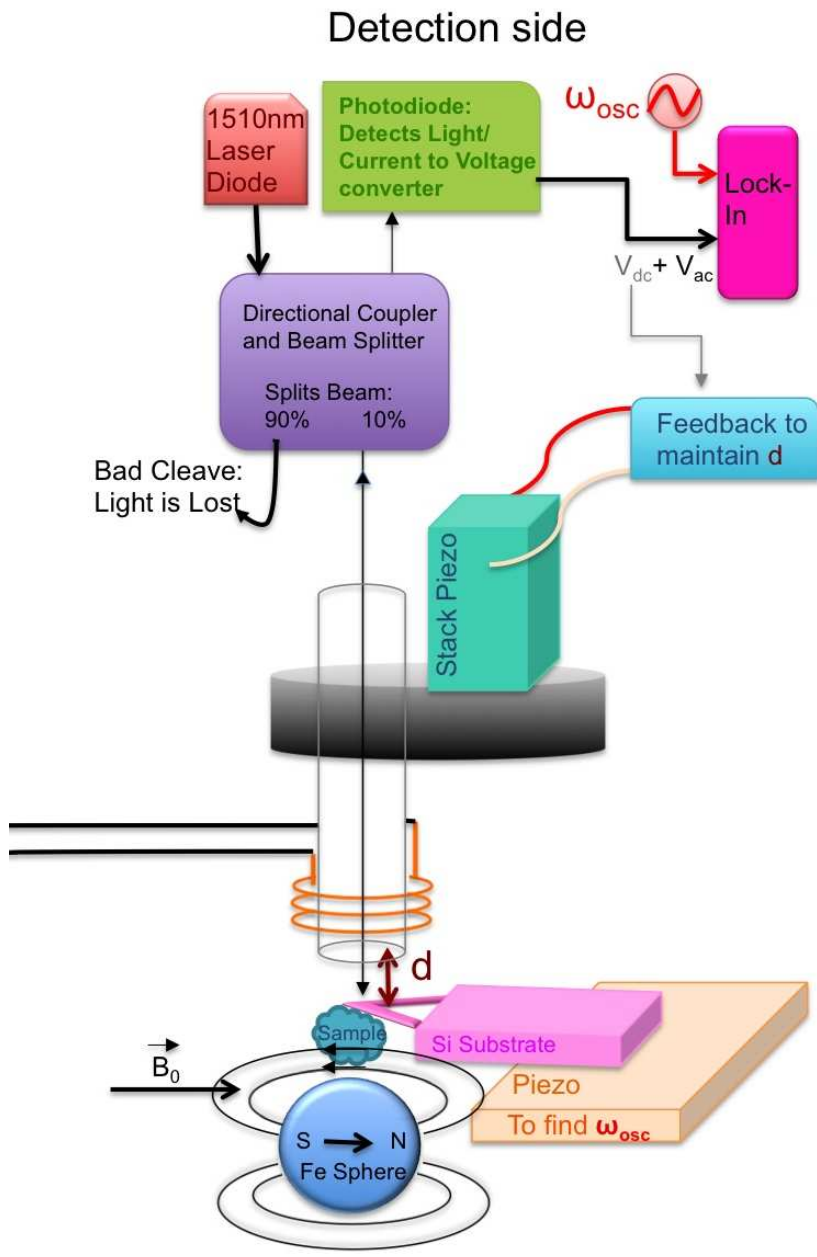
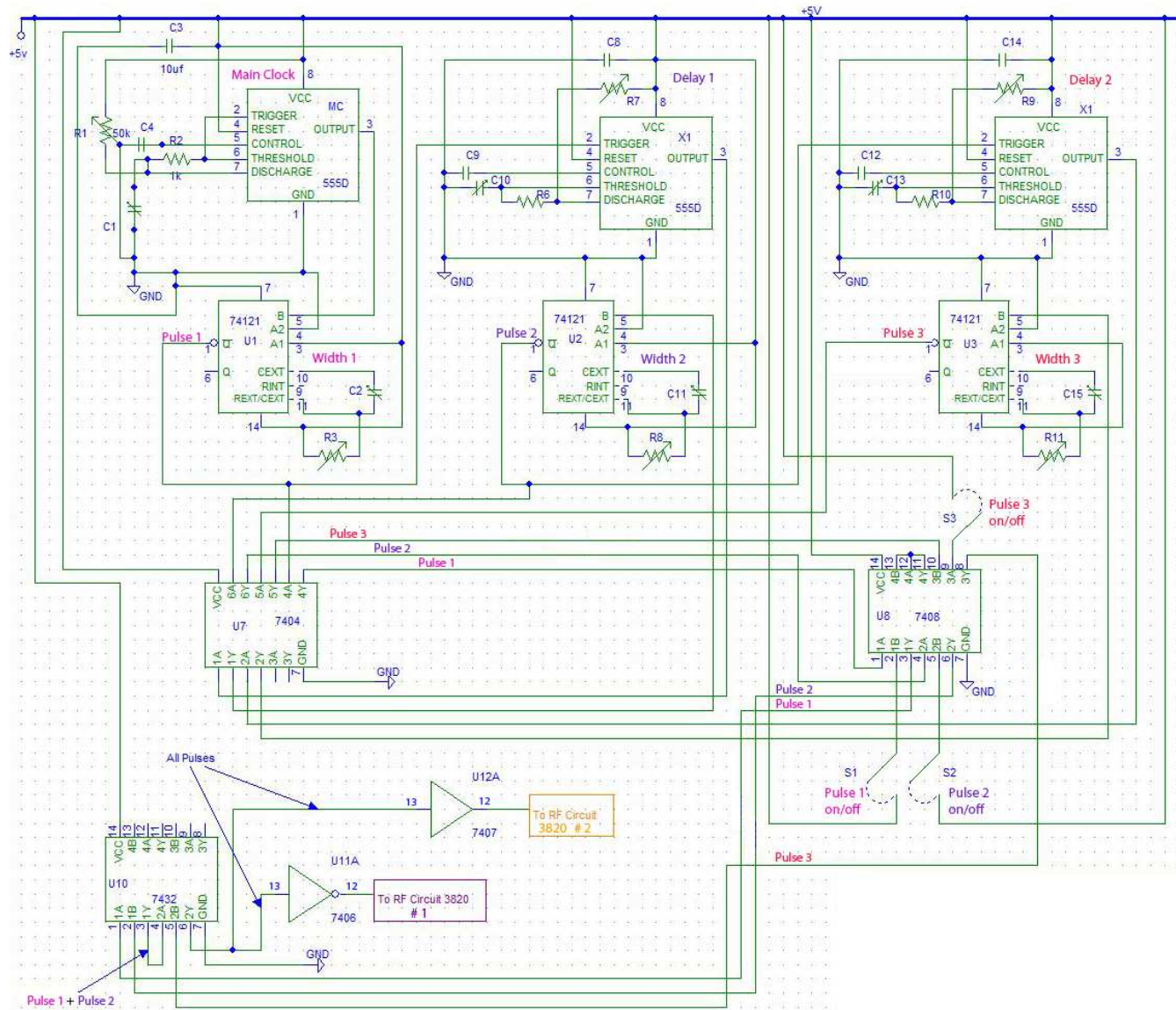


Figure 3.2: Schematic of NMRFM Experiment

Figure 3.3: Pulse Box Circuit Diagram



the pulse programmer along with the output of the modulation box is given in Figure 3.5

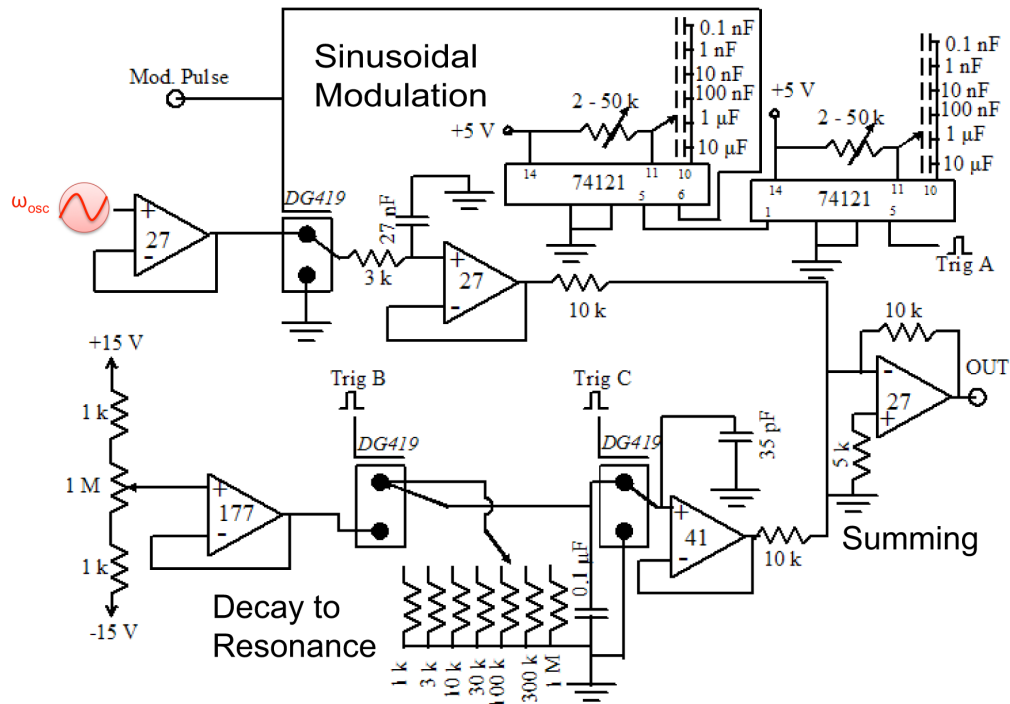


Figure 3.4: Modulation Box Circuit Diagram

3.2.3 Radio Frequency Signal Generator

The HP8640B radio frequency signal generator is used to produce the radio frequency signal and to allow for its modulation at the resonant frequency of the cantilever. The signal out of the HP 8640B may be viewed through a spectrum analyzer (Figure 3.7) with the center frequency set to that of the

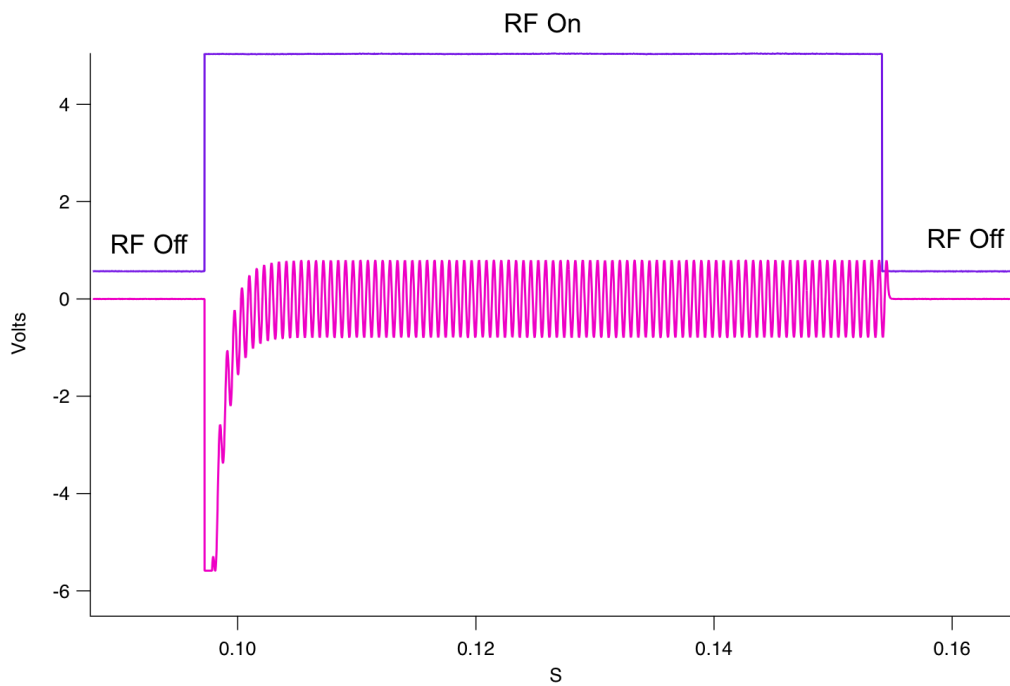


Figure 3.5: The purple curve is the output from the pulse programmer and the pink curve is the output from the modulation box. The modulation shown is at a frequency of 1607Hz because this corresponds to the resonant frequency of a cantilever.

radio frequency signal. This is shown in Figure 3.8. After the output from the modulation box is sent to the dc coupled radio frequency modulation input of the HP8640B rf signal generator one can look at the output and one see that now the signal is not just one peak at the radio frequency, but it is spread out over frequencies, where the width of these frequencies corresponds to the amplitude of the frequency modulation, typically around 100kHz for ^1H . This output is shown in Figure 3.9.



Figure 3.6: This is a picture of the pulse programmer electronics box. It is in black. The modulation box is below it.

3.2.4 The RF Gate

Once the pulses have been created, they are then routed through some transistors. The details are given in the RF circuit diagram shown in Figure 3.10. This is the step just prior to them going through the RF gate. The datasheets for components in this circuit are shown in Appendix B.

The outputs from this board go into the control inputs of the Mini-Circuits ZFSWHA-1-2C RF gate. The data sheet for the Mini-Circuits ZFSWHA-1-2C RF gate is shown in Figure B.5. The now modulated RF signal from the HP radio frequency signal generator goes into the RF In connection of the Mini-Circuits RF gate. The output from the RF gate is now a modulated radio frequency signal that is pulsed. This signal may also be viewed on a spectrum analyzer with the center frequency set to that of the radio frequency

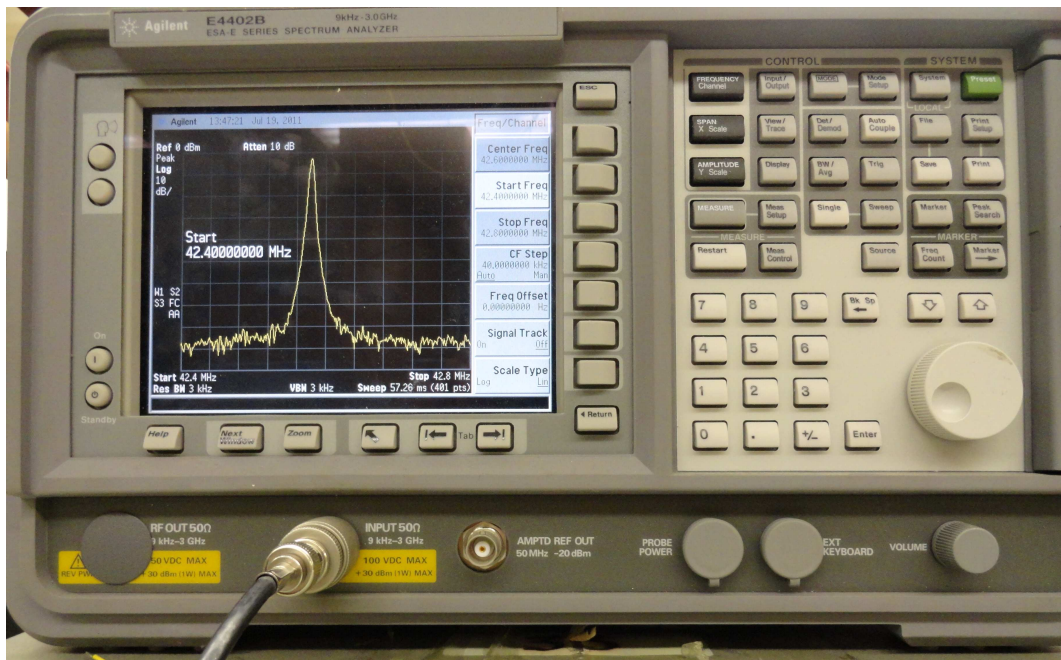


Figure 3.7: Agilent 4402B Spectrum Analyzer

signal. The result should be similar to the output directly out of the HP 8640B, only now it is not always on. It should be on and off depending on the pulse sequence that was chosen.

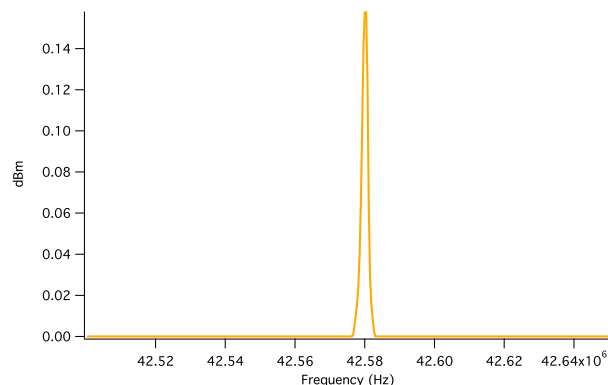


Figure 3.8: This plot shows the 42.58 MHz signal coming from the HP8640B rf signal generator.

3.2.5 The Tank Circuit

As in conventional NMR, a tank circuit is used to produce the radio frequency magnetic field, B_1 . A cartoon of the tank circuit is shown in Figures 3.1 and 3.2. It consists of two variable capacitors and a coil and should be tuned to 50Ω . This is done by viewing the impedance of the tank circuit on a smith chart on an HP 8753A Network Analyzer (Figure 3.12). The impedance is adjusted by changing the value of variable capacitors. The capacitors used must be non-magnetic, so we use ceramic variable capacitors. Figure 3.11 shows a picture of the capacitors used, and specifications are shown in Figure 3.13. The coil used is made from nyklad coated



Figure 3.11: Ceramic Variable Capacitor

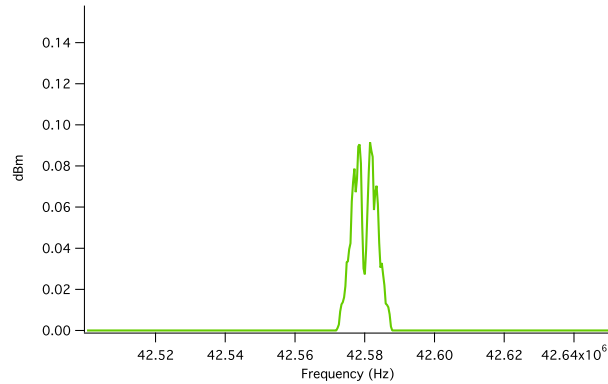


Figure 3.9: This plot shows the 42.58 MHz signal coming from the HP8640B rf signal generator when it has been modulated at 1607Hz. 1607Hz corresponds to the resonant frequency of the cantilever.

copper wire. It is s approximately .075” in diameter and consists of 10 turns. It is shown in Figure 3.14.

3.3 Signal Detection

3.3.1 The Interferometer

The signal that we measure comes entirely from the interferometer, so this is a very important part of the experimental set-up. The two most important things to maximize the signal from the interferometer are the cleave and the alignment between the fiber optic and the cantilever.

The interferometer is based on measuring the constructive and destructive interference of the laser

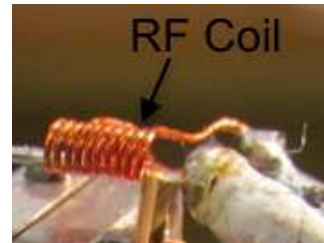


Figure 3.14: Coil

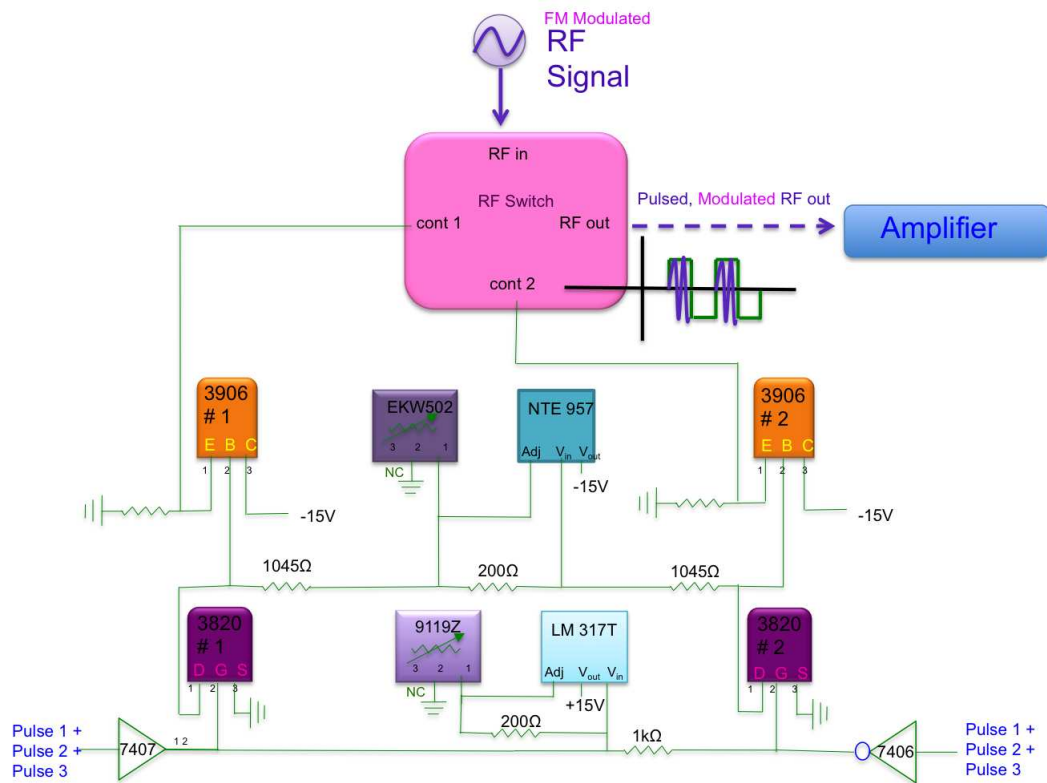


Figure 3.10: RF Board Circuit Diagram

light that is reflected from the glass/air boundary and the laser light that travels farther to the oscillator, and is then reflected. This is done experimentally by using a laser diode to produce 1510 nm laser light. From the diode the laser light goes through an optical fiber into a directional coupler which splits the beam into two.

One beam is now has 10% of the original intensity and the other is 90%. The beam that has 90% of the original intensity is sent through one optical fiber and is discarded by creating a “bad” cleave at the end of this fiber. A

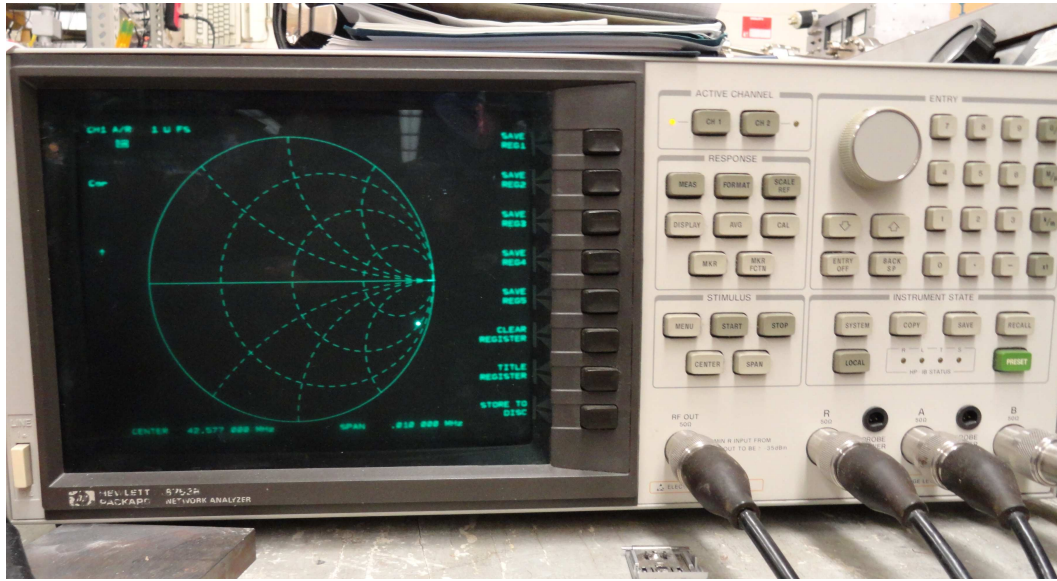


Figure 3.12: HP 8753 Network Analyzer

“bad” cleave is one at a large angle, so that little or no light is reflected. The other beam is sent through a second optical fiber and through a “good”, or nearly perpendicular, cleave. From the end of the fiber (at the “good” cleave) the light travels through vacuum and hits the cantilever. The light is then reflected from the oscillator and returns back into and through the same optical fiber. Recall that the behavior of the light beam can be represented by the Fresnel equations [19]:

$$\frac{E'}{E} = \frac{2n \cos i}{n \cos i + \frac{\mu}{\mu'} \sqrt{n'^2 - n^2 \sin^2 i}}; \quad \frac{E''}{E} = \frac{n \cos i - \frac{\mu}{\mu'} \sqrt{n'^2 - n^2 \sin^2 i}}{n \cos i + \frac{\mu}{\mu'} \sqrt{n'^2 - n^2 \sin^2 i}} \quad (3.1)$$

The incident (unprimed), refracted (primed), and reflected (doubly primed) rays and the angle at the boundary are shown in Figure 3.15

Product: NMTM120CEI

Product Line General Specifications

Product Line	Insulation Resistance	Operating Temperature	Shock	Vibration	Recommended Tuning Tool metal	Recommended Tuning Tool Ceramic
TM - Panel Mount Glass Trimmers	10 ⁴ megaohms	-55°C to +125°C	N/A	N/A	TT-100	TT-600

Min Capacitance	1
Max Capacitance	120
DC Working Voltage	1000
DC Withstanding Voltage	2000
Temperature Coefficient	0 ± 150
Q min at 1 MHz	600
Q min at 100MHz	
Self Resonant Frequency	
Torque	1.0 to 8.0 in-oz.
Mount Type	Panel Mount
Horizontal / Vertical	
Number of Turns	
Seal	YES
Rotational Life	

Example of "TM - Panel Mount Glass Trimmers"

Packaging	With Cap
MIL Designation	
Marking Color	
Is NonMag	NM

100-10 Ford Road, Denville, NJ 07834-1396

P (973)586-8585 | F (973)586-3404 | www.voltronicscorp.com | email:info@voltronics.com

Figure 3.13: Ceramic Variable Capacitor Data Sheet

The cleave is considered “good” if approximately 4% of the light is reflected at the fiber/vacuum boundary. This can easily be shown by considering the Fresnel equations for perpendicularly incident light at a boundary:

$$\frac{E'}{E} = \frac{2n}{n+n'}; \quad \frac{E''}{E} = \frac{n'-n}{n'+n} \quad (3.2)$$

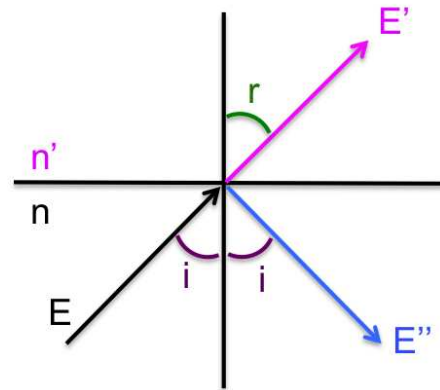


Figure 3.15: Incident Refracted and Reflected Rays

Recall that in our case, the indices of refraction are those of glass, since the fiber is made of glass with $n \approx 1.52$, and vacuum with $n' \approx 1 \Rightarrow \frac{E''}{E} = (1 - 1.52)/(1 + 1.52) = -0.52/2.52 \Rightarrow I''/I = (E''/E)^2 = 4\%$ as above.

The interference occurs between the light that has been reflected at the glass/vacuum boundary and that light that has traveled farther to the oscillator and is then reflected as shown in Figure 3.18. Both of these reflected beams then travel back through the directional coupler and are sent to a photodiode. The photodiode converts this laser light signal into a current. This current is then passed through a current-to-voltage converter and amplifier.

The signal that is outputted from the current-to-voltage converter is then measured with a voltmeter. The intensity of the signal at the photodiode depends on the relationship between the phases of the two interfering beams. The two reflected beams produce a standing wave that has an intensity, I_{diode} which is proportional to A^2 , where A is the amplitude of the standing wave [20] [21]). Therefore:

$$I_{diode} \propto A_1 + A_2 - 2A_1A_2 \cos(\Delta(d)); \quad \Delta(d) = \frac{4\pi d}{\lambda} \quad (3.3)$$

The difference in the path length traveled by the laser light is equal to $2d$, where d is the distance between the cleaved surface and the oscillator, since the light travels to the oscillator and back.

If the oscillator is not being driven, then d remains constant. This implies that the photo diode has a dc output current. However, if the oscillator is driven, the phase will depend on time because of the sinusoidally varying amplitude of the oscillator. If this is the case, then a sinusoidal current will be output from the photo diode along with the corresponding dc signal. $I_{diode} = I^{dc} + I^{ac}$. The ac current, I^{ac} , is detected with a lock-in amplifier. If the fiber is fixed, and the oscillator oscillates with an amplitude x_0 then the change of A_1 and A_2 due to the oscillation can be neglected, so therefore:

$$\Delta \rightarrow \Delta(t) = \frac{2\pi x_o}{\lambda} \sin(\omega_{osc}t) + \frac{4\pi d}{\lambda} \quad (3.4)$$

and

$$I^{ac} \propto 2A_1A_2 \cos\left(\frac{2\pi x_o}{\lambda} \sin(\omega_{osc}t) + \frac{4\pi d}{\lambda}\right) \quad (3.5)$$

In order to have the best signal-to-noise ratio the ac signal should be at a maximum. This is possible when the fiber is positioned at one of the linear sides (steepest position) of the interference fringes. This implies that d should be chosen so that there is a maximum change in $\cos(\Delta(t, d))$. Since the amplitude of oscillation, x_o , is usually much smaller than one wavelength, λ , and $4\pi d/\lambda = n\pi$, then:

$$\cos(\Delta) \rightarrow \cos\left(\frac{2\pi x_o}{\lambda} \sin(\omega_{osc}t)\right) \approx 1 - \left(\frac{2\pi x_o}{\lambda}\right)^2 \sin^2(\omega_{osc}t) \quad (3.6)$$

However, if

$$\frac{4\pi d}{\lambda} = (2n + 1)\frac{\pi}{2}, \quad (3.7)$$

then:

$$\cos(\Delta) \rightarrow \sin\left(\frac{2\pi x_o}{\lambda} \sin(\omega_{osc}t)\right) \approx \frac{2\pi x_o}{\lambda} \sin(\omega_{osc}t) \quad (3.8)$$

Thus the ac part of the interference intensity varies in direct proportion to the position.

3.3.2 Cleaving The Fiber

In order to measure the constructive and destructive interference with the interferometer we must first achieve a “good” cleave. Recall that we need a good cleave in order to reflect 4 % of the light at the fiber/vacuum boundary.

The fiber optic pigtail runs down the probe inside of teflon tubing. The pigtail consists of the fiber optic glass core coated by a thin plastic skin. This thin plastic layer is removed by placing the fiber in acetone for a few minutes and then grabbing the plastic coating with some tweezers and pulling it off. Now, the fiber core is completely exposed and ready to be cleaved. This cleaving step taken to expose the fiber is not done until after the fiber is passed through a stainless steel hypodermic tubing, which is used to hold the fiber in place. If it was done afterwards, then the fiber core could be damaged or broken while trying to get it through the tubing. The fiber running through the stainless steel tubing is shown in Figure 3.16

The cleaving of the fiber core is done with a special cleaving tool. The fiber is placed in a slot, and then the top of the cleaver, which has a ceramic blade, is pressed down to score the fiber. Once this scoring has been made, you take the fiber out of the cleaver, take some tweezers and hold the very end of the fiber between them. Now, you break off the end of the fiber by bending it with the tweezers. It feels like a little snap. In theory, you should now have

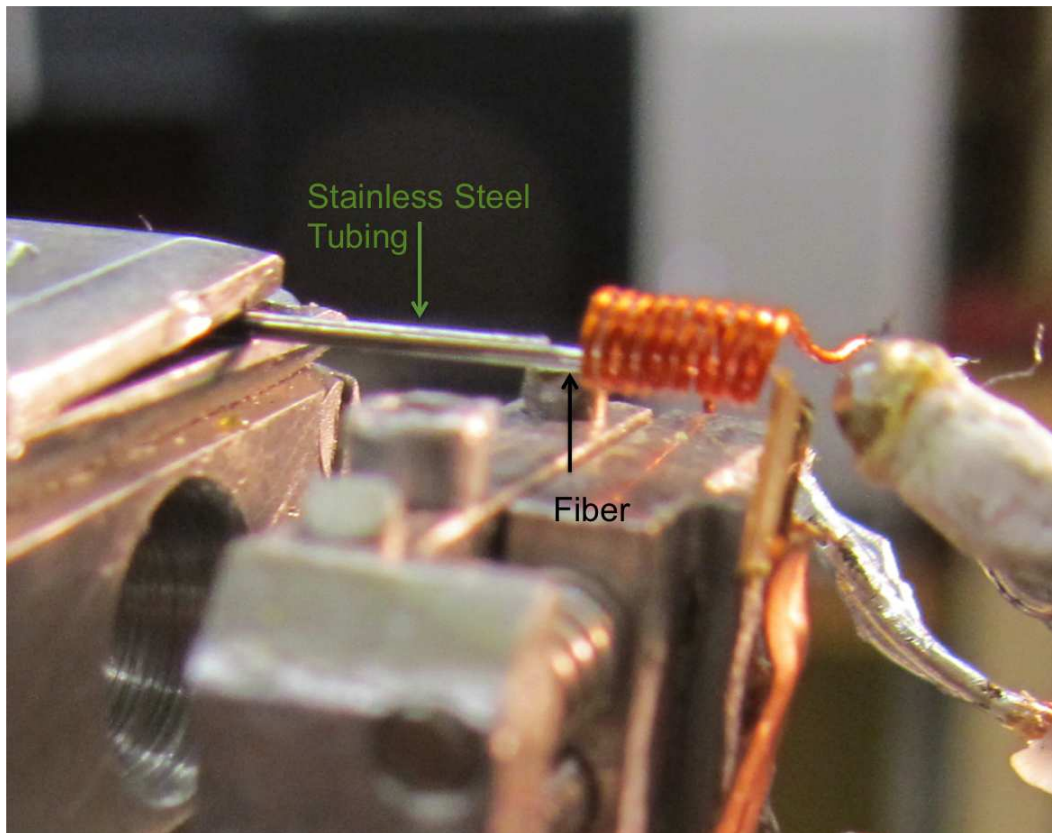


Figure 3.16: Stainless Steel Tubing

a good cleave, but you have to make sure it is “good”. If the cleave is not “good”, you must repeat the cleaving of the fiber core until it is.

Determining whether or not the cleave is “good” is a little tricky. To check if the cleave is “good” we measure what the output signal is without having the light be reflected by anything other than at the glass/air boundary. Note that this is done before the laser is placed in the vacuum where the oscillator is mounted. This has to be done before anything else because it

is important that the cleave be “good”, so that the reflected signal is large enough to make a measurement. So to make this check we begin by making a prediction of what the output voltage value of the photodetector should be. To do so we make a calculation which includes a predicted power output value after the beam is split, and that accounts for the gain of the photodetector circuitry. The calculation goes as follows: First, we know the power of the laser before the beam is passed through the directional coupler/beam splitter by looking at the specifications of the laser; it is approximately $1000 \mu\text{W} \sim 1$ milliwatt. The power of the laser (photodiode) can be double checked by using a home made laser power meter. Even though this is not the most accurate method of measuring power, it helps to make sure that the laser diode is working properly. Note that the laser diode is very sensitive and that the can should not be pulled out from its socket.

From the laser diode, about 20% of the laser power is typically coupled into the fiber. The laser light then passes through a directional coupler and a beam splitter that divides the power into 10% and 90%, i.e. a 10/90 beam splitter. Thus the laser power that reaches the end of the fiber, after the beam has been split, should be about 2% of the initial power value. We can use the home made laser power meter again to measure the power of the laser after the beam has been split. We found this power to be approximately $20 \mu\text{W}$ at the “good” cleave end. After the beam is split the light reflected at the glass/air boundary is returned through the fiber and is sent to the photodetector. If the cleave is “good one can assume that about 4% of the light is reflected; 20

$\mu\text{W} \times .04 = 0.8 \mu\text{W}$ in my case.

After this reflection occurs, the light travels back through the beam splitter, so now we must divide the reflected power by 10. In my case, I now have a $0.8 \mu\text{W} / 10 = 0.08 \mu\text{W}$ signal that has made it to the photodetector. The photodetector now converts this power into a current, its specifications indicate a conversion of $0.3\text{A}/\text{W}$, so my signal becomes $0.08 \mu\text{W} \times 0.3\text{A}/\text{W} = 0.024 \mu\text{A}$. The signal is passed through a current-to-voltage converter which converts the current into a voltage and also amplifies the signal. The photodetector circuitry uses a resistance of $83 \text{ k}\Omega$ for the current-to-voltage converter plus an additional gain 100 amplifier. Thus an estimate of the output voltage of the photodetector is obtained by multiplying the current by $.83 \times 10^7 \Omega/\text{A}$. This corresponds to a $0.024 \mu \text{ A} \times 1.667 \times 10^7 \Omega/\text{A} \sim .2\text{V}$ signal in my case. So for a “good cleave I expect a signal from the photodetector circuitry (i.e. the output signal) that is approximately .2V. If the output signal is much less than that then re-cleaving the fiber is necessary. This $\sim .2\text{V}$ output value that we read is called the fiber-only DC level.

3.3.3 Alignment

Once a good cleave has been established we then need to align the fiber with the cantilever. The alignment needs to be done with care so that the fiber does not crash into the cantilever. Crashing into the cantilever may result in the destruction of the “good” cleave as well as in the damage of the cantilever.

In order to align the fiber with the cantilever, we have to use a micro-

translational stage that can be adjusted in three dimensions. A picture of the mechanical $x - y - z$ stage is shown in Figure 3.17. Only one stage is necessary, and either the fiber or the oscillator can be mounted on the microtranslator in order to make the necessary adjustments. One could also have both the fiber and the oscillator mounted on a translator so that both can be adjusted simultaneously. Recall that what we are measuring here is the interference between the light that is reflected at the fiber/air boundary and that light which travels to the oscillator and is then reflected. The DC level of the output signal helps determine if the fiber is aligned. We know what the DC level should be for a good cleave if there is no light reflected other than the light that is reflected at the glass/air boundary. Now, if there is light that is reflected from the oscillator, the DC level should change depending on how much more light is being sent back through the fiber and whether there is constructive or destructive interference. To maximize the amount of light that makes it back through the fiber after having been reflected by the oscillator, the fiber should be placed very close to the oscillator. The laser light spreads with distance with approximately an 8 % divergence, so we want to make sure that we reflect as much of the light as we possibly can so that the signal we read is as large as possible. This implies that the fiber needs to be within approximately 10 μm . We look through a microscope as we are aligning the laser to check if the laser beam is on the oscillator. A good reference for checking if the fiber is close enough to the oscillator by sight is if the distance between the fiber and the oscillator is appreciably smaller than diameter of

the fiber, 100 μm . To verify the alignment, we measure the size of the fringe by adjusting the piezo voltage. The fiber is mounted onto a piezo whose size can be adjusted by changing the voltage applied to it. By changing the voltage across the piezo, the distance between the laser and the oscillator is decreased or increased resulting in either constructive or destructive interference of the light that is reflected at the glass/air boundary and the light that is reflected at the oscillator. I found that a fringe of approximately 3 volts peak-to-peak was the best that I could usually get. Note that each peak-to-peak voltage change corresponds to the oscillator moving $\lambda/4$.

3.3.4 Feedback by the Fringe-Lock Circuit

Once the alignment has been made, we can now apply a dc voltage to the z piezo and change d as shown in Figure 3.18. As d changes, we go through an interference fringe and see the DC level measurement from the interferometer increase and decrease. The electronics used to go through a fringe is the fringe-lock circuit. A circuit diagram is given in Figure 3.19. It not only allows the option to go through a fringe by applying -15V to +15V to the P - (white) lead of the piezo, but it also permits the capability of locking on a specific voltage of the fringe.

In order to find the resonant frequency of the cantilever we must do a driven scan. During a driven scan, we would like to remain on the same point of the fringe. Particularly, we want to remain on the linear portion of the fringe so that the measured intensity changes will be directly proportional

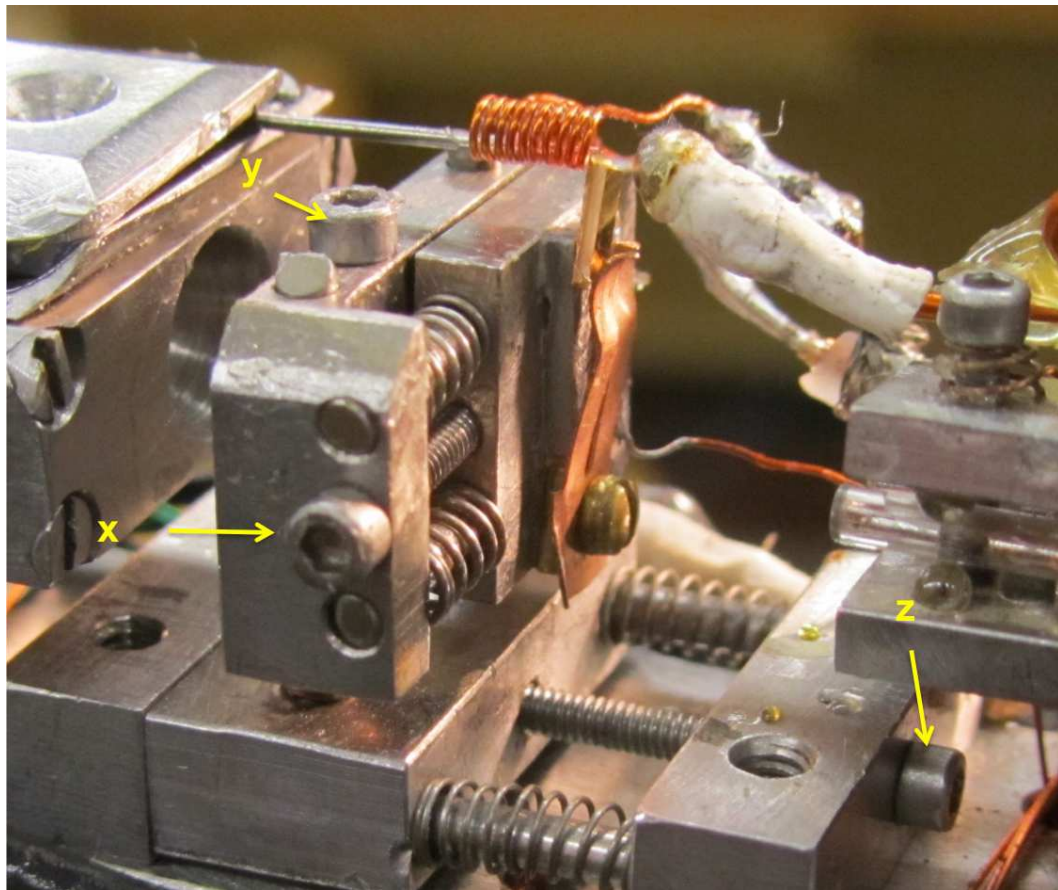


Figure 3.17: Mechanical $x - y - z$ Stage

to the position. This is nearly impossible to accomplish since there are many fluctuations occurring. However, remaining along the linear part of the fringe can be done by using the fringe-lock circuit. The fringe-lock circuit P+ and P- are connected directly to the stack piezo. This implies that the length of the piezo is controlled directly by the fringe-lock circuit. The fiber is directly mounted onto the piezo, and therefore the fringe positioning is also controlled

by the fringe-lock circuit. The fringe-lock circuit works by manually setting the DC level of the middle of the fringe, and then the fringe-lock circuit maintains it at that level. The output of the photodetector is directly imputed into the fringe-lock circuit and it adjusts P- so that the length of the piezo is such that the position of the oscillator remains in the linear part of the fringe.

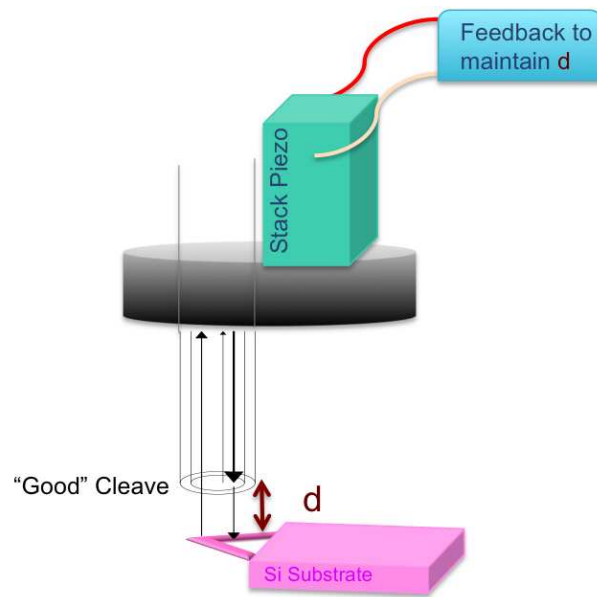
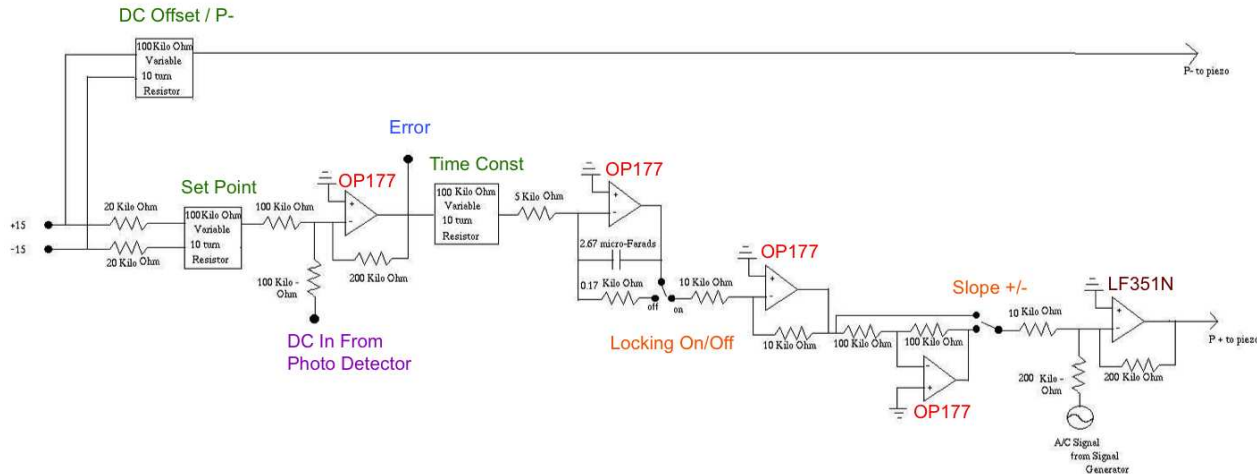


Figure 3.18: Here one can see the interference of the laser light that reflects at the glass/vacuum boundary and the light that travels to the cantilever and then back. The interference occurs when as voltage is applied to the z piezo since this determines the distance, d , between the cantilever and the interferometer.

Figure 3.19: Fringe-Lock Circuit Diagram



Chapter 4

NMRFM Experiment and Results

4.1 La Flaca

La Flaca is what I named the room-temperature NMRFM probe that I inherited from Utkur Mirsaidov. A picture of the probe is found in Figure 4.1. It is a nice probe with a mechanical $x-y-z$ stainless steel stage used for positioning the cantilever with respect to the fiber. In this image one can see most of the parts necessary to conduct an NMRFM experiment. Not visible in this picture are the ceramic variable capacitors necessary to tune the tank circuit. They are located at the bottom of the probe as shown in Figure 4.2.

In the process of preparing to conduct an experiment using this probe I broke almost every single part. I eventually replaced the z feedback piezo, ball magnet, coil, capacitors, and fiber. I also had to re-build the fringe-lock circuit, the pulse programmer, and the modulation electronics. Once I was ready to put a sample in the probe it came time to decide what to analyze. We decided to analyze ammonium hexafluorophosphate, NH_4PF_6 .

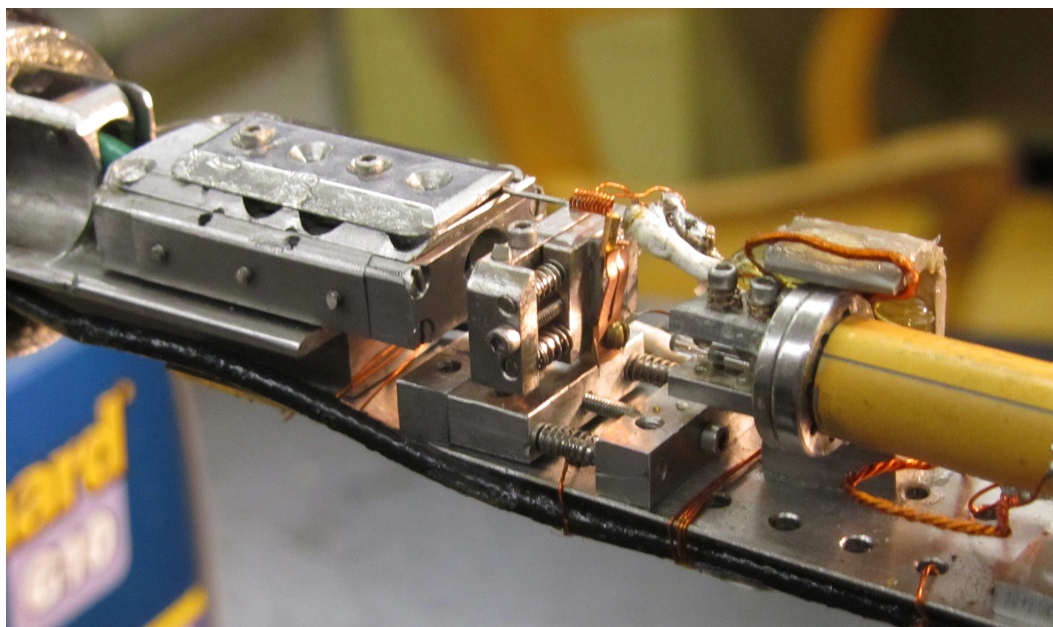


Figure 4.1: This is a general view of the probe that I inherited from Utkur.

4.2 Ammonium Hexafluorophosphate, NH_4PF_6

Ammonium hexafluorophosphate is a sample with a high concentration of hydrogen and fluorine. Both of these elements have magnetic moments large enough to detect by using nuclear magnetic resonance techniques and are therefore excellent candidates for analysis by nuclear magnetic resonance force microscopy. A cartoon of NH_4PF_6 is shown in Figure 4.3. The gyromagnetic ratio of hydrogen, γ_H , is 42.58 MHz/Tesla and the gyromagnetic ratio of fluorine, γ_F , is 40.06 MHz/Tesla. From these values along with the selection of the rf frequency to 42.58 MHz and the calculation of the field gradient from the iron ball magnet at the sample location, we can calculate the expected

resonant field for a particular element. An illustration of the magnetic fields at the sample is shown in Figure 4.4. For the case of my experiment I was able to estimate $B_z(d)$ to be 0.22 T from the analysis made by Utkur [18] shown in Figure 4.5.

Now I was able to make an approximation of the value of the field necessary to satisfy the resonant condition for both hydrogen and fluorine. In the case of hydrogen, where $\omega_{rf} = 42.58$ MHz, $\gamma_H = 42.58$ MHz/T, and $B_z(d) = 0.22$ T, I found:

$$\omega_{rf} = \gamma_H(H_H - B_z(d)), \quad (4.1)$$

which implies that

$$H_H = 1.22 \text{ T}. \quad (4.2)$$

In the case of fluorine, where $\omega_{rf} = 42.58$ MHz, $\gamma_F = 40.06$ MHz/T, and $B_z(d) = 0.22$ T, I found:

$$\omega_{rf} = \gamma_F(H_F - B_z(d)), \quad (4.3)$$

which implies that

$$H_F = 1.284 \text{ T}. \quad (4.4)$$

So under these conditions I would expect to see a peak in the response of the cantilever at 1.22 T for hydrogen and then at 1.284 T for fluorine.

4.3 NMRFM Experimental Set-Up for Ammonium Hexafluorophosphate

The experimental set-up for the analysis of ammonium hexafluorophosphate is shown in Figure 4.6. In Figure 4.6 (c) one can see how the optical fiber and the mechanical cantilever need to be aligned in order to get a signal. In this image one can also see the coil used to produce the radio frequency field, \vec{B}_1 , the iron spherical magnet used to create a magnetic field gradient in the sample, and the sample mounted directly on the cantilever.

The most difficult parts of getting the experiment to this point are mounting the sample on the cantilever, making sure that the fiber cleave remains intact as it is installed through the rf coil, and (the most difficult part) maintaining alignment of the fiber with the cantilever as you sweep the magnetic field.

Mounting the sample is done carefully by using a piece of an optical fiber that is mounted on an $x - y - z$ stage. Under the microscope you first attach a small amount of silver epoxy to the cantilever. Then you place some sample on the silver epoxy. The epoxy can then be cured. Once the sample is mounted to the cantilever you place the cantilever in the clamp on the $x - y - z$ stage and align.

The next part is putting the probe in the big red electromagnet, El Gordo. Detailed instructions for powering up the big red magnet can be found in Appendix C. After moving the probe into the magnet the alignment will most likely be off, so be prepared to re-align. Once the probe is in the magnet

and aligned the vacuum can must be put on and the probe should be evacuated. Keep your fingers crossed that pumping does not also lead to misalignment of the fiber with the cantilever. Now once the probe is aligned in the magnet and evacuated we can begin.

4.4 NMRFM Ammonium Hexafluorophosphate Scan Results

I first found the resonant frequency of the cantilever with the mounted sample by driving the cantilever at an average position that has been locked on the linear part of the interference fringe. Figures 4.7 and 4.8 show plots of driven scans using different driving amplitudes. This should be done just prior to doing an experiment because this resonance frequency needs to be accurate in the modulation of the radio frequency pulse. If the radio frequency pulse is not modulated at the correct frequency then our cantilever will not respond to it and we will not be able to collect any signal.

The response of the cantilever fits a Lorentzian. Please note that this is actually the square root of the sum of the squares of each phase of the signal. The driven scan response of each phase is shown in Figure 4.9.

Now that the resonant frequency is known, a signal with this frequency is sent to the modulation box as shown in Figure 3.1. I also set the length of the rf pulse to 150 ms. The output from the modulation box is similar to that shown in Figure 3.5. The output from the modulation box will then be sent the dc coupled radio frequency modulation input of the HP8640B rf signal

generator to create the modulated rf pulse. Now the modulated rf signal will be passed through the rf gate so that it is pulsed. From the gate it goes to the 40 dB amplifier and then to the tank circuit. Remember that the tank circuit needs to be tuned to 50Ω as is explained in Chapter 3, Section 2, Subsection 5 before sending a signal to it.

I sent a pulse once every 10 s and measured the cantilever response with an SRS830 Lock-In Amplifier. The cantilever's response in the absence of an NMR force to the pulse is known as the artifact effect and I call the curve measured an artifact. I collected the data from the lock-in with a Nicolet. Artifact data was averaged and collected as I swept the field. A set of artifact curves are shown in Figure 4.10. Each curve corresponds to a specific phase of the signal.

As shown in Equations 4.2 and 4.2, I had already calculated where I expected to see the resonance peaks for hydrogen and fluorine so I started the field sweep at 1.16 T, well below the expected resonant value for hydrogen and ended it at 1.325 T, well above the expected resonant value for fluorine.

So for each field I collected artifact data. For example, the artifacts shown in Figure 4.11 are for a field of 11.60 T and for 11.65 T. Each one has a slightly different minimum.

In a given field sweep, I collected over a hundred sets of data since I took a measurement every 10 Gauss. The data was transferred from the Nicolet to a computer using IgorPro. Once the files were imported, I wrote

a program in IgorPro that found the minimum and maximum value of each artifact. This program is shown in Figure 4.12.

This program then writes the value found to a new array. Figure 4.13 shows a partial table of the minima and maxima found for each artifact.

From here I plotted the values of the maxima vs the applied field as shown in Figure 4.14. The values of the maxima here were not normalized with respect to the size of the fringe, so I then normalized the data by dividing the maxima by the fringe size as shown in Figure 4.16

The result is shown in Figure 4.15. In this data one can see two peaks. The first most likely corresponds to the hydrogen resonance. The second may correspond to fluorine.

4.5 Probe Limitations

Although this probe was functional, it was not user friendly. The main drawbacks to it were the mechanical positioning stage used for the alignment of the cantilever with the fiber. For example, in moving the the probe from outside of the magnet to inside of the magnet, the alignment would be lost and it would need to be re-aligned. Also, as the magnetic field was swept, there would be some slight shifting of the components and the alignment would also be lost. Many times during a field sweep, I had to break vacuum to re-align and then continue. This made conducting an experiment very challenging.

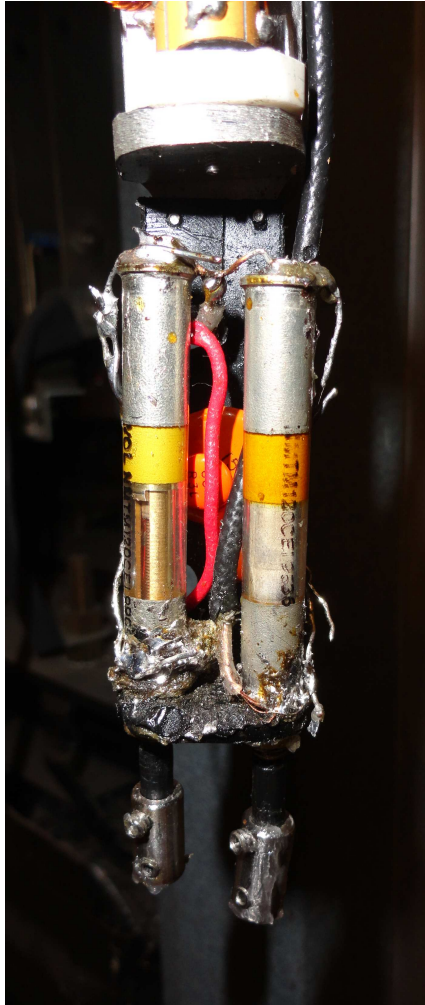


Figure 4.2: These are the variable capacitors that have been mounted at the bottom of this probe.

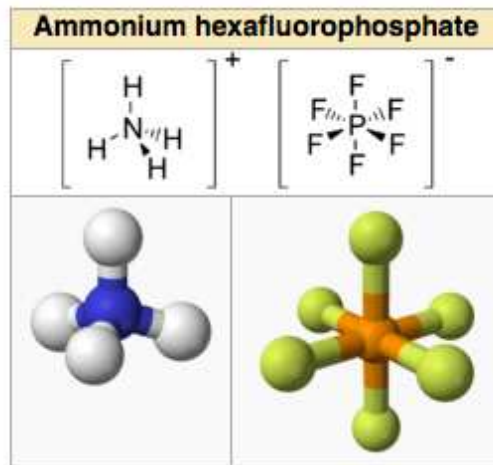


Figure 4.3: This is a ball and stick figure of ammonium hexafluorophosphate.

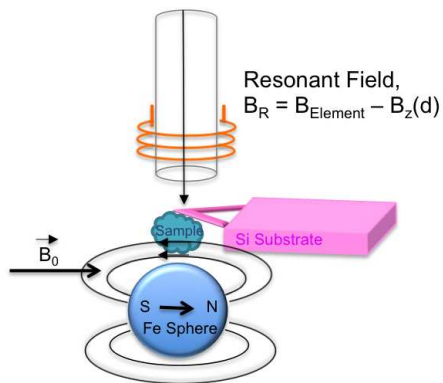


Figure 4.4: Here one can see that B_0 and the field from the iron ball magnet are in opposite directions and must subtract.

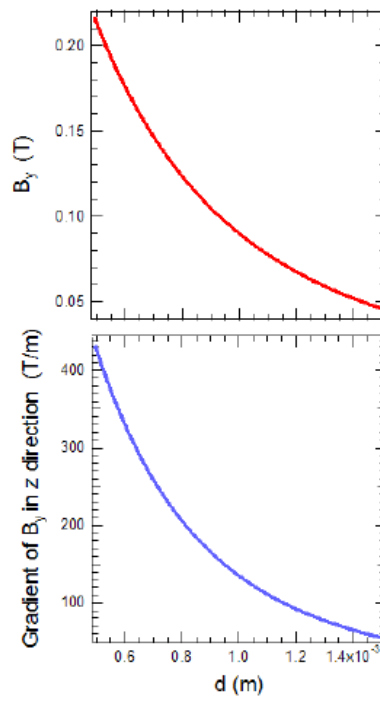


Figure 4.5: In this plot we can see what the value is of the magnetic field vs. the distance the sample is from the magnet. From [18].

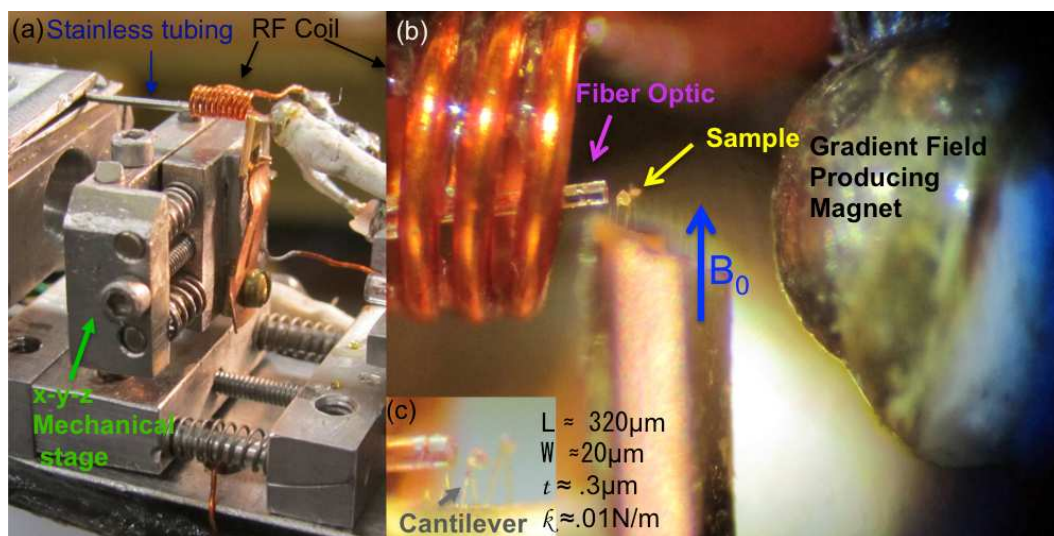


Figure 4.6: (a) Mechanical stage used for aligning the cantilever to the fiber in this room-temperature NMRFM probe. (b) A zoomed in picture of the fiber and cantilever that must be aligned. (c) Further zoom of optical fiber and cantilever.

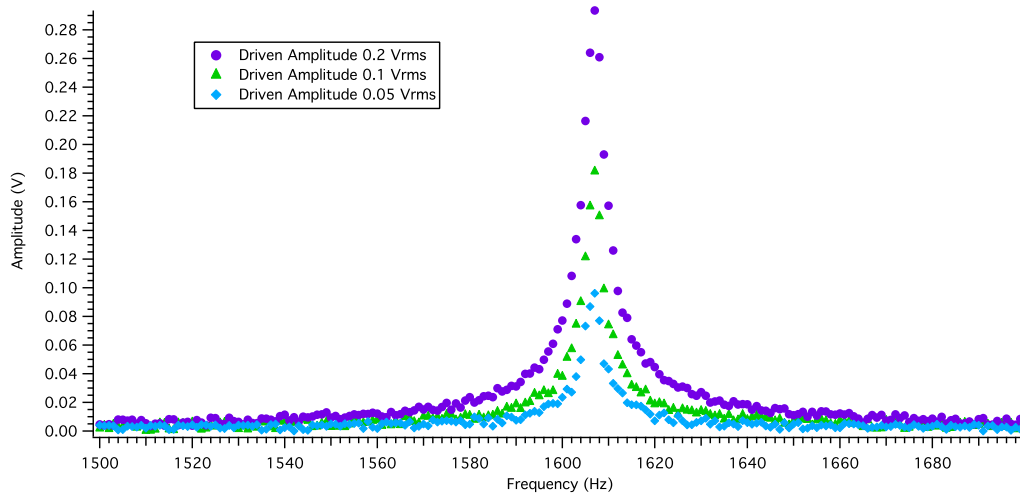


Figure 4.7: Driven scans of the cantilever with the ammonium hexafluorophosphate sample mounted. It has a resonant frequency of approximately 1607 Hz and a Q of approximately 250.

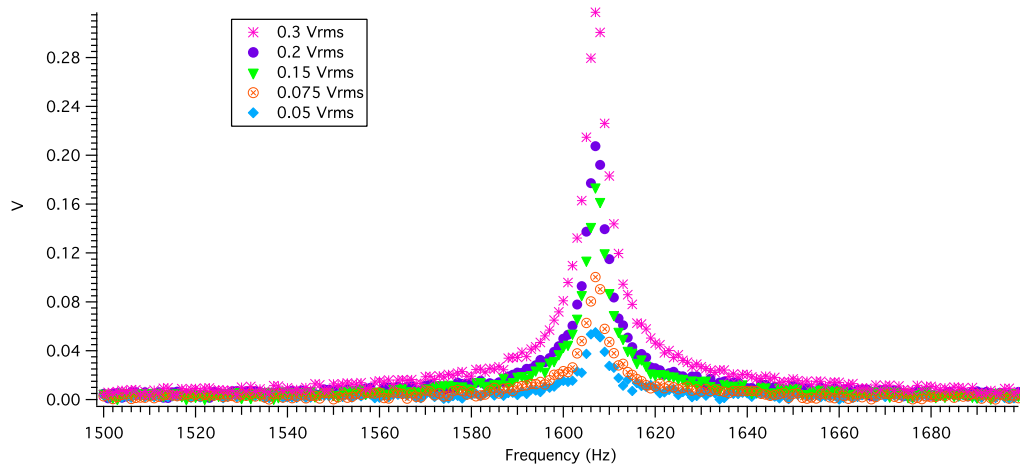


Figure 4.8: These are also driven scans of the cantilever with the ammonium hexafluorophosphate sample mounted. These were taken on a different day. We see that the cantilever still has a resonant frequency of approximately 1607 Hz and a Q of approximately 250.

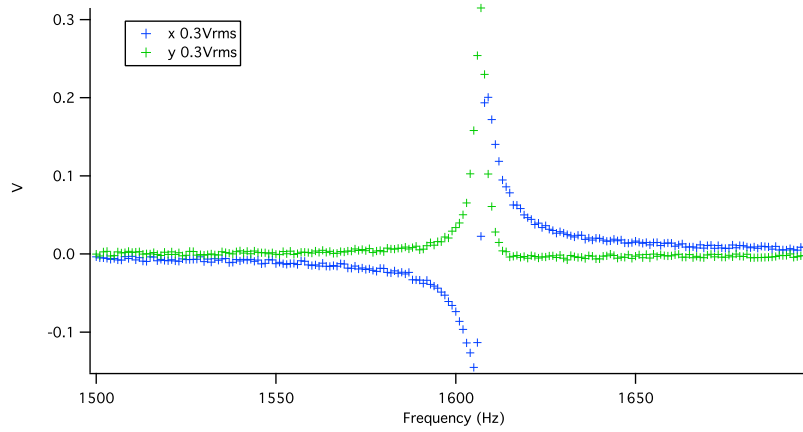


Figure 4.9: This shows the x and y components of the signal measured by the lock-in.

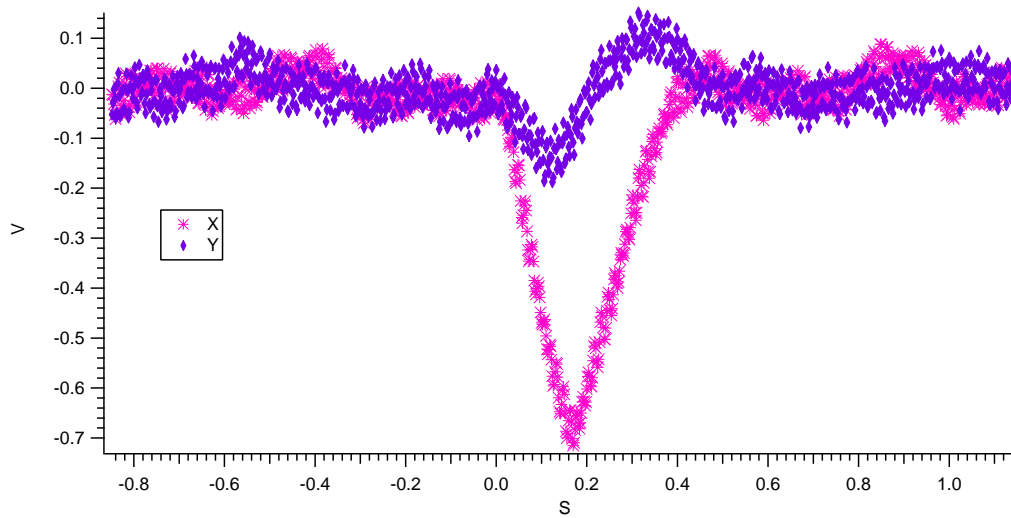


Figure 4.10: This shows the x and y components of the artifact.

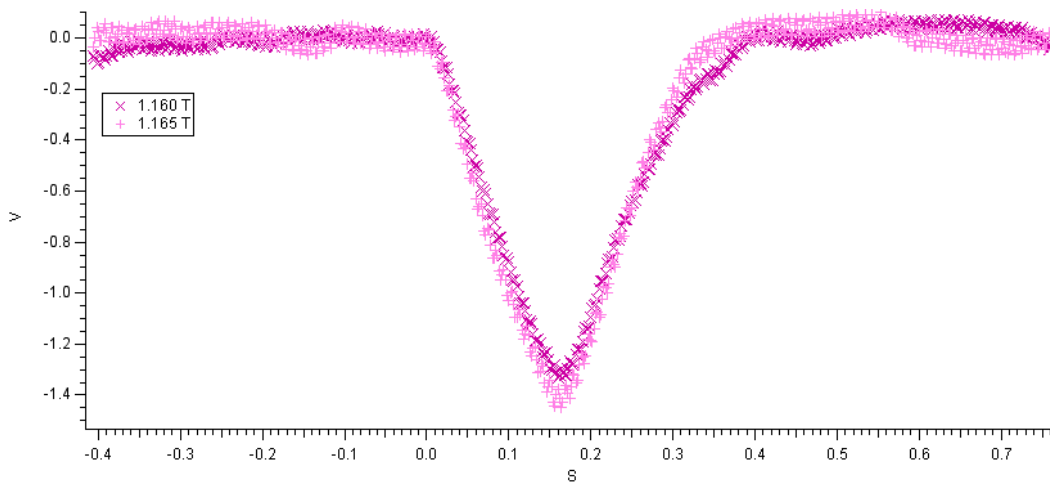


Figure 4.11: Artifacts for different magnetic field values.

```

Xmax
#pragma rtGlobals=1      // Use modern global access method.

Function FindXmax()

Variable i = 24
do
  String oneName = "wave"+num2str(i)
  Wave/Z w = $oneName
  if (!WaveExists(w))
    break // no such wave- get out of the loop
  endif
  WaveStats/Q/R=(-0.1,0.3) w
  Print V_max
  i = i + 2
while(1)

End

```

Figure 4.12: This is the Igor Pro program that finds the maximum for each artifact data set.

Table0:Xmin,Xmax,Ymin,Ymax					
RO			-1.32995		
Point	Xmin	Xmax	Ymin	Ymax	
0	-1.32995	0.02725	-0.1002	0.3108	
1	-1.2885	0.0595	-0.2157	0.3615	
2	-1.2962	0.043	-0.1727	0.3009	
3	-1.3197	0.0903	-0.2298	0.3686	
4	-1.3798	0.0214	-0.2079	0.3489	
5	-1.45	0.0464	-0.1357	0.5183	
6	-1.4871	0.0577	-0.0734	0.6298	
7	-1.3759	0.0565	-0.0839	0.5405	
8	-1.4005	0.1283	-0.1575	0.6101	
9	-1.3652	0.058	-0.1386	0.5602	
10	-1.3188	0.0792	-0.145	0.4922	
11	-1.2523	0.0297	-0.1053	0.4559	
12	-1.1948	0.072	-0.0995	0.4165	
13	-1.2167	0.0585	-0.079	0.4738	
14	-1.1568	0.0044	-0.0797	0.4555	
15	-1.0507	0.0185	-0.1926	0.3678	
16	-1.0252	0.0624	-0.092	0.3944	
17	-0.9887	0.0477	-0.1134	0.3206	
18	-0.9463	0.0217	-0.1049	0.3823	
19	-0.8772	0.002	-0.0617	0.3539	
20	-0.8468	-0.0064	-0.0951	0.2621	
21	-0.8838	-0.0166	-0.1121	0.3183	
22	-0.7929	0.0219	-0.0635	0.2221	
23	-0.8179	0.0209	-0.0728	0.3288	
24	-0.7966	0.0342	-0.0822	0.379	
25	-0.8487	0.0441	-0.1084	0.294	
26	-0.7488	0.0416	-0.0852	0.2656	
27	-0.7827	0.0145	-0.084	0.35	
28	-0.7464	0.0184	-0.0923	0.2749	
29	-0.7383	0.0313	-0.0858	0.3102	
30	-0.6264	0.0176	-0.0532	0.2328	
31	-0.6283	0.0593	-0.0756	0.2556	
32	-0.5894	0.0142	-0.0539	0.2457	
33	-0.6503	-0.0443	-0.0882	0.239	
34	-0.6062	0.0006	-0.0894	0.2814	
35	-0.5946	0.0258	-0.0658	0.2402	
36	-0.5328	0.028	-0.0742	0.213	
37	-0.5615	0.00290001	-0.0311	0.2617	
38	-0.5157	0.00500000	-0.0100	0.2560	

Figure 4.13: This a partial list of the minima and maxima found from the artifact data.

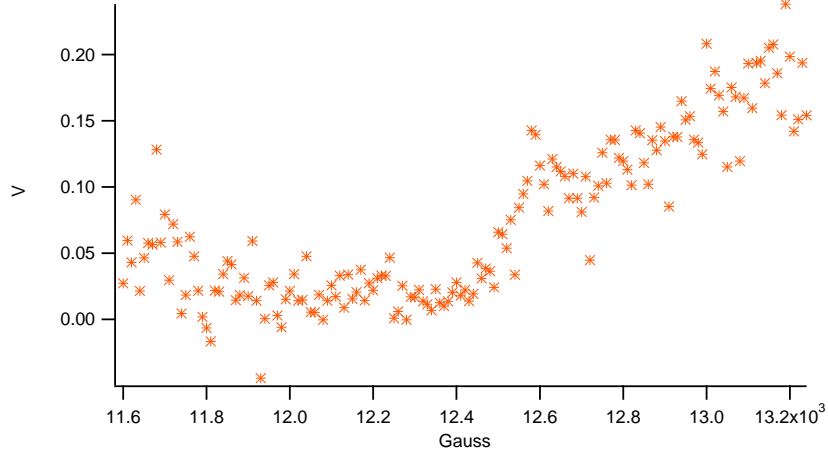


Figure 4.14: This is a plot of the maxima of each artifact vs. the field applied.

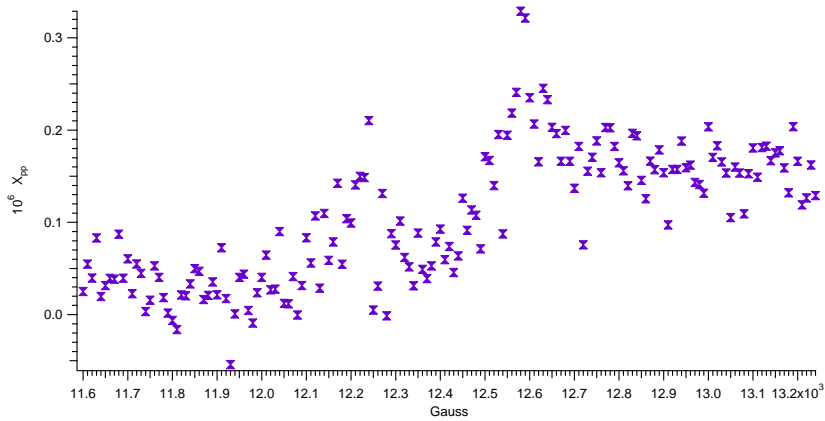


Figure 4.15: This is a plot of the maxima normalized by dividing according to the fringe size. Dividing by the fringe size makes the data directly proportional to the cantilever displacement. There are two peaks.

```
NormXmax
#pragma rtGlobals=1 // Use modern global access method.
Function NormXmax()

Variable i = 24
Variable a
do
Wave/Z/B w = Xmax
Make/N = 1000/0 XmaxNorm
Wave/Z/B y = XmaxNorm
if (!WaveExists(w))
break // no such wave- get out of the loop
endif
for(a=0; a<5; a+=1)
y[a] = w[a] / 1.086
endifor
for(a=5; a<10; a+=1)
y[a] = w[a] / 1.471
endifor
for(a=10; a<15; a+=1)
y[a] = w[a] / 1.31
endifor
for(a=15; a<20; a+=1)
y[a] = w[a] / 1.181
endifor
for(a=20; a<25; a+=1)
y[a] = w[a] / 1.026
endifor
for(a=25; a<30; a+=1)
y[a] = w[a] / .885
endifor
for(a=30; a<35; a+=1)
y[a] = w[a] / .818
endifor
for(a=35; a<40; a+=1)
y[a] = w[a] / .64
endifor
for(a=40; a<45; a+=1)
y[a] = w[a] / .53
endifor
for(a=45; a<50; a+=1)
y[a] = w[a] / .451
endifor
```

Figure 4.16: This is the Igor Pro program that normalizes the maxima of the artifact data set.

Chapter 5

New Room Temperature NMRFM Probe

5.1 La Flaca II

Due to the alignment issues that I had with the probe that I inherited from Utkur, La Flaca, Dr. Markert decided that I should build a new probe. I call it La Flaca II. This probe is modeled after Yong Lee's probe [25]. The main difference between La Flaca and the new probe is that it incorporates two three dimensional slip stick stages. One stage allows for remote alignment of the fiber with the cantilever and the other allows for positioning of the gradient magnet. By changing the position of the gradient magnet one can move the resonant slice through the sample. This will allow for the analysis of relaxation times spatially throughout the sample.

5.2 Tiny Slip-Stick Positioners

The first consideration for the probe was the design of the stages. This was particularly important because this probe is designed to fit inside of the lab's electromagnet. The distance between the pole faces of this electromagnet is only 1.5", so the dimensions of the stages need to be even smaller than this. A schematic of the probe design is shown in Figure 5.1. The design was done

in SOLIDWORKS by an undergraduate, Daniel Curtis. Detailed drawings of each component are found in Appendix D.

All of the stages are made of titanium to ensure that they are strong but not magnetic. The plates onto which the stages mount are made of copper. The rods onto which the copper plates mount with stainless steel set screws are made of copper. The x and y direction components of the stages were of particular importance because there is not much room for movement. Because of this it was necessary to use piezos that are much shorter than any used before in the lab. The titanium pieces were made to fit piezos with dimensions of $2\text{ mm} \times 3\text{ mm} \times 5\text{ mm}$. However the piezos that we purchased were $2\text{ mm} \times 3\text{ mm} \times 5\text{ mm}$ except for they are coated with green insulating resin. In order for them to fit in the titanium pieces, the resin had to be removed. The resin is removed by soaking the piezo in acetone at least over night and then slicing off the resin using a razor blade. Take care not to damage the red and white leads because if they are pulled off the piezo will no longer work. Details on the piezos can be found in Appendix E.

There are then graphite pieces attached to the piezos that allow for the slip stick motion. The graphite pieces need to be cut into very precise rectangular prisms so that they are just a little bit larger than the space allowed in the clamp. The clamp needs to hold on to the graphite and not directly to the other piece of the titanium in order for it to move.

The piezos and the graphite parts need to be attached with care to ensure proper alignment of the stages. H77 black epoxy is used to attach the

graphite bars and piezos together. Specifications for the H77 two part black epoxy can be found in Appendix F.

There also need to be springs in between the head of the clamp screws and the titanium to allow for the proper tension around the graphite. Make sure to make or purchase springs that are not magnetic.

Once all of the graphite pieces have been epoxied and the stages are assembled one must apply a sawtooth signal to the piezo to obtain the motion. I will describe the electronics in detail in a later section.

The main problem to achieve motion in all directions is adjusting the tension in the clamps accurately. I found that the best way to get motion from the piezos was by applying an even amount of tension around the graphite. To achieved this, I would tighten both screws on a given clamp. I would then pull them apart and measure the amount that the clamp would separate on each side. It turned out that if the amount that could be separated on each side was the same then the stage would move. If you tighten one side of a clamp much more than the other, then the stage will not move. Pictures of the probe can be found in Figure 5.2.

5.3 Positioner Electronics

There are two things necessary to get the sawtooth waveform necessary to drive the positioners. The first is a sawtooth waveform that has a very sharp drop after it reaches its maximum. You also need to be able to produce

a sawtooth that is always positive and that can have either a positive or a negative slope. You also need to be able to control the amount of sawtooth waves that are sent to the piezos for accurate stage control. The second thing that is necessary is an amplifier that can amplify the sawtooth waveform to 60 V in order to drive the piezos.

The waveform is generated by LabView and is output from the computer by a DAQ card. The DAQ model number is PXIe-6259 and a pinout diagram is shown in Figure 5.3. The maximum voltage out by the DAQ card is only 10 volts, so the sawtooth signal must be amplified in order to drive the piezos.

OPA 549 operational amplifiers were used to amplify the voltage from approximately 2 volts out from the DAQ card to having a variable amplitude of up to 60 V. These amplifiers are only rated up to 60 volts as shown in Figure 5.4. There is an amplifier for each axis of motion of the stages. In total there are six. Three for the stages that move the fiber and three for the stages that move the magnet. The circuit diagram for the OPA 549 is given in Figure 5.5. Wiring the amplifier circuitry proved to be a bit challenging because the pin separation on this op amp was not the standard 0.1". Instead the separation between pins is 0.067" and so the amplifiers can not be mounted directly onto a breadboard. As a way to work around this problem I etched a board that functions as a reducer from 0.1" to 0.067". To do this, I had to first make a mask to use when developing a copper board that is covered in photoresist. The details of the mask that I made is shown in Figure 5.6. The board is

shown in Figure 5.7. While exposing the board to light, the mask should be clamped to the board tightly so that light does not filter in between the board and the mask. The end result is shown in Figure 5.8.

Currently, this probe has one fully functioning 3-D stage. This is currently being used to align the fiber to the cantilever. This is shown in Figure 5.9. Also, some characterization has been done in the z - direction. This is shown in Figure 5.10, where the data depict the change in intensity as the stage moves through several interference fringes. This data was collected by measuring the voltage from the laser interferometer and the voltage applied to the z piezo simultaneously with two voltmeters (Keithley 2700 and HP 3455A) that have a GPIB (IEEE-488) interface with a LabView program.

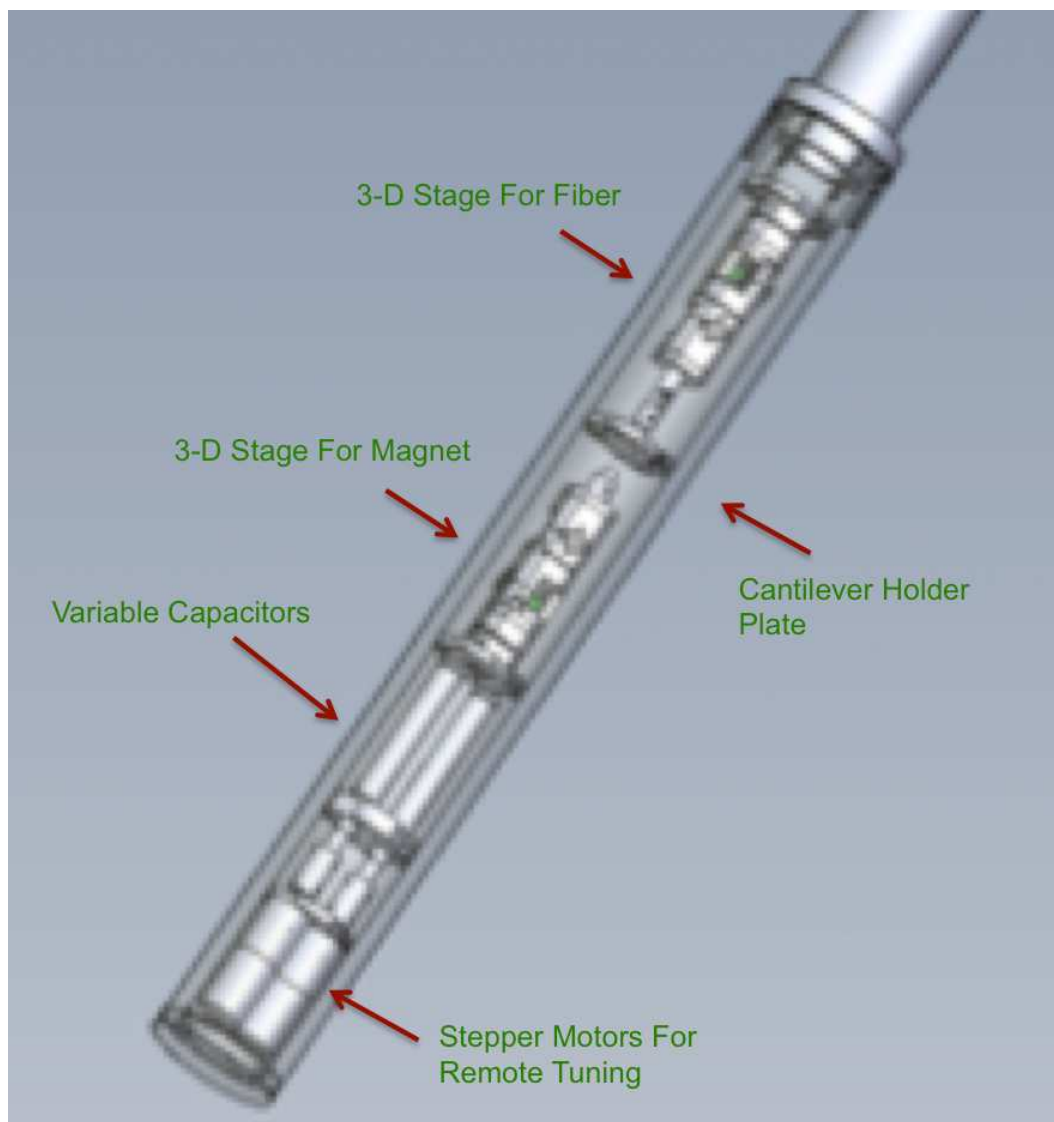


Figure 5.1: In this schematic one can see a complete overview of the new probe.

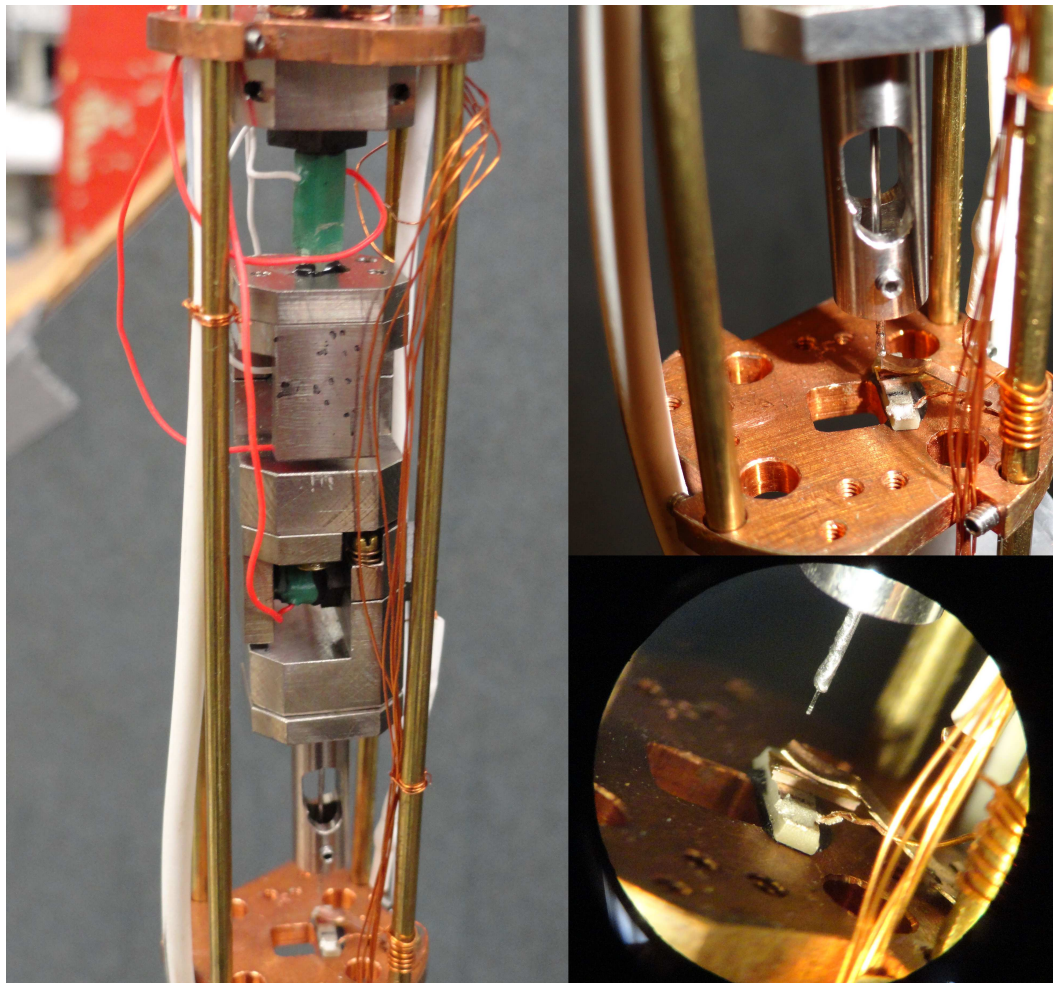


Figure 5.2: These are pictures of the assembled probe.

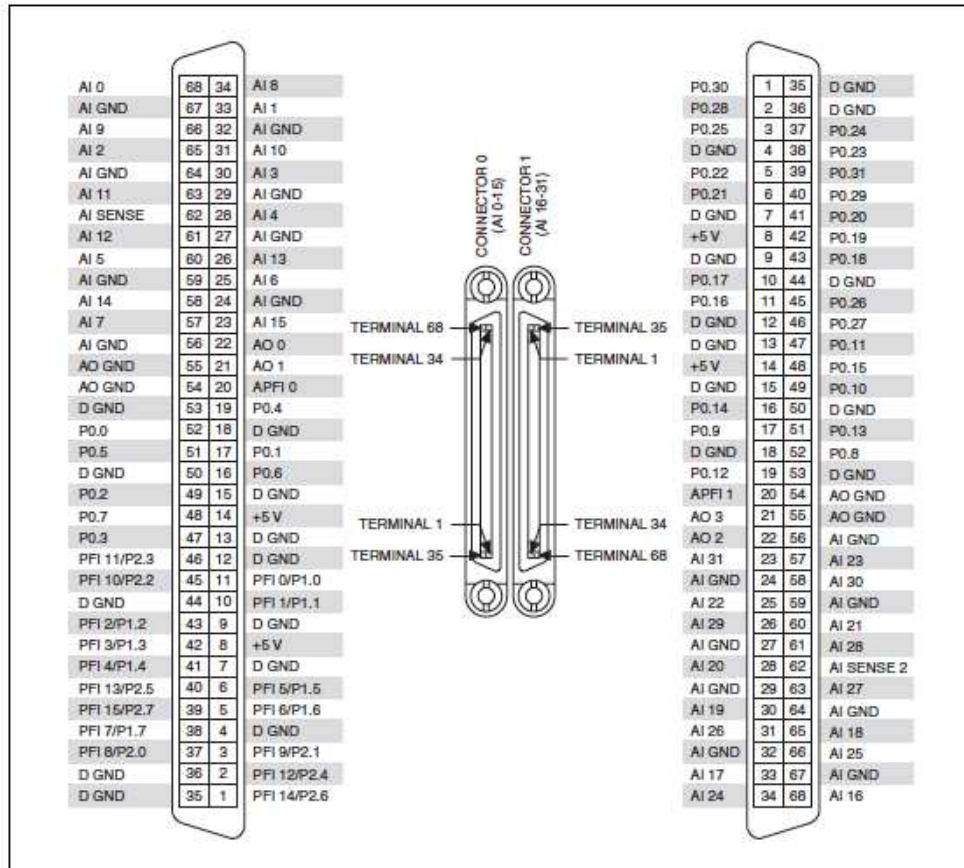


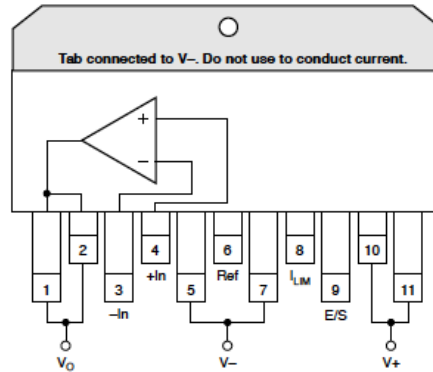
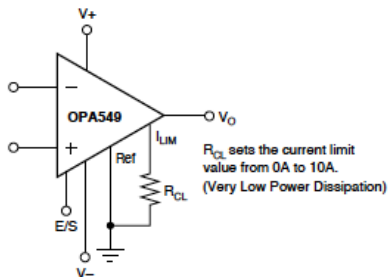
Figure A-44. NI PCI/PCIe/PXI/PXIe-6259 Pinout

Figure 5.3: This is a pinout of the PXIe-6259 DAQ card used.



SBOS093C – MARCH 1999 – REVISED SEPTEMBER 2002

High-Voltage, High-Current OPERATIONAL AMPLIFIER



ABSOLUTE MAXIMUM RATINGS⁽¹⁾

Output Current	See SOA Curve (Figure 8)
Supply Voltage, V+ to V-	60V
Input Voltage Range	(V-) - 0.5V to (V+) + 0.5V
Input Shutdown Voltage	Ref - 0.5 to V+
Operating Temperature	-40°C to +125°C
Storage Temperature	-55°C to +125°C
Junction Temperature	150°C
Lead Temperature (soldering, 10s)	300°C
ESD Capability (Human Body Model)	2000V

NOTE: (1) Stresses above these ratings may cause permanent damage.

Connect both pins 1 and 2 to output.
Connect both pins 5 and 7 to V-.
Connect both pins 10 and 11 to V+.

Figure 5.4: These are the OPA 549 specifications.

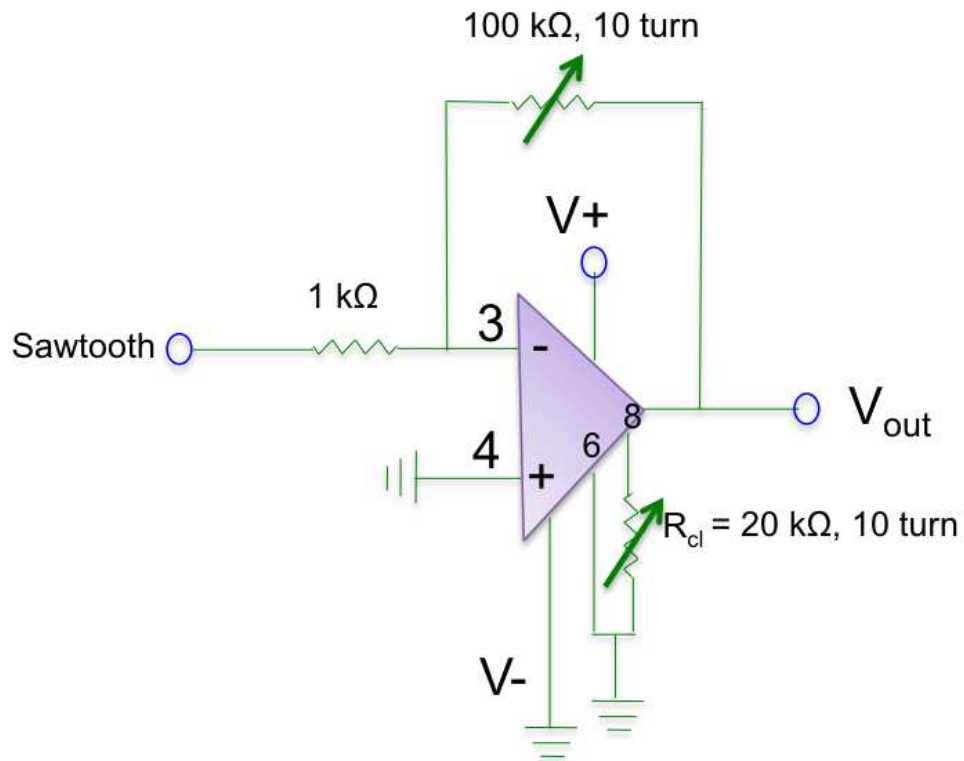


Figure 5.5: This depicts the OPA 549 circuit diagram. Note that the V + is 60 V DC and the V - is grounded. This allows for the signal out to always be positive.

Cárdenas:OPA549,.067" to .1"

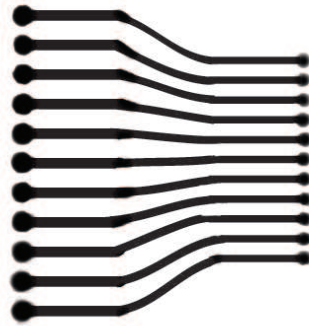


Figure 5.6: This depicts the mask that I used when etching the 0.1” to 0.067” reducer board. Pins were soldered directly to the board on both ends. The pins on the 0.1” end of the etched board were then mounted directly to a breadboard and wired accordingly.

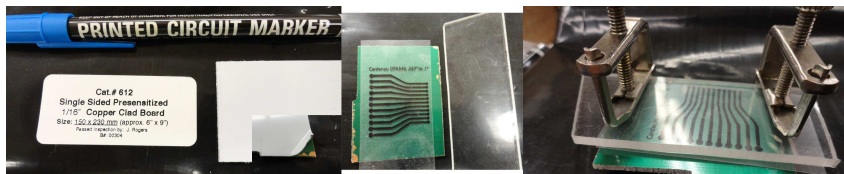


Figure 5.7: Depicted on the left is the board part number, an example of the board that is coated with white plastic to prevent the exposure of the underlying photoresist and a photoresist pen used for filling in any areas where the photoresist was scratched. In the center there is the photoresist coated board with a mask on top and a piece of plexiglass by its side. The plexiglass clamped tightly over the mask is shown on the right.

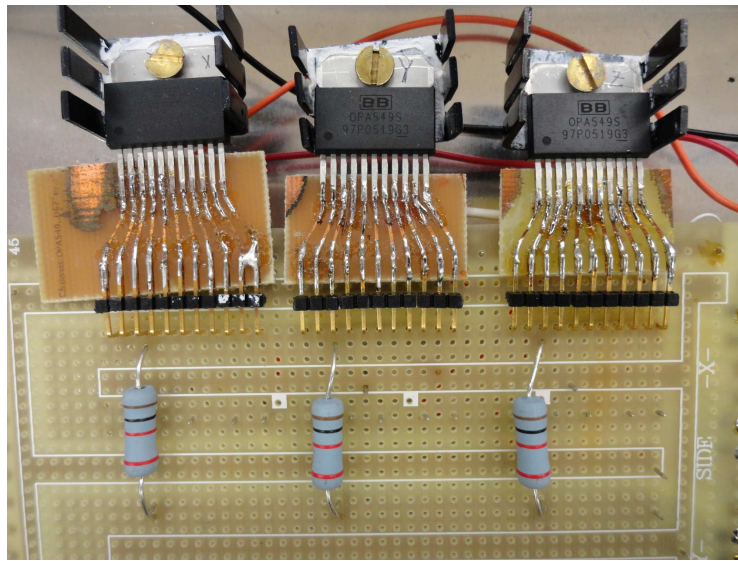


Figure 5.8: This picture shows the resulting etched OPA 549 boards in use.

Figure 5.9: These are frames from a movie of the fiber moving.

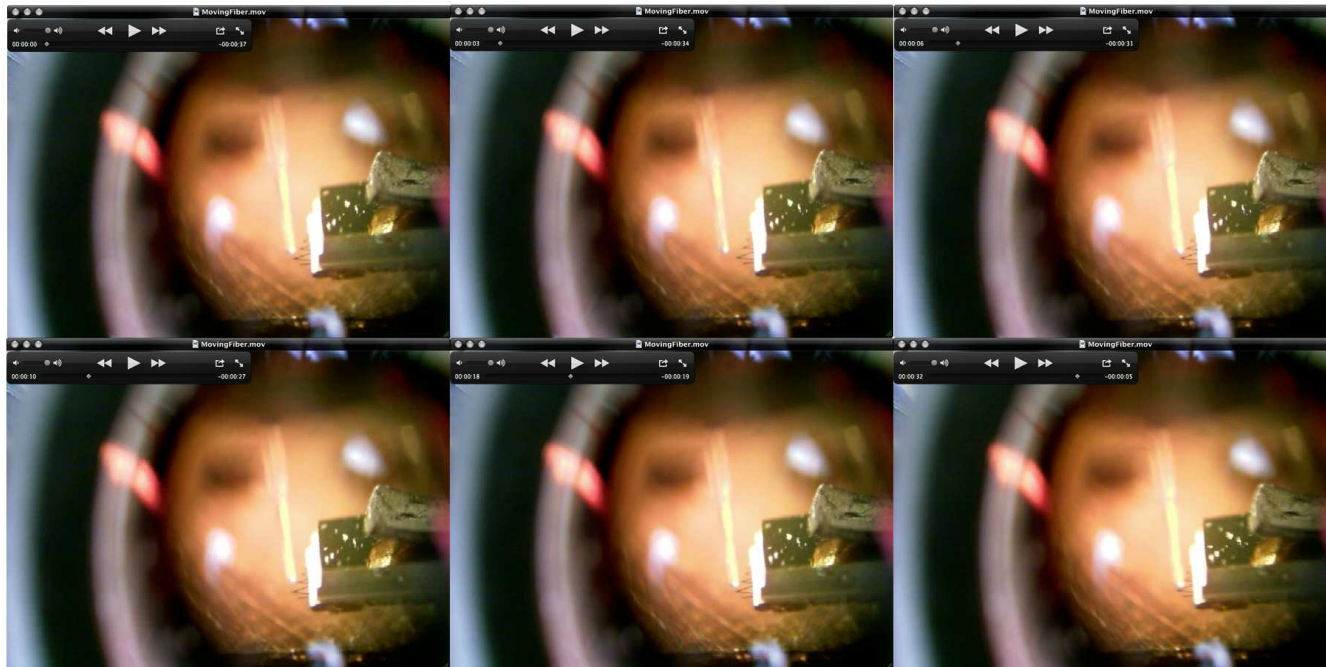
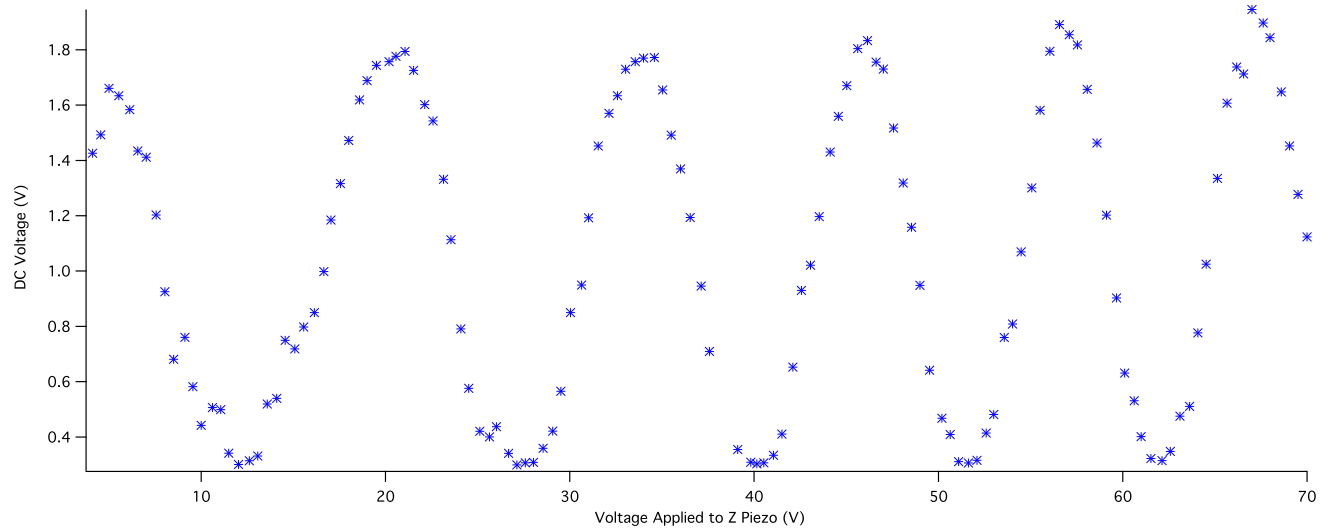


Figure 5.10: As we apply DC voltage to the piezo, it expands and changes the distance between the fiber and the cantilever. The constructive and destructive interference of the laser light is recorded by the DC offset voltage.



Chapter 6

Micro Magnet Coated Cantilevers

6.1 Permalloy Deposition and Masking

Using the electron beam evaporation chamber in the lab, we were able to evaporate permalloy onto a very small area of several mechanical cantilevers. The masking technique used is shown in Figure 6.1. The premise is pretty straight forward, but in practice it is not trivial since cantilevers are quite delicate and can easily be broken when trying to apply the mask and when trying to remove it.

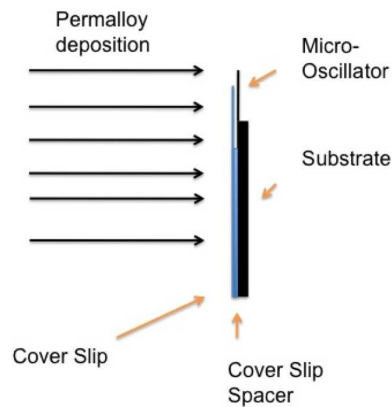


Figure 6.1: In this schematic one can see how the cantilevers were masked so that only a very small area is exposed during the permalloy evaporation process.

6.2 Results

We were successful in depositing magnetic material over a small area of the cantilever by using this masking technique. Figure 6.2 shows an optical image and a scanning electron microscopy (SEM) image of a coated cantilever.

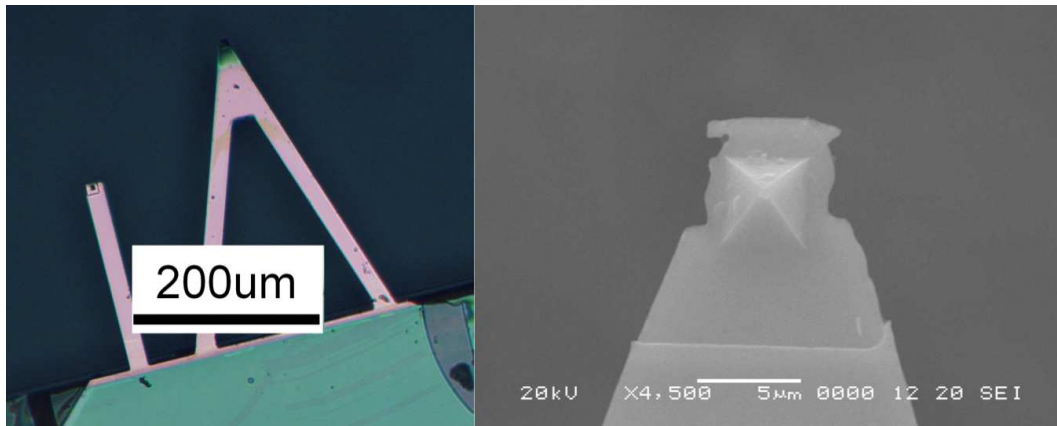
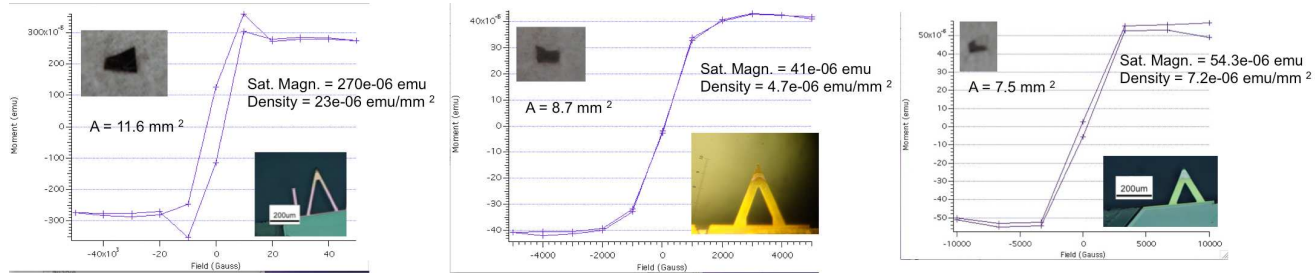


Figure 6.2: Here we see an optical image of a permalloy coated cantilever on the left. On the right is an SEM image of the same cantilever. It is clear from the SEM image that there is a very discrete line where the deposition begins.

During any given evaporation, the amount of material deposited was monitored by a deposition monitor. We also made sure to include a piece of glass as a reference sample. With this reference we could also measure the thickness by using atomic force microscopy (AFM). The thickness measured was in good agreement with that of the deposition monitor. We were also able to analyze this reference with a SQUID magnetometer and determine the saturation magnetization. SQUID analysis is shown in Figure 6.3. From the

saturation magnetization and the area of the sample we can calculate the a magnetization density for the sample. Once this is known, we can then divide it by the known saturation magnetization volume density of permalloy, 800 kA/m, to check if the thickness calculated agrees with the thickness measured.

Figure 6.3: This is the SQUID data from the reference samples that were coated with permalloy alongside the cantilevers. From this data one can calculate the net moment per area of a given sample.



Chapter 7

Summary and Future Work

7.1 Summary

In summary, this dissertation expresses that the main motivation for a microscopy form of nuclear magnetic resonance is that there is a limitation on the resolution in conventional nuclear magnetic resonance that arises directly from the experiment. In order to surpass these physical limitations one must consider an alternative way of conducting NMR experiments. NMRFM offers the capacity to achieve much higher resolution than conventional NMR and should be further developed.

In Chapter 2, some basic theory behind conventional NMR was described and the relaxation times that may be found experimentally along with their physical meaning were discussed. A basic NMR experimental set-up was also described in detail.

In Chapter 3, the foundation of NMRFM was explained and each part of the experiment was discussed in great detail. Chapter 4 described an existing probe and the experimental procedures necessary to conduct an NMRFM experiment.

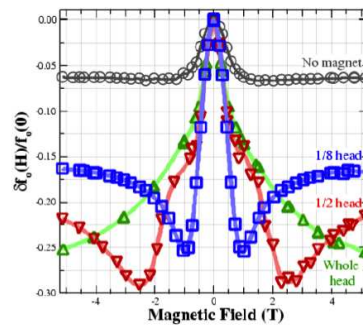
Chapter 5 discussed the new room-temperature NMRFM probe and

how it has been put together. Finally, Chapter 6 showed how we have been able to deposit magnetic material over a small area of a mechanical cantilever. These cantilevers will be used to conduct NMRFM in the magnet on oscillator geometry.

7.2 Future Work

7.2.1 Analysis of Micro Magnet Coated Cantilevers

The first thing to analyze with the new probe are the permalloy coated cantilevers. It has been shown that the resonant frequency of mechanical cantilevers that are coated with a magnetic material will shift as an external magnetic field is applied [22]. The data is shown in Figure 7.1.



Normalized shift in resonant frequency for a bare paddle \circ and magnetically capped oscillators A, \square , B, ∇ , and C, \triangle .

Figure 7.1: These plots show the shift in resonant frequency of magnetically coated cantilevers vs. the applied field [22].

7.2.2 NMRFM Liquid Sample

Once the cantilevers have been characterized, then they can be used to conduct an NMRFM experiment in the magnet-on-oscillator geometry. Since the magnet is located directly on the cantilever, the sample can be mounted to the second positioning stage. This would be a great opportunity to use a sample that could not be studied in the sample-on-cantilever geometry. A good choice for a sample would be water since it has not yet been analyzed using NMRFM. One challenge for doing this type of experiment on a liquid is the method for containing the liquid. I propose that a silicon nitride membrane window device be used to hold the liquid. Some examples of these silicon nitride windows are shown in Figure 7.2. These are relatively inexpensive and readily available from companies like NORCADA, <http://www.norcada.com/products.php>.

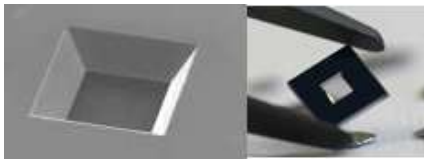


Figure 7.2: These are some images of silicon nitride membrane window devices [23] and [24]. I propose that these be used for holding liquid samples in an NMRFM experiment.

A schematic of the proposed experiment is shown in Figure 7.3. There are some differences in this experimental set-up from the NMRFM experiments typically done in our lab. The first is the use of a liquid sample. The second and I think more complicated part is the use of a wire to produce the radio frequency field, B_1 perpendicular to B_0 . However, if it is more convenient, one

could continue to use a coil around the fiber as the method of producing B_1 . A first goal would be to characterize otherwise-identical micro liquid samples by their different NMR relaxation times, that is, to perform dynamical NMR imaging using NMRFM.

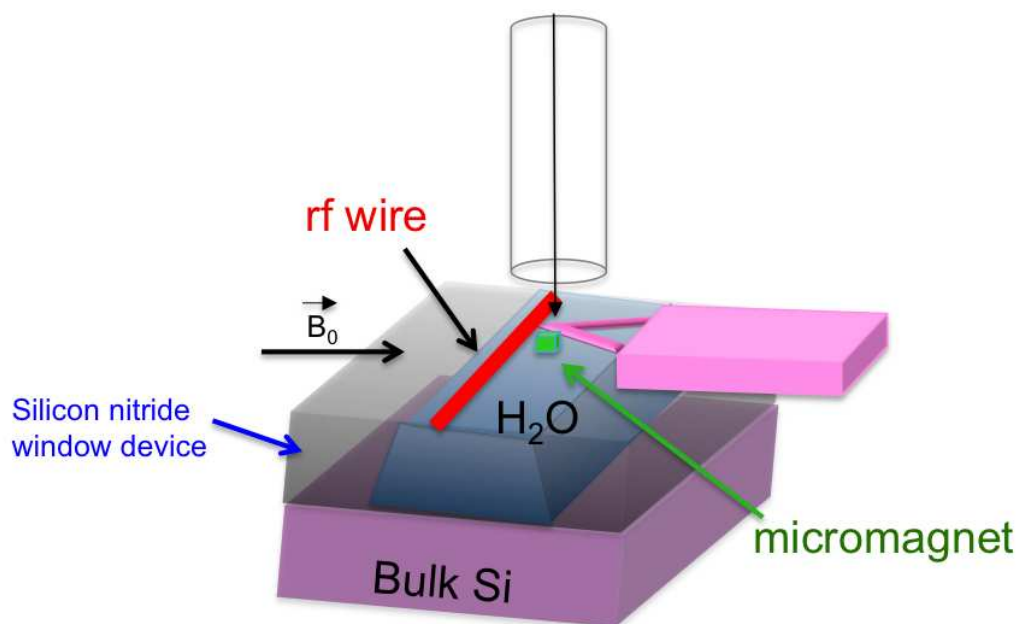


Figure 7.3: This schematic describes how an NMRFM experiment could be conducted on a liquid sample.

Appendices


Appendix A
NMR Periodic Table

										Inert Gases													
										2	He												
										3	32.436 -1/2												
										5	B	6	C	7	N	8	O	9	F	10	Ne		
										10	4.575 3 0.00385965	13	10.708	14	3.077 1 0.00099825	17	5.347	19	40.062	21	3.361		
										11	13.656 3/2 0.1322807	1/2	0.00017544	15	4.316 -1/2 3.8421E-06	-5/2	1.0719E-05	1/2	0.829824561	-3/2	6.29825E-06		
										13	Al	14	Si	15	P	16	S	17	Cl	18	Ar		
										27	11.095 5/2 0.20526316	29	8.459 -1/2 0.00036667	31	17.237 1/2 0.06614035	33	3.268 3/2 1.707E-05	35	4.172 3/2 0.00354386	37	3.473 3/2		
28	Ni	29	Cu	30	Zn	31	Ga	32	Ge	33	As	34	Se	35	Br	36	Kr						
	61 3.805 -3/2 4.21053E-05	63 11.296 3/2 0.064035088 65 12.100 3/2 0.035263158	67 2.664 5/2 0.000116667	69 10.220 3/2 0.04157895 71 12.985 3/2 0.05596491	73 1.485 -9/2 0.00010825	75 7.291 3/2 0.02508772	77 8.121 1/2 0.00052281	79 10.668 3/2 0.039649123 81 11.500 3/2 0.048596491	83 1.638 -9/2 0.000215789														
46	Pd	47	Ag	48	Cd	49	In	50	Sn	51	Sb	52	Te	53	I	54	Xe						
	105 1.949 -5/2 0.000247368	107 1.724 -1/2 3.42105E-05 109 1.981 -1/2 4.84211E-05	111 9.027 -1/2 0.001215789 113 9.443 -1/2 0.001333333	113 9.310 9/2 0.01470175 115 9.330 9/2 0.33157895	117 15.172 -1/2 0.00342807 119 15.878 -1/2 0.00442105	121 10.190 5/2 0.09122807 123 5.518 7/2 0.01947368	123 13.434 -1/2 0.00015614 125 11.143 -1/2 0.00219298	127 8.520 5/2 0.092982456	129 11.777 -1/2 0.005578947 131 3.491 3/2 0.000580702														
78	Pt	79	Au	80	Hg	81	Tl	82	Pb	83	Bi	84	Po	85	At	86	Rn						
	195 9.154 1/2 0.003350877	197 0.729 3/2 1.05263E-05	199 7.626 1/2 0.000950877 201 2.810 -3/2 0.000189474	203 24.366 1/2 0.05070175 205 24.605 1/2 0.13491228	207 8.881 1/2 0.00207018	209 6.842 9/2 0.13631579																	
64	Gd	65	Tb	66	Dy	67	Ho	68	Er	69	Tm	70	Yb	71	Lu								
	155 1.626 -3/2 3.50877E-05 157 2.033 -3/2 8.42105E-05	159 9.657 3/2 0.057894737	161 1.403 -5/2 7.89474E-05 163 1.952 5/2 0.000280702	165 8.734 7/2 0.1754386	167 1.231 -7/2 0.00011579	169 3.522 -1/2 0.0005614	171 7.500 1/2 0.00071053 173 2.066 -5/2 0.0002	175 4.857 7/2 0.027368421 176 3.376 7 0.000901754															
96	Cm	97	Bk	98	Cf	99	Es	100	Fm	101	Md	102	No	103	Lw								

Figure A.2

Appendix B

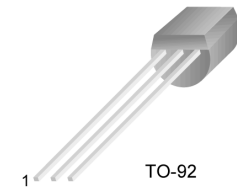
RF Board Parts



2N3820

P-Channel General Purpose Amplifier

- This device is designed primarily for low level audio and general purpose applications with high impedance signal sources.
- Sourced from process 89.



TO-92
1. Drain 2. Gate 3. Source

Epitaxial Silicon Transistor

Absolute Maximum Ratings* $T_C=25^{\circ}\text{C}$ unless otherwise noted

Symbol	Parameter	Ratings	Units
V_{DG}	Drain-Gate Voltage	-20	V
V_{GS}	Gate-Source Voltage	20	V
I_{GF}	Forward Gate Current	10	mA
T_{STG}	Storage Temperature Range	-55 ~ 150	$^{\circ}\text{C}$

* This ratings are limiting values above which the serviceability of any semiconductor device may be impaired.

Figure B.1

2N3906

Preferred Device

General Purpose Transistors

PNP Silicon

Features

- Pb-Free Packages are Available*

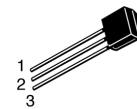
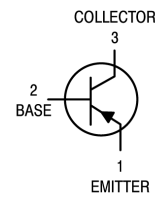
MAXIMUM RATINGS

Rating	Symbol	Value	Unit
Collector - Emitter Voltage	V_{CEO}	40	Vdc
Collector - Base Voltage	V_{CBO}	40	Vdc
Emitter - Base Voltage	V_{EBO}	5.0	Vdc
Collector Current - Continuous	I_C	200	mAdc
Total Device Dissipation @ $T_A = 25^\circ\text{C}$ Derate above 25°C	P_D	625 5.0	mW mW/ $^\circ\text{C}$
Total Power Dissipation @ $T_A = 60^\circ\text{C}$	P_D	250	mW
Total Device Dissipation @ $T_C = 25^\circ\text{C}$ Derate above 25°C	P_D	1.5 12	Watts mW/ $^\circ\text{C}$
Operating and Storage Junction Temperature Range	T_J, T_{stg}	-55 to +150	$^\circ\text{C}$



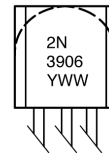
ON Semiconductor®

<http://onsemi.com>



TO-92
CASE 29
STYLE 1

MARKING DIAGRAMS

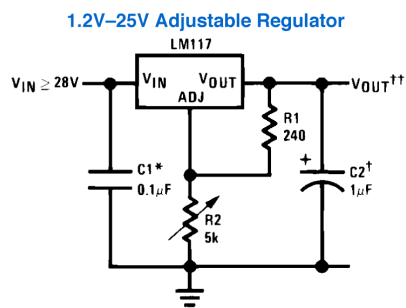


Y = Year
WW = Work Week

Figure B.2

3-Terminal Adjustable Regulator

Typical Applications



906301

Full output current not available at high input-output voltages

*Needed if device is more than 6 inches from filter capacitors.

†Optional—improves transient response. Output capacitors in the range of 1μF to 1000μF of aluminum or tantalum electrolytic are commonly used to provide improved output impedance and rejection of transients.

$$\dagger\dagger V_{OUT} = 1.25V \left(1 + \frac{R2}{R1} \right) + I_{ADJ}(R2)$$

TO-220 (T)
Plastic Package

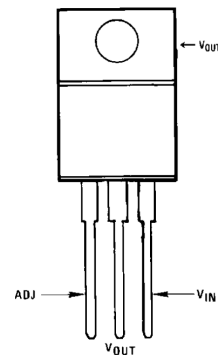


Figure B.3



NTE957 Integrated Circuit 3-Terminal Adjustable Negative Voltage Regulator

Features:

- Output Voltage Adjustable from $-1.2V$ to $-37V$
- Guaranteed 1.5A Output Current
- Line Regulation Typically 0.01%/V
- Load Regulation Typically 0.3%
- Excellent Thermal Regulation: 0.002%/W
- 77dB Ripple Rejection
- Temperature-Independent Current Limit
- Internal Thermal Overload Protection
- 100% Electrical Burn-In
- Eliminates the Need to Stock Many Voltages

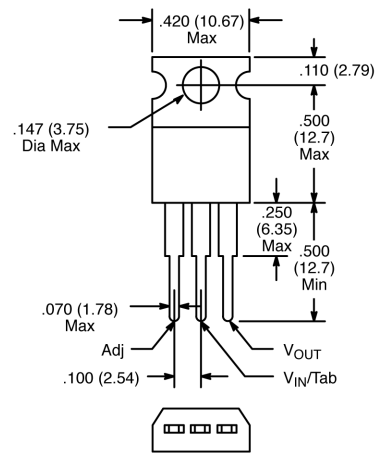


Figure B.4

Coaxial High Isolation Switch

50Ω SPST, Absorptive DC to 2000 MHz

ZFSWHA-1-20+



CASE STYLE: J17

Connectors	Model	Price	Qty.
SMA	ZFSWHA-1-20+	\$74.95	(1-9)
BRACKET (OPTION "B")		\$2.50	(1+)

+ RoHS compliant in accordance with EU Directive (2002/95/EC)

The + Suffix has been added in order to identify RoHS Compliance. See our web site for RoHS Compliance methodologies and qualifications.

Maximum Ratings

Operating Temperature	-55°C to 100°C
Storage Temperature	-55°C to 150°C
Input Power	see Table & Note 1
Control Current	see Table

Permanent damage may occur if any of these limits are exceeded.

Coaxial Connections

RF IN	2
RF OUT	3
CONTROL 1	1
CONTROL 2	S

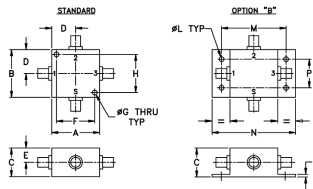
Features

- wideband, DC to 2000 MHz
- low insertion loss, 1.3 dB typ.
- low video leakage 30 mVp-p typ.
- very fast switching

Applications

- PCN
- cellular
- antenna switching

Outline Drawing



Outline Dimensions (inch/mm)

A	B	C	D	E	F	G	H
1.25	1.25	.75	.63	.38	1.000	.125	1.000
31.75	31.75	19.05	16.00	9.65	25.40	3.18	25.40
J	K	L	M	N	P	Q	wt
--	--	.125	1.688	2.18	.75	.07	grams
--	--	3.18	42.88	55.37	19.05	1.78	75.0

High Isolation Switch Electrical Specifications

FREQ. (MHz)	INSERTION LOSS (dB)						1dB COMPR. (dBm)			IN-OUT ISOLATION (dB)								
	DC-100 MHz		100-1000 MHz		1000-2000 MHz		DC-100 MHz		100-1000 MHz		1000-2000 MHz		DC-100 MHz		100-1000 MHz		1000-2000 MHz	
f _c	f _p	Typ.	Max.	Typ.	Max.	Typ.	Max.	Typ.	Typ.	Typ.	Typ.	Typ.	Typ.	Min.	Typ.	Min.	Typ.	Min.
DC	2000	0.8	1.2	1.3	1.7	1.3	1.7	19	19	26	75	60	65	58	65	58	65	58

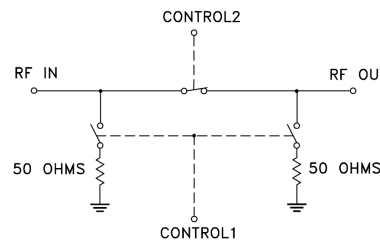
Additional Specifications

Control Voltage, volts	-0.2 to 0			
Low State	-0.2 to 0			
High State (negative) for compression specs for other specs	-8			
Control Current, mA	0.5 Max. at -9V to -12V Typ.			
RF Power Input Max. ¹	DC-.02	.02-5	5-2	GHz
Steady State 0/-8V As Modulator ²	+23	+30	+33	dBm
	+14.5	+20	+27	dBm
Video Leakage ³ , mVp-p	30 Typ., 50 Max.			
VSWR (1)	DC-0.2 GHz		0.2-2 GHz	
ON, all ports	1.25 Max.		1.5 Max.	
OFF, Input	1.25 Max.		1.5 Max.	
OFF, Output	1.4 Max.		1.5 Max.	
Rise/Fall Time (10%-90%), ns	3 Typ., 5 Max.			
Switching Time, 50% of control to 90% RF (Turn-on), ns	7 Typ., 10 Max.			
10% RF (Turn-off), ns	3 Typ., 10 Max.			

CONTROL LOGIC

Control Ports	RF outputs
1	2
-V	0
0	-V
	On
	Off

Electrical Schematic



Mini-Circuits
ISO 9001 ISO 14001 AS 9100 CERTIFIED

For detailed performance specs & shipping online see web site

P.O. Box 350166, Brooklyn, New York 11235-0003 (718) 934-4500 Fax (718) 332-4861 The Design Engineers Search Engine Provides ACTUAL Data Instantly at minicircuits.com

MICROWAVE COMPONENTS
Notes: 1. Performance and quality attributes and conditions not expressly stated in this specification sheet are intended to be excluded and do not form a part of this specification sheet. 2. Electrical specifications and performance data contained herein are based on Mini-Circuit's applicable established test performance criteria and measurement instructions. 3. The parts covered by this specification sheet are subject to Mini-Circuit's standard limited warranty and terms and conditions (collectively, "Standard Terms"). Purchasers of this part are entitled to the rights and benefits contained therein. For a full statement of the Standard Terms and the exclusive rights and remedies thereunder, please visit Mini-Circuit's website at www.minicircuits.com/MCStore/terms.jsp.

REV. B
M121747
ZFSWHA-1-20+
WPCP/AM
090818
Page 1 of 2

Figure B.5: Mini-Circuits ZFSWHA-1-2C RF Gate Data Sheet

Appendix C

Powering On The Big Red Electromagnet

C.1 Powering On Procedure

To power on the electromagnet one must first turn on the magnet's cooling system which is a pump that runs water through the wire plates. This switch is located on the bottom left of the top panel. Then you need to make sure that water is flowing by checking that water is running out of the hose of the magnet and into the drain. Once you are sure that water is flowing, then you can turn the magnet on. To do so, you press the black button on the front panel. You should hear a big clank that indicates that it is powered on.

There is a Gauss meter built into the magnet and that should be turned on next. There are two switches behind the big plates. One is labeled heater and the other is labeled Gauss meter. Both switches should be turned on.

On the panel below the one with the black ON button, which is labeled electromagnet controller, there is a white on/off switch. This should now be turned on.

To set the magnetic field you can use the black thumbwheels. These are in Gauss. You should ramp the field slowly, being careful that the current meter in this controller does not overload.

This magnet is quite old and its cooling system is not great. Make sure to continuously touch the red plates checking for their temperature. If they get hot, one should turn the thumbwheels to 0 Gauss, but leave the water flowing to help cool the plates off.

C.2 Powering Off Procedure

When you are ready to turn off the magnet, first set the thumbwheels back to 0 Gauss. Wait for the current meter to be at zero before turning off the white switch on the electromagnet controller panel. Once the current meter is at zero you can turn off the white switch and the Gauss meter switches in the back. Then you can press the red off button on the top panel. If the plates are still hot do not turn off the water pump. The water pump switch should be the last thing to be turned off.

C.3 Post Power Surge Measures

In the case that turning on the magnet causes a power surge to the lab, make everyone in the lab aware so that they may vent any pumps that have been suddenly shut off. Also, be prepared to flip the breakers in the utility corridor back on. To do so you must turn all of the breakers to the off position first and then to the on position.

Appendix D

Slip-Stick Stage Machine Drawings

Figure D.1: Flange

102

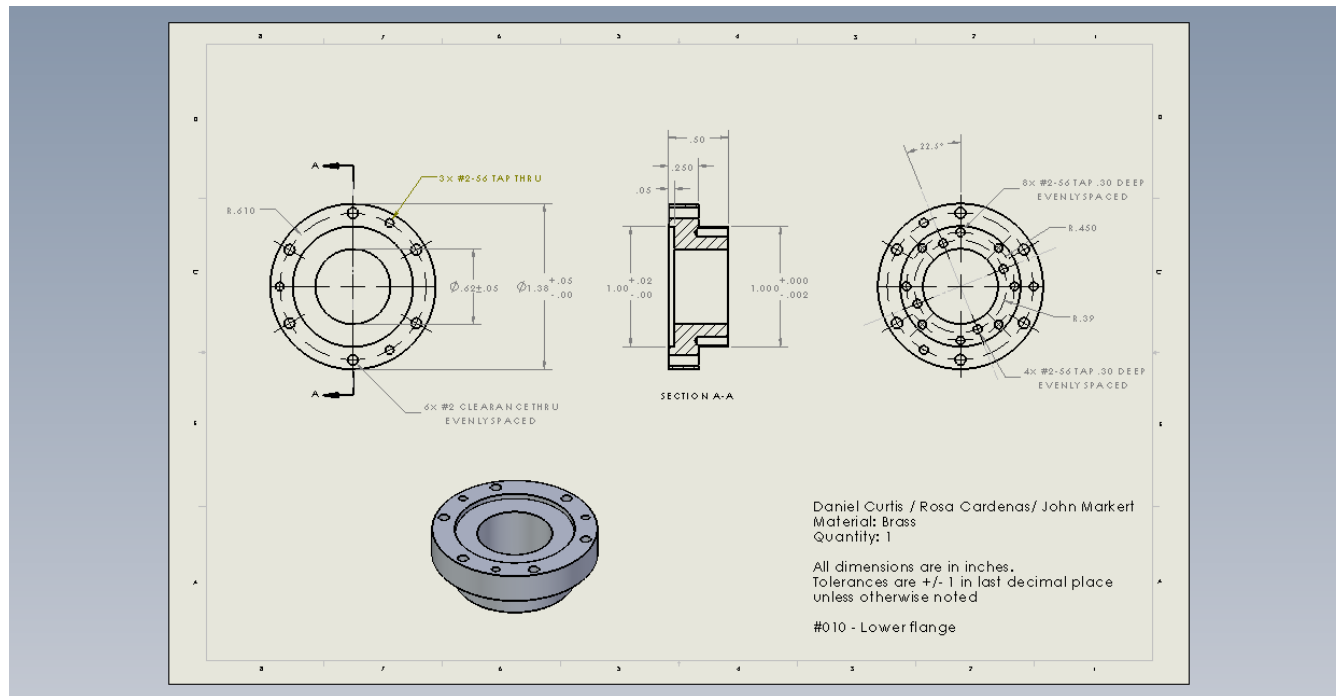


Figure D.2: Can

103

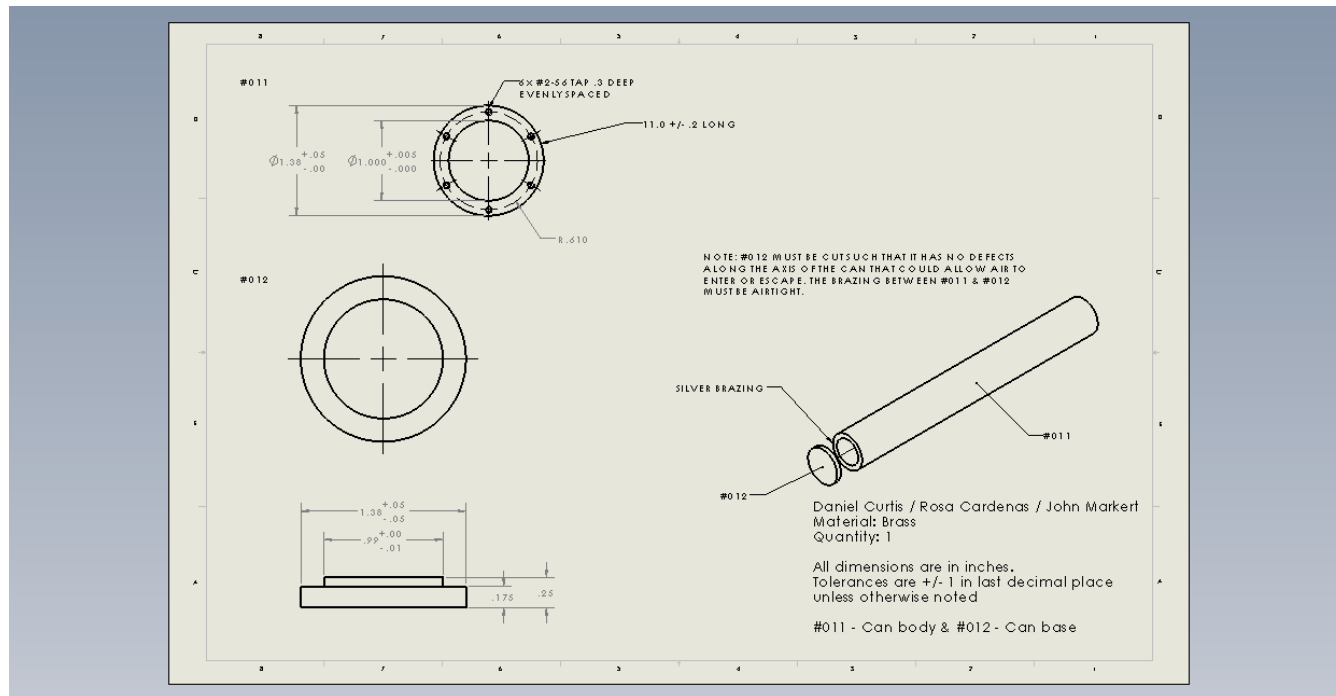


Figure D.3: Plate onto which the stages mount.

104

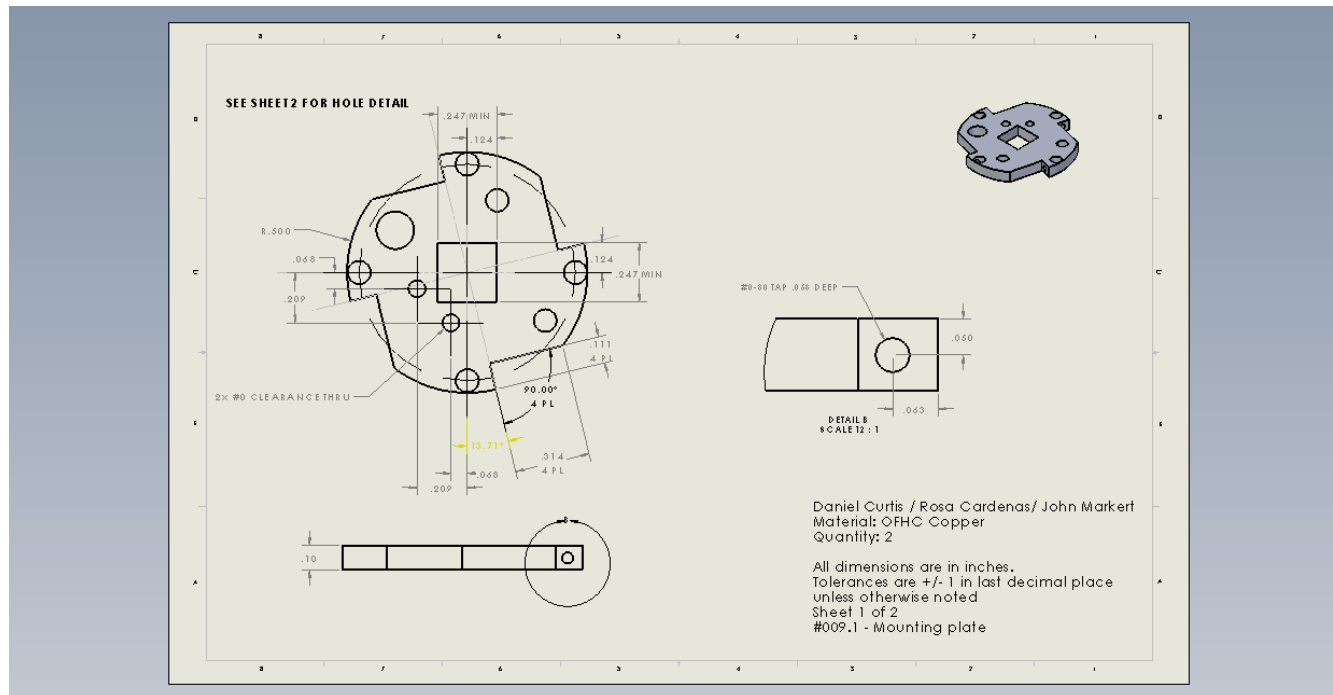


Figure D.4: Stage plate hole details.

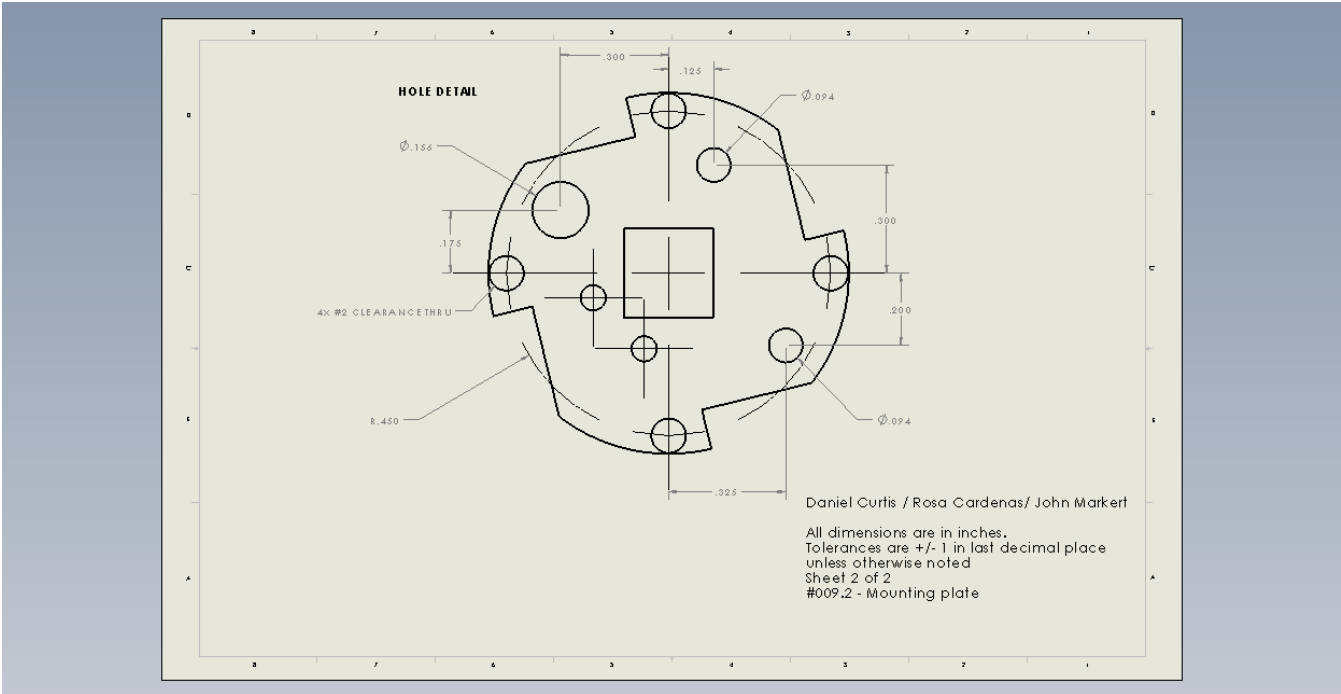


Figure D.5: Base of the z-clamp.

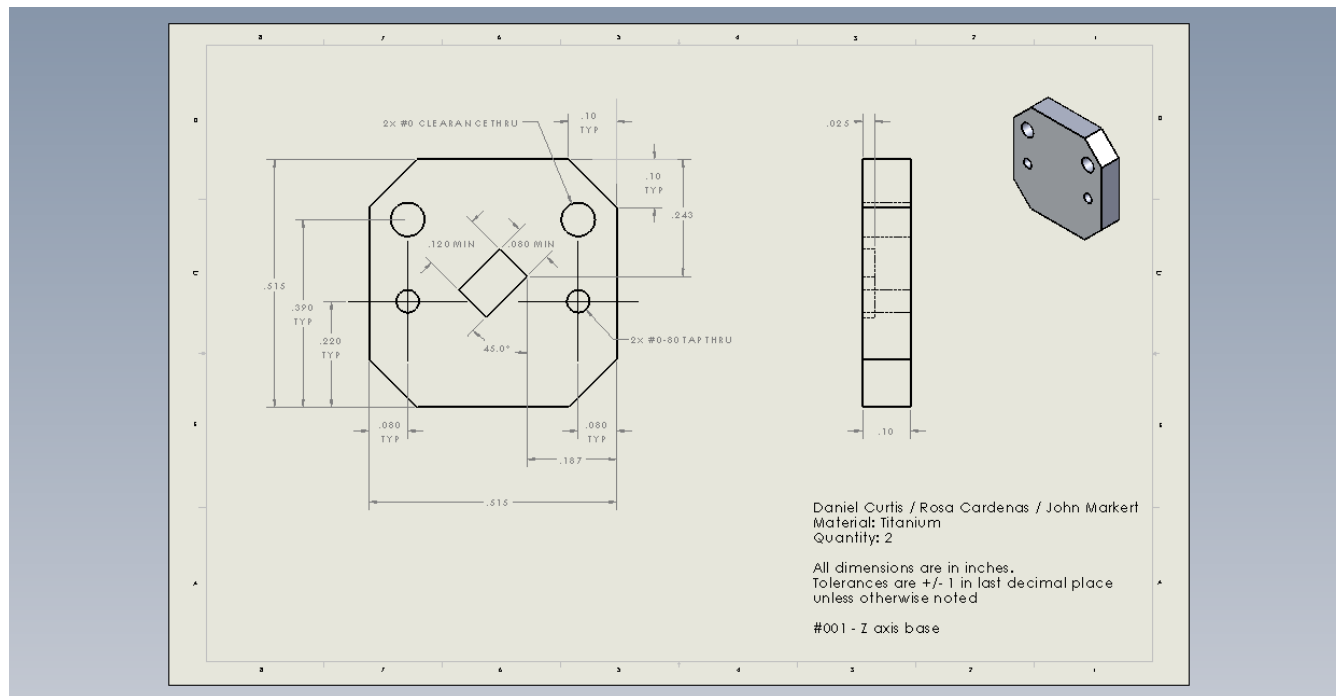


Figure D.6: Part 1 of the z-clamp.

107

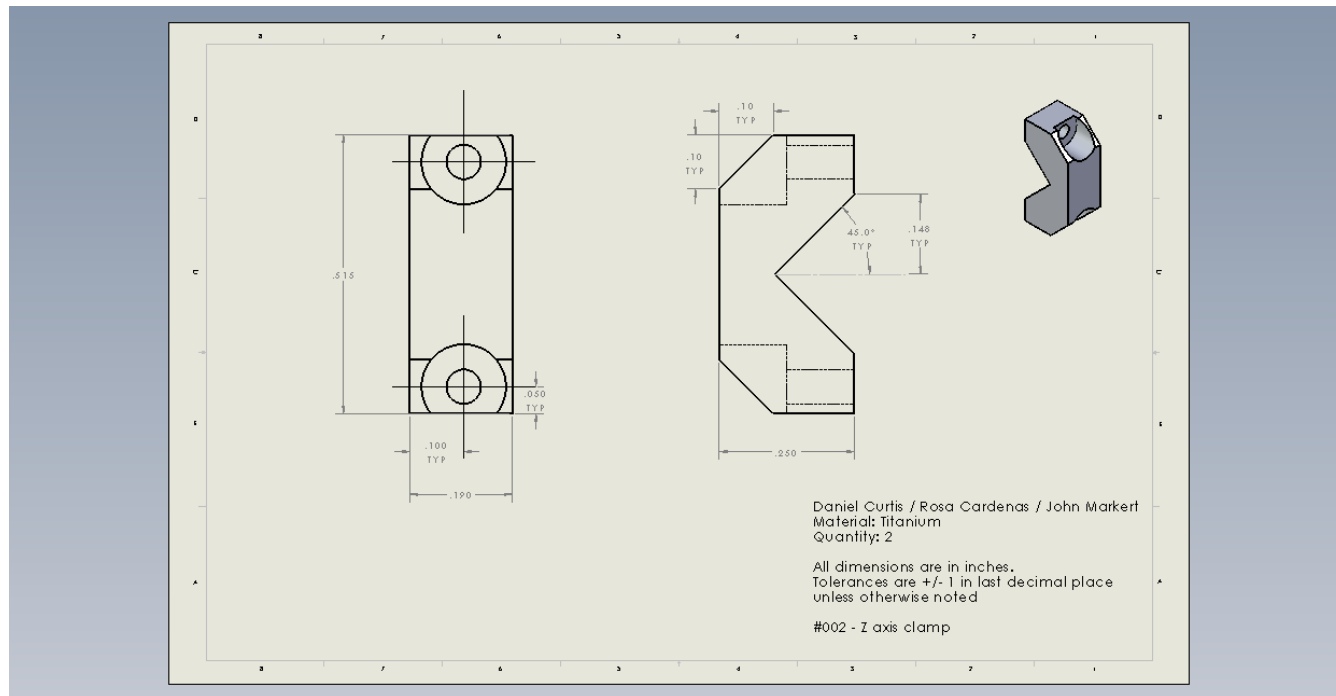


Figure D.7: Part 2 of the z-clamp.

108

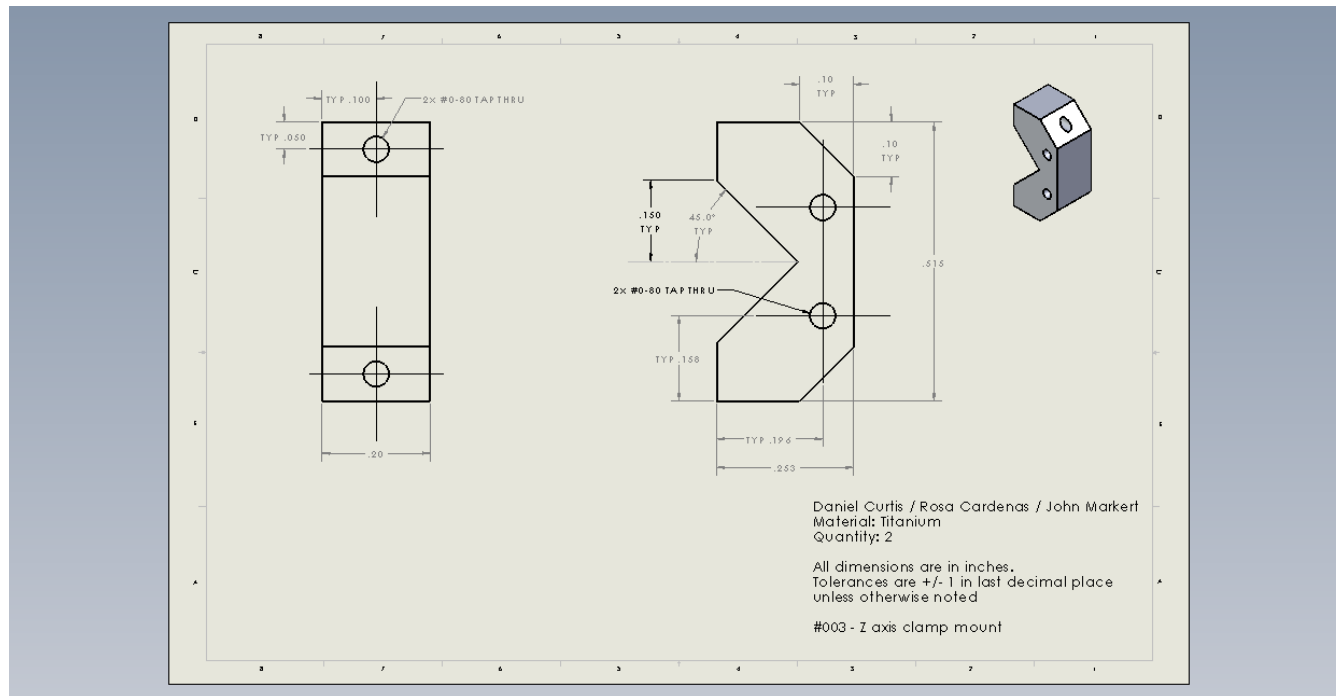


Figure D.8: Base of the x and y clamp.

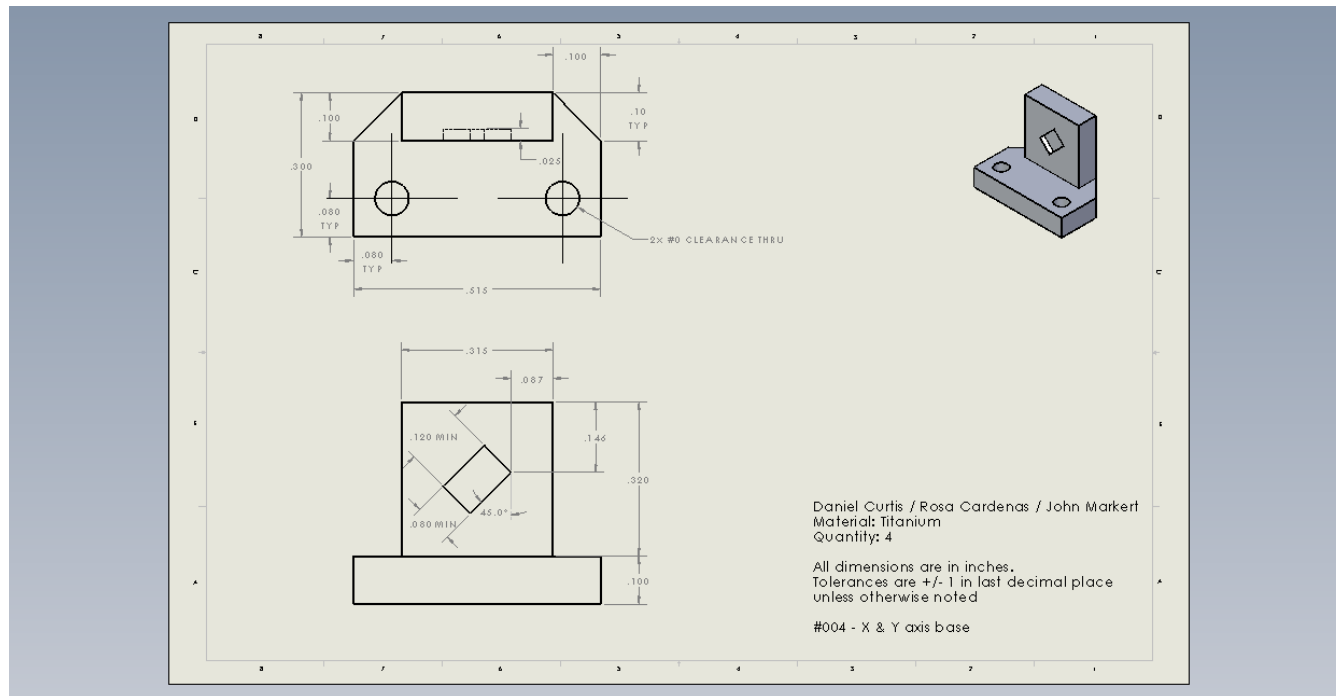


Figure D.9: X and Y clamp drawing.

110

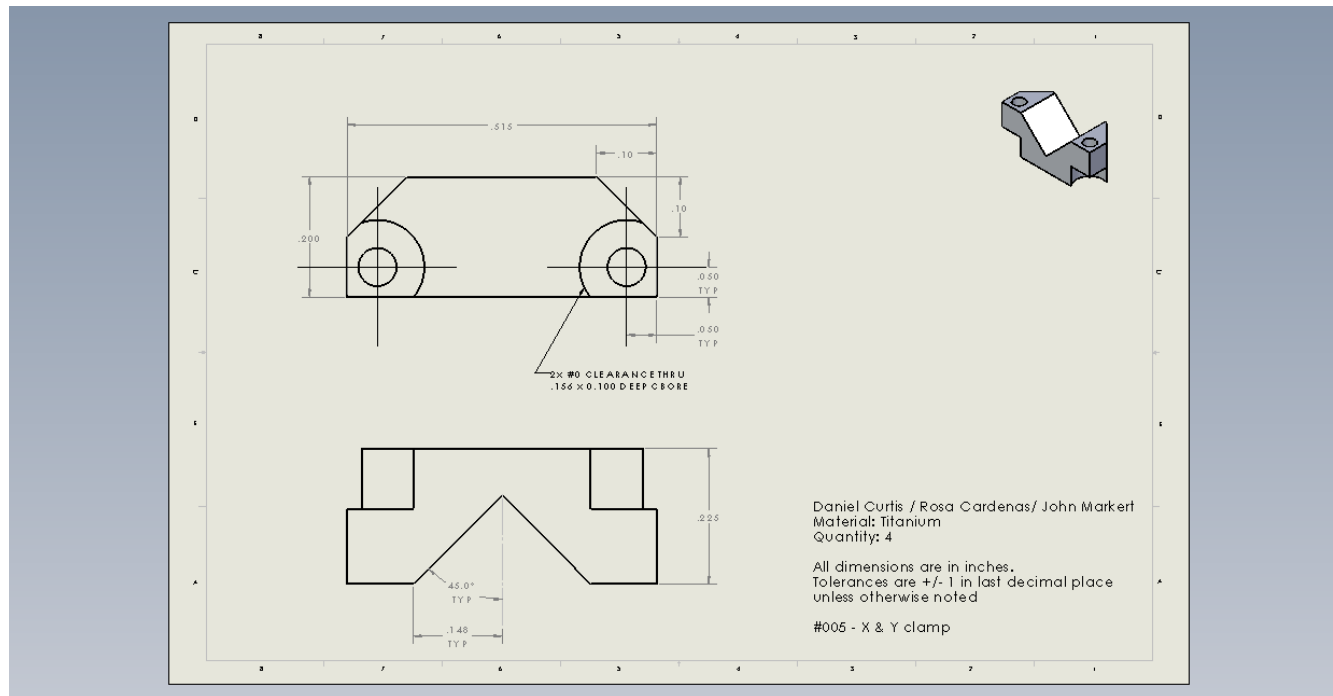


Figure D.10: X and Y clamp and mount drawing.

111

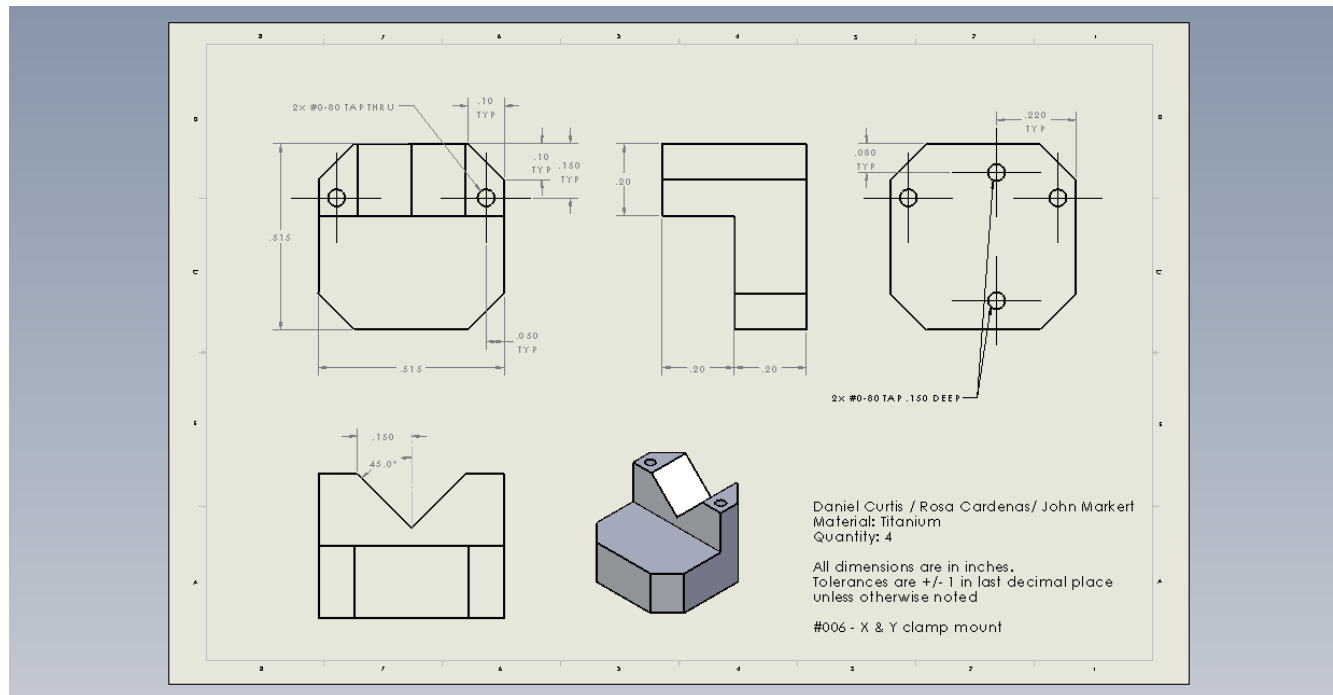


Figure D.11: Fiber mount drawing.

112

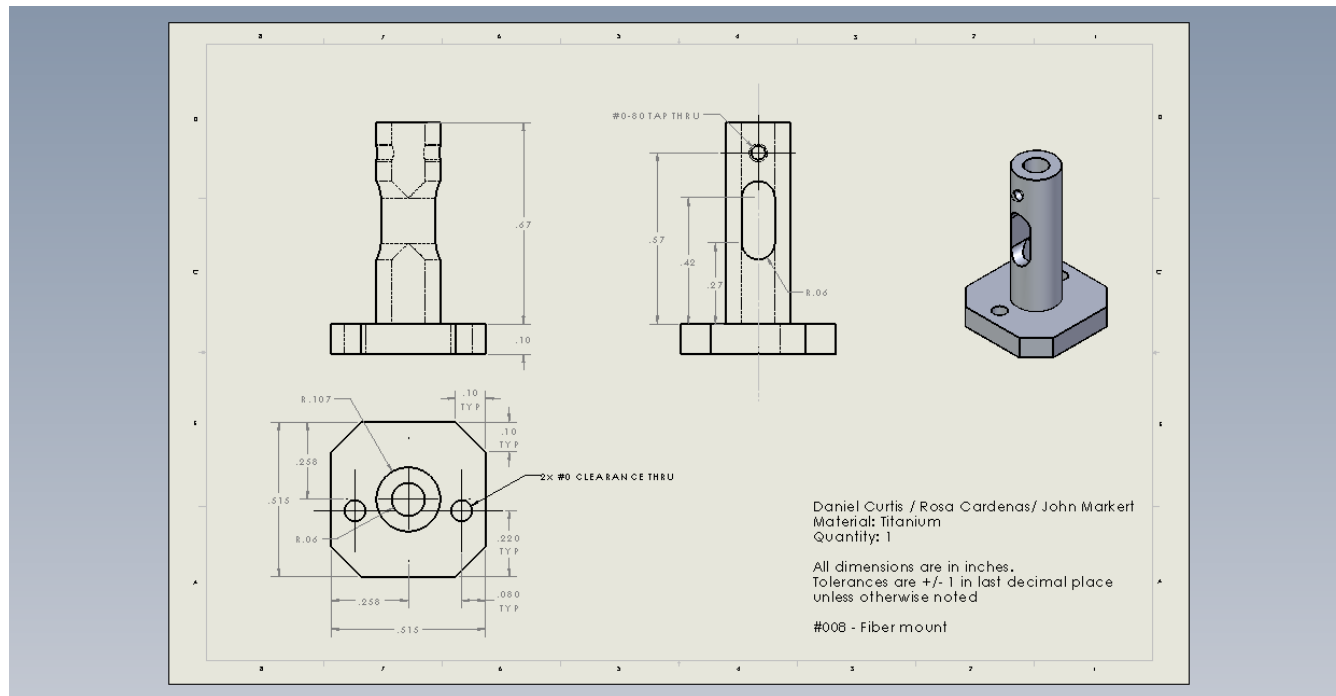


Figure D.12: Magnet mount drawing.

113

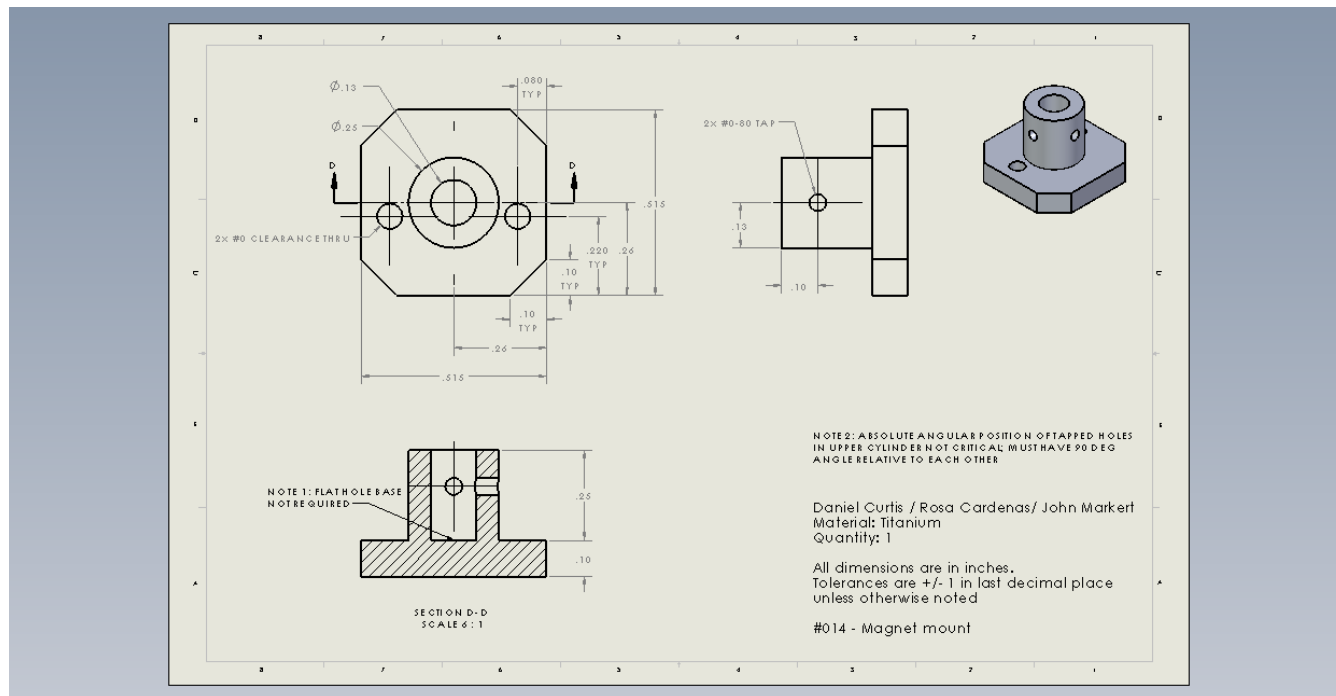


Figure D.13: Cantilever plate drawing.

114

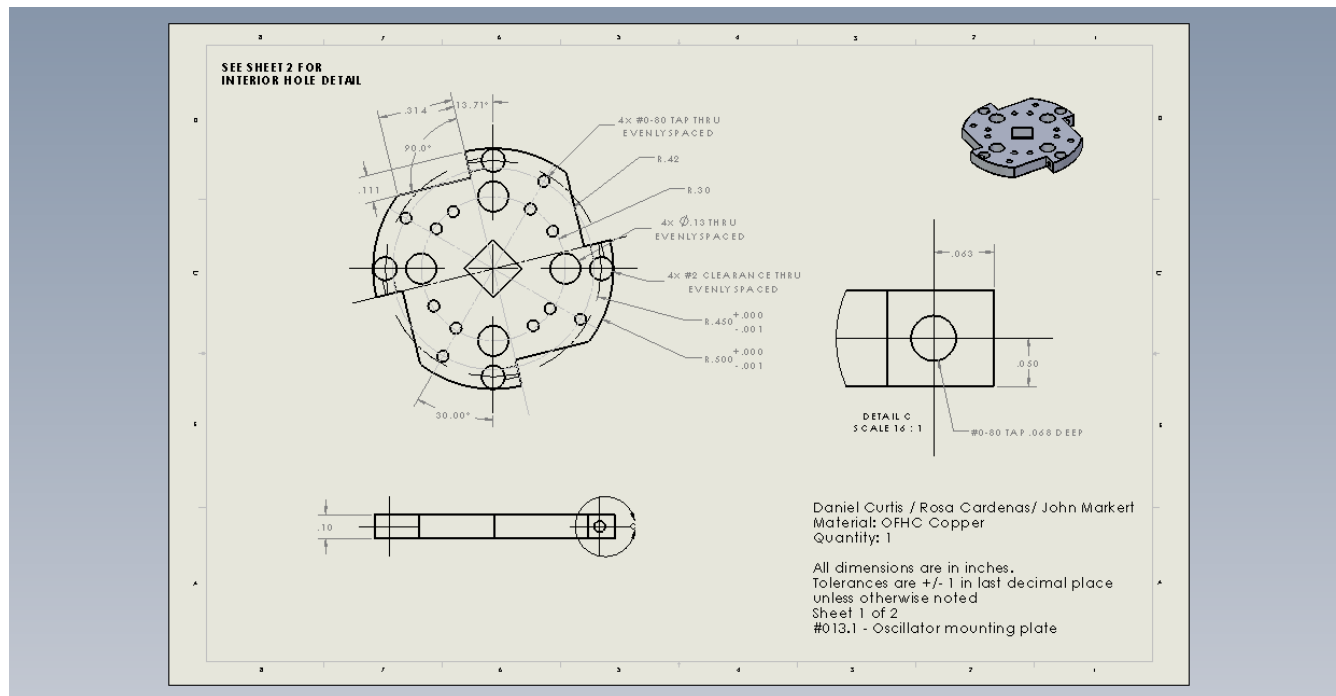
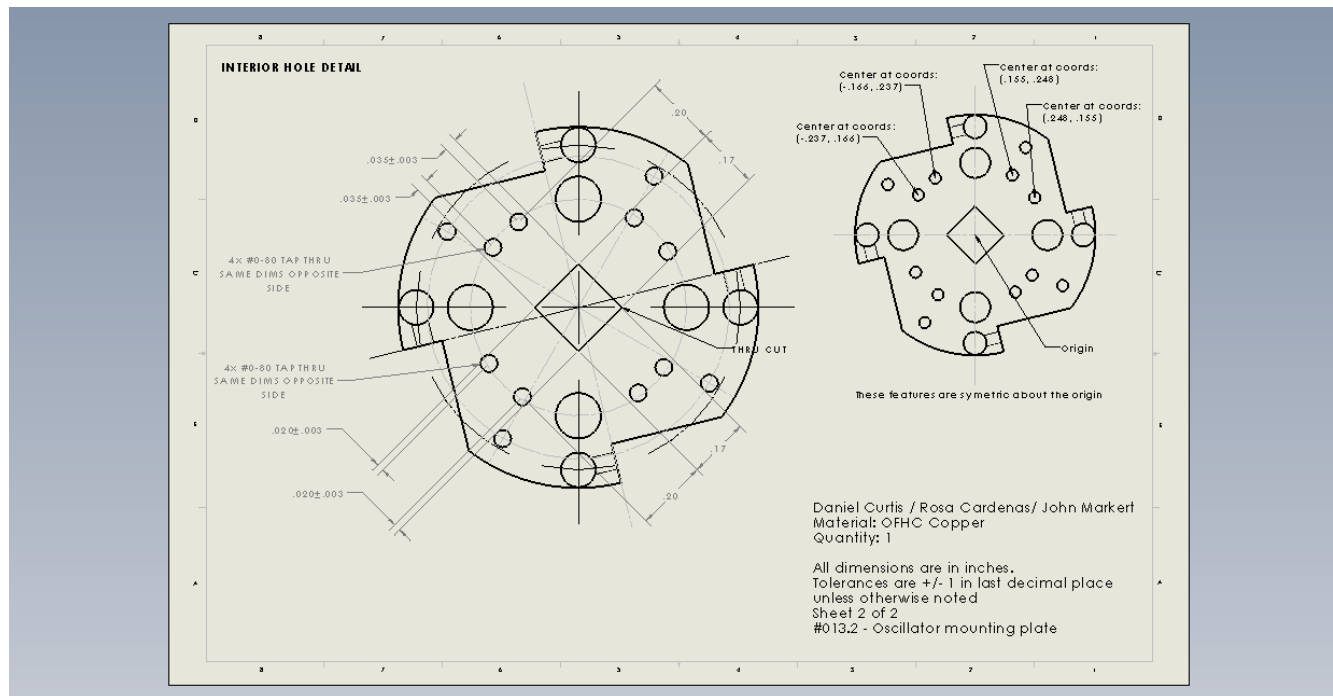


Figure D.14: Cantilever plate drawing hole details.

115



Appendix E

Piezo Specifications

E.1 Plate Piezo Specifications

The plate piezo was ordered from EBL Products Inc. Their website is: <http://www.eblproducts.com/leadzirc.html> and their telephone number is 860-290-3737. The part number is EBL #2. It is a flat disc with a 1×2.25 MHz resonance and a 0.035" thickness. The material type is silver.

E.2 Stack Piezo Specifications

The piezos were ordered online at <http://www.bravoelectro.com/>.

Resin coated type multilayer piezoelectric actuators

AE Series



Features

- Large generated force: 3,500 N/mm² (typ.)
- High speed response: Driving up to about 1/3 of self-resonance frequency (in general ten kHz) is possible.
- Accurate positioning: Controllable in nm order.
- Low power consumption: Can be operated at the leakage current state (100 μA or less)
- Very small size: 1/10 or smaller than conventional multilayer actuators (specific volume)

Outline

Multilayer piezoelectric actuators are ceramic elements for converting electrical energy into mechanical energy such as displacement or force by utilizing the piezoelectric longitudinal effect.
NEC TOKIN's multilayer piezoelectric actuators are produced based on our unique element structure design and using originally developed piezoelectric ceramic materials with high electrostrictive factors. Compared to conventional piezoelectric actuators, they are smaller in size but can generate higher displacement and force at low voltages. Especially, the resin-coated AE series actuators feature compact size and wide variety in shape for applications such as ultra-fine positioning mechanisms and drive sources.

Applications

Auto focusing of cell phone camera, Image stabilization of DSC, Positioning, Mirrors, Pumps, Valves, Vibration source, Vibration control, Sensors, Mirror / Prism positioning, Manipulators, AFM, PFM, etc

Standard Parts List

Model	Displacement [μm] Maximum driving voltage [150VDC]	Overall length [mm]	Generated force [N]	Stiffness [N/mm]	Resonance frequency [kHz]	Capacitance [μF]	Insulation resistance [MΩ]
AE020D04F	4.8 ± 1.5	5	200	43.5	261	0.09	100
AE020D04DF							
AE020D08F	9.1 ± 1.5	10	200	22.0	138	0.18	100
AE020D08DF							
AE020D16F	17.4 ± 2.0	20	200	11.5	69	0.36	50
AE020D16DF							
AE020D44H0F	42.0 ± 6.6	40	200	4.8	34	0.82	20
AE020D44H0DF							
AE050D08F	9.1 ± 1.5	10	850	93.4	138	0.75	50
AE050D08DF							
AE050D16F	17.4 ± 2.0	20	850	48.9	69	1.4	10
AE050D16DF							
AE050D44H0F	42.0 ± 6.6	40	850	20.2	34	3.4	5
AE050D44H0DF							
AE1010D16F	18.4 ± 3.5	20	3,500	190.2	69	5.4	5
AE1010D16DF							
AE1010D44H0F	42.0 ± 6.6	40	3,500	83.3	34	13.6	2
AE1010D44H0DF							
AE1414D16F	18.4 ± 3.5	20	7,000	380.4	69	10.8	2
AE2525D16F							

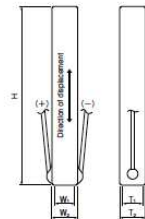
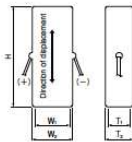
*Thin coating types are available. AE****D**DF has thinner coating thickness.

*For detail information of measurement conditions and outer dimension, please refer to "Performance" and "Outer Dimension" sections.

Outer Dimensions

Overall length 5, 10 and 20mm Products

Overall length 40mm Product



Note:

Factory-shipped polarization : Red lead wire = (+) ,

White lead wire = (-) .

Above drawings do not include dimension of wire connection area and diameter of the wire. Please contact us for details.

Unit : mm

Model	T ₁	W ₁	H	T ₂	W ₂	L
AE020D04F	2 ± 0.1	3 ± 0.1	5 ± 0.1	3.5Max.	4.5Max.	100
AE020D04DF				2.4Max.	3.4Max.	
AE020D08F	2 ± 0.1	3 ± 0.1	10 ± 0.1	3.5Max.	4.5Max.	100
AE020D08DF				2.4Max.	3.4Max.	
AE020D16F	2 ± 0.1	3 ± 0.1	20 ± 0.1	3.5Max.	4.5Max.	100
AE020D16DF				2.4Max.	3.4Max.	

Figure E.1: Stack piezo specifications.

Appendix F

Epoxy Specifications



EPO-TEK® H77 Black
Technical Data Sheet
 For Reference Only
 Thermally Conductive Epoxy

Number of Components:	Two	Minimum Bond Line Cure Schedule*:	
Mix Ratio By Weight:	100:15	150°C	1 Hour
Specific Gravity:			
Part A	2.53		
Part B	1.22		
Pot Life:	6 Hours		
Shelf Life:	One year at room temperature		

*Note: Container(s) should be kept closed when not in use. For filled systems, mix the contents of Part A thoroughly before mixing the two parts together. *Please see Applications Note available on our website.*

Product Description:

EPO-TEK® H77 Black is a two component, thermally conductive, electrically insulating epoxy system designed for lid-sealing of hybrids found in hermetic packaging of micro-electronics. Lids can be ceramic, glass, aluminum or kovar. Package types can be plastic, metal cases or ceramic.

EPO-TEK® H77-BLACK Advantages & Application Notes:

- Very high temperature epoxy. Coatings on metals have been subjected to temperatures as high as 260°C without bond failure. It can also resist >300°C processes found in ceramic or hermetic packaging.
- Rheology provides a soft, smooth, flowing paste with excellent handling characteristics. Its low viscosity nature allows it to be poured or cast into shape for potting applications. It is compatible with automated dispense equipment, screen printing or stamping techniques.
- Excellent solvent and chemical resistance. Excellent for harsh chemical environments found in aircraft, under-hood automotive, medical and petrochemical refineries like down-hole applications.
- It provides near hermetic seals in the packaging of MEMs devices, such as pressure sensors or accelerometers, packaged in TO-cans.
- Suggested for ultra-high vacuum applications.
- It can be also be used for sealing of optical filter windows found in scientific OEM or sensor devices.

Typical Properties: *(To be used as a guide only, not as a specification. Data below is not guaranteed. Different batches, conditions and applications yield differing results; Cure condition: 150 °C/1 hour ; * denotes test on lot acceptance basis)*

Physical Properties:	
*Color: Part A: Black Part B: Amber	Die Shear Strength @ 23°C: ≥ 5 Kg / 1,700 psi
*Consistency: Smooth pourable paste	Degradation Temp. (TGA): 405°C
*Viscosity (@ 20 RPM/23°C): 6,000 – 12,000 cPs	Weight Loss:
Thixotropic Index: 1.72	@ 200°C: 0.15%
*Glass Transition Temp.(Tg): ≥ 75°C (Dynamic Cure	@ 250°C: 0.38%
20–200°C /ISO 25 Min; Ramp -40–200°C @ 20°C/Min)	@ 300°C: 1.47%
Coefficient of Thermal Expansion (CTE):	Operating Temp:
Below Tg: 38 x 10 ⁻⁶ in/in/°C	Continuous: - 55°C to 250°C
Above Tg: 156 x 10 ⁻⁶ in/in/°C	Intermittent: - 55°C to 350°C
Shore D Hardness: 90	Storage Modulus @ 23°C: 904,655 psi
Lap Shear Strength @ 23°C: 1,523 psi	*Particle Size: ≤ 50 Microns
Thermal Properties:	
Thermal Conductivity: 0.66 W/mK	
Electrical Properties:	
Dielectric Constant (1KHz): 5.91	Volume Resistivity @ 23°C: ≥ 2.8 x 10 ¹³ Ohm-cm
Dissipation Factor (1KHz): 0.008	

EPOXY TECHNOLOGY, INC.
 14 Fortune Drive, Billerica, MA 01821-3972 Phone: 978.667.3805 Fax: 978.663.9782
www.EPOTEK.com

Epoxyes and Adhesives for Demanding Applications™

This information is based on data and tests believed to be accurate. Epoxy Technology, Inc. makes no warranties (expressed or implied) as to its accuracy and assumes no liability in connection with any use of this product.

Rev. V
 10/2006

Figure F.1: H77 Black epoxy datasheet.



EPO-TEK® H21D
Technical Data Sheet
 For Reference Only
Electrically Conductive, Silver Epoxy

Number of Components:	Two	Minimum Bond Line Cure Schedule*:	
Mix Ratio By Weight:	10:1	150°C	5 Minutes
Specific Gravity:		120°C	15 Minutes
Part A	2.45	80°C	90 Minutes
Part B	2.14		
Pot Life:	15 Hours		
Shelf Life:	One year at room temperature		

*Note: Container(s) should be kept closed when not in use. For filled systems, mix contents of each container (A & B) thoroughly before mixing the two together. *Please see Applications Note available on our website.*

Product Description:

EPO-TEK® H21D is a two component, high Tg, silver-filled epoxy adhesive designed for chip bonding in microelectronic and optoelectronic applications.

EPO-TEK® H21D Advantages & Application Notes:

- Extended pot-life and can be cured at relatively low temperatures such as 80°C.
- Designed to be used in the 300°C range for applications such as wire bonding operations and eutectic lid-sealing processes.
- *Contains no solvents or thinners. Passes NASA low outgassing standard ASTM E595 with proper cure - <http://outgassing.nasa.gov/>
- Also suggested for hybrid - aerospace circuits found in Rf / Microwave devices like cockpits and satellites.
- Paste-like rheology allows for application by commercial dispensing equipment, stamping, screen printing, or by hand with spatula or toothpick.
- Compatible with Au-plated ceramic substrates found in traditional and custom hybrids.

Typical Properties: *(To be used as a guide only, not as a specification. Data below is not guaranteed. Different batches, conditions and applications yield differing results; Cure condition: 150°C/1 hour; * denotes test on lot acceptance basis)*

Physical Properties:	
*Color: Part A: Silver Part B: Silver	Weight Loss:
*Consistency: Smooth paste	@ 200°C: 0.20%
*Viscosity (@ 20 RPM/23°C): 14,000 – 20,400 cPs	@ 250°C: 0.21%
Thixotropic Index: 2.62	@ 300°C: 0.35%
*Glass Transition Temp.(Tg): ≥ 100°C (Dynamic Cure 20—200°C /ISO 25 Min; Ramp -10—200°C @ 20°C/Min)	Operating Temp:
Coefficient of Thermal Expansion (CTE):	Continuous: - 55°C to 250°C
Below Tg: 26 x 10 ⁻⁶ in/in/°C	Intermittent: - 55°C to 350°C
Above Tg: 124 x 10 ⁻⁶ in/in/°C	Storage Modulus @ 23°C: 712,559 psi
Shore D Hardness: 60	Ions: Cl ⁻ 64 ppm
Lap Shear Strength @ 23°C: 1504 psi	Na ⁺ 72 ppm
Die Shear Strength @ 23°C: ≥ 5 Kg / 1,700 psi	NH ₄ ⁺ 121 ppm
Degradation Temp. (TGA): 457°C	K ⁺
	*Particle Size: ≤ 45 Microns
Electrical Properties:	
*Volume Resistivity @ 23°C: ≤ 0.0009 Ohm-cm	
Thermal Properties:	
Thermal Conductivity: 1.0 W/mK	

EPOXY TECHNOLOGY, INC.
 14 Fortune Drive, Billerica, MA 01821-3972 Phone: 978.667.3805 Fax: 978.663.9782
www.EPOTEK.com

Epoxy and Adhesives for Demanding Applications™

This information is based on data and tests believed to be accurate. Epoxy Technology, Inc. makes no warranties (expressed or implied) as to its accuracy and assumes no liability in connection with any use of this product.

Rev. V
 Apr 2010

Figure F.2: H21D silver epoxy datasheet.

Bibliography

- [1] E. M. Shapiro, S. Skrtic, K. Sharer, J. M. Hill, C. E. Dunbar, and A. P. Koretsky, “MRI detection of single particles for cellular imaging,” *Proceedings of the National Academy of Sciences of the United States of America*, vol. 101, no. 30, pp. 10901–10906, 2004.
- [2] J. A. Sidles, “Noninductive detection of single-proton magnetic resonance,” *Applied Physics Letters*, vol. 58, pp. 2854–2856, 1991.
- [3] D. Rugar, R. Budakian, H. J. Mamin, and B. W. Chui, “Single spin detection by magnetic resonance force microscopy,” *Nature*, vol. 430, pp. 329–332, 2004.
- [4] C. L. Degen, M. Poggio, H. J. Mamin, C. Rettner, and D. Rugar, “Nanoscale magnetic resonance imaging,” *Proceedings of the National Academy of Sciences of the United States of America*, vol. 106, no. 5, pp. 1313–1317, 2008.
- [5] D. J. Griffiths, *Introduction to Electrodynamics*. Prentice Hall, 3rd ed., 1999.
- [6] R. Resnick, D. Halliday, and K. S. Krane, *Physics*. Wiley, 4th ed., 1992.
- [7] C. Kittel, *Introduction to Solid State Physics*. Wiley, 6th ed., 1986.

- [8] D. J. Griffiths, *Introduction to Quantum Mechanics*. Prentice Hall, 1995.
- [9] A. H. Carter, *Classical and Statistical Thermodynamics*. Prentice Hall, 2001.
- [10] C. P. Slichter, *Principles of Magnetic Resonance*. Springer-Verlag, 2nd ed., 1980.
- [11] A. Abragam, *The Principles of Nuclear Magnetism*. Oxford University Press, 1961.
- [12] T. Farrar and E. Becker, *Pulse and Fourier Transform NMR Introduction to Theory and Methods*. Academic Press, 1971.
- [13] M. Puppephat.
- [14] R. A. Pooley, “Fundamental physics of mr imaging,” *RadioGraphics*, vol. 25, no. 4, pp. 1087–1099, 2005.
- [15] J. A. Sidles and D. Rugar, “Signal-to-noise ratios in inductive and mechanical detection of magnetic resonance,” *Physical Review Letters*, vol. 70, no. 22, pp. 3506–3509, 1993.
- [16] N. Nestle, A. Schaff, and W. S. Veeman, “Mechanically detected nmr, an evaluation of the applicability for chemical investigations,” *Progress in Nuclear Magnetic Resonance Spectroscopy*, vol. 38, pp. 1–35, 2000.

- [17] D. Rugar, O. Zuger, S. Hoen, C. S. Yannoni, and R. D. K. H.-M. Vieth, “Force detection of nuclear magnetic resonance,” *Science*, vol. 264, pp. 1560–1563, 1994.
- [18] U. Mirsaidov, *Nuclear Magnetic Resonance Force Microscopy of Ammonium Dihydrogen Phosphate and Magnetism of Cobalt Nanocrystals*. PhD thesis, The University of Texas at Austin, 2005.
- [19] J. D. Jackson, *Classical Electrodynamics*. Wiley, 3rd ed., 1999.
- [20] H. A. Sommer, “Design and construction of a nuclear magnetic resonance force microscope with special attention to micromechanical manipulations and interferometry,” Master’s thesis, The University of Texas at Austin, 1995.
- [21] C. R. Miers, “Design and construction of an nmr force microscope with special attention to vacuum considerations and rf circuitry,” Master’s thesis, The University of Texas at Austin, 1995.
- [22] C. W. Miller, U. M. Mirsaidov, T. C. Messina, and Y. J. Lee, “External effects on the resonant frequency of magnetically capped oscillators for magnetic resonance force microscopy,” *Journal of Applied Physics*, vol. 93, no. 10, pp. 6572–6574, 2003.
- [23] S. Supplies.
- [24] NORCADA.

- [25] Y. J. Lee, *Construction of a Low Temperature Nuclear Magnetic Resonance Force Microscope*. PhD thesis, The University of Texas at Austin, 2006.

Vita

Rosa Elia Cárdenas was born in Houston, TX. She is the youngest of four siblings. After graduating from Business Careers High School in San Antonio, TX, she attended The University of Texas at Austin. After two years at UT, she was awarded the Corporate Sponsored Scholarship from The American Physical Society, and the Gates Millennium Scholars scholarship award from the Bill and Melinda Gates Foundation. In her third year at UT, she began working in Dr. Markert's Magnetism and Superconductivity Lab. In her last year she worked with Soyeun Park in Dr. Josef Kas' Biophysics Lab. After graduating with a Bachelor of Science degree in physics from The University of Texas at Austin, she worked for a company in California. While working, she applied to graduate school and was accepted. She began her graduate work at The University of Texas at Austin, and re-joined Dr. Markert's Magnetism and Superconductivity Lab. Two years later, she graduated from The University of Texas at Austin with a Master of Arts degree in physics. She then continued as a Ph.D. student to pursue the study of solid state crystalline samples using Nuclear Magnetic Resonance Force Microscopy. In one summer, she was awarded an internship at Sematech where she worked for Dr. Joseph Bennett using secondary ion mass spectrometry (SIMS) in the analysis of semiconductor devices. She is graduating with her Ph.D. in physics in August of 2011. After graduation she will begin a postdoctoral position at Sandia

National Lab in Livermore, California where she will build another NMRFM microscope for the analysis of helium in metal.

Permanent address: 1211 W. Mistletoe Ave.
San Antonio, Texas 78201

This dissertation was typeset with L^AT_EX[†] by the author.

[†]L^AT_EX is a document preparation system developed by Leslie Lamport as a special version of Donald Knuth's T_EX Program.